Physical modeling of PEMFC performance and chemical membrane degradation

Von der Fakultät Energie-, Verfahrens- und Biotechnik der Universität Stuttgart zur Erlangung der Würde eines Doktor-Ingenieurs (Dr.-Ing.) genehmigte Abhandlung

Vorgelegt von

Georg Futter

aus Stuttgart

Hauptberichter:	Prof. Dr. K. Andreas Friedrich
Mitberichter:	Prof. Dr. Arnulf Latz
2. Mitberichter:	Prof. Dr. Rainer Helmig

Tag der mündlichen Prüfung: 08.01.2019

Institut für Gebäudeenergetik, Thermotechnik und Energiespeicherung
der Universität Stuttgart
2019

Contents

List of Figures

List of Tables

List of Algorithms

List of Abbreviations

ACL anode catalyst layer. 15

AFOLU agriculture, forestry and other land use. 4

AMG algebraic multigrid. 212

AST accelerated stress test. 186

BP bipolar plate. 7

CCL cathode catalyst layer. 15

CL catalyst layer. 5

CPU central processing unit. 110

DMFC direct methanol fuel cell. 84

DRT distributed relaxation time. 211

ECSA electrochemically active surface area. 28

EIS electrochemical impedance spectra. 99

ePTFE expanded polytetrafluoroethylene. 157

EW equivalent weight. 37

FE finite-element. 88

FER fluoride emission rate. 153

FV finite-volume. 88

GC gas channel. 7

GDL gas diffusion layer. 7

GHG greenhouse gas. 1

HOR hydrogen oxidation reaction. 8

KKT *Karush-Kuhn-Tucker*. 49

MEA membrane electrode assembly. 157

MPL micro-porous layer. 7

NCP nonlinear complementarity problem. 49

OCV open circuit voltage. 12

ORR oxygen reduction reaction. 8

PEM polymer electrolyte membrane. 5

PEMFC polymer electrolyte membrane fuel cell. 4

PFSA poly-fluorinated sulfonic acid. 23

PTFE polytetrafluoroethylene. 38

RDS rate-determining step. 31

REV representative elementary volume. 43

SEM scanning electron microscopy. 157

SOFC solid oxide fuel cell. 143

UNFCCC United Nations Framework Convention on Climate Change. 1

XPS X-ray photoelectron spectroscopy. 155

List of Symbols

Greek symbols

α_l ..... liquid transport coefficient / mol^2 J^{-1} m^{-1} s^{-1}
α_v ..... vapor transport coefficient / mol^2 J^{-1} m^{-1} s^{-1}
χ ..... selectivity of H_2O_2 formation
δ_{ion} ..... thickness of the ionomer film / m
ϵ ..... effectiveness factor for the platinum loading
η^i ..... overpotential of reaction i / V
λ ..... heat conductivity / W m^{-1} K^{-1}
$\lambda^{flux,\kappa}$ ..... lambda-control parameter for component κ
λ^i ..... moles of species i per mol of sulfonic acid
$\mu^{\mathrm{H_2O}}$ ..... chemical potential of H_2O / J mol^{-1}
μ_α ..... dynamic viscosity of phase α / Pa s
Φ ..... potential / V
ϕ ..... porosity
Φ_{elec} ..... electrode potential / V
ϕ_i ..... volume fraction of phase i
Φ_{ion} ..... ionic potential / V
Π^i ..... *Peltier* coefficient of reaction i / V
Ψ ..... flux term / various

ψ^{κ} ..... permeation coefficient of species κ / mol s^{-1} m^{-1} Pa^{-1}

ρ_i ..... mass density of phase i / kg m^{-3}

$\rho_{mol,\alpha}$ ..... molar density of phase α / mol m^{-3}

ρ_{Pt} ..... mass density of platinum / kg m^{-3}

ρ_{PTFE} ..... mass density of PTFE / kg m^{-3}

ρ_s ..... mass density of the solid matrix / kg m^{-3}

σ ..... conductivity / S m^{-1}

$\sigma^{surface}$ .... surface tension / N m^{-1}

θ ..... contact angle / $\circ$

θ^{PtOx} ..... platinum oxide surface coverage

υ^i ..... stoichiometry coefficient of species i

υ ..... frequency / s^{-1}

ξ ..... storage term / various

Roman symbols

a^i ..... activity of species i

A_{cell} ..... cell area / m^2

A_{inlet} ..... gas channel inlet cross section / m^2

$[A]$ ..... molar concentration of species A / mol m^{-3}

$[B]$ ..... molar concentration of species B / mol m^{-3}

c ..... molar charge / C mol^{-1}

C_{DL} ..... double layer capacitance / F m^{-3}

c^i ..... molar concentration of species i / mol m^{-3}

c^i_α ..... molar concentration of species i in phase α / mol m^{-3}

$c_{\mathrm{Pt}}^{\mathrm{O_2}}$ ..... concentration of oxygen at the platinum surface / mol m^{-3}

$c_{p,\mathrm{PTFE}}$ ..... isobaric heat capacity of PTFE / J kg^{-1} K^{-1}

$c_{p,s}$ ..... isobaric heat capacity of the solid matrix / J kg^{-1} K^{-1}

d_i ..... thickness of layer i / m

$\mathbf{d}^\kappa_\alpha$ ..... diffusive flux density of component κ in phase α (mol m^{-2} s^{-1})

D^κ_α ..... diffusion coefficient of species κ in phase α / m^2 s^{-1}

$D^\kappa_{Knudsen,g}$ .. *Knudsen* diffusion coefficient of component κ / m^2 s^{-1}

$D^{\mathrm{O_2}}_{ion}$ ..... diffusion coefficient of O_2 in the ionomer / m^2 s^{-1}

E ..... electrical potential difference / V

$E^{0,i}$ ..... equilibrium voltage of reaction i / V

E^i_{act} ..... activation energy of reaction i / J mol^{-1}

$ECSA$ ..... electrochemically active surface area / m^{-1}
EW ..... equivalent weight / kg mol^{-1}
F ..... *Faraday's* constant / C mol^{-1}
G ..... *Gibbs* free energy / J
g ..... molar *Gibbs* free energy / J mol^{-1}
H ..... enthalpy / J
h ..... molar enthalpy / J mol^{-1}
$h^{\mathrm{H_2O}}$ ..... mass specific enthalpy of water / J kg^{-1}
I ..... cell current / A
i ..... current density / A m^{-2}
I_{min} ..... lambda-control minimum cell current / A
j ..... imaginary number $\sqrt{-1}$
K ..... intrinsic permeability / m^2
k^i ..... rate constant of reaction i / various
$k_{r\alpha}$ ..... relative permeability of phase α
M^κ ..... molar mass of component κ / kg mol^{-1}
M ..... number of phases
m_{Pt} ..... platinum loading / kg m^{-2}
n ..... number of transferred electrons
n ..... normal vector
$n_{drag,l}$ ..... liquid electro-osmotic drag coefficient
$n_{drag,v}$ ..... vapor electro-osmotic drag coefficient
N ..... number of components
p ..... pressure / Pa
p_α ..... pressure of phase α / Pa
p_c ..... capillary pressure / Pa

p^i ..... partial pressure of species i / Pa
Q ..... heat / J
q ..... source- and sink term / various
R ..... lumped ionomer resistance / s m^{-1}
R_{diff} ..... resistance due to diffusion / s m^{-1}
RH ..... relative humidity
$\hat{r}$ ..... integrated volumetric reaction rate / mol m^{-3} s^{-1}
r^i ..... volumetric reaction rate of reaction i / A m^{-3}
R_{int} ..... interfacial resistance / s m^{-1}
R_l ..... resistance due to water films / s m^{-1}
r_{Pt} ..... platinum particle radius / m
R ..... ideal gas constant / J mol^{-1} K^{-1}
S ..... entropy /J K^{-1}
s ..... molar entropy / J mol^{-1} K^{-1}
S_α ..... saturation of phase α
S_{ch} ..... fraction of expanded channels
T ..... temperature / K
t ..... time / s
U ..... internal energy / J
u_α ..... mass specific internal energy of phase α / J kg^{-1}
u^i ..... ion mobility / s mol kg^{-1}
$\mathbf{v}$ ..... velocity / m s^{-1}
V ..... volume / m^3
$\mathbf{v}_\alpha$ ..... velocity of phase α / m s^{-1}
v^i ..... partial molar volume of species i / m^3 mol^{-1}
W ..... work / J

w ..... molar work / J mol^{-1}
x_α^κ ..... mole fraction of component κ in phase α
Z^* ..... complex impedance / Ω m^2
z^i ..... charge number of ion i

Sub- and superscripts

0 ..... standard condition
α ..... phase α
dry ..... in the dry state
eff ..... effective
$elec$ ..... electrical
f ..... forward
$high$ ..... high voltage regime
i ..... various
$init$ ..... initial
ion ..... ionic / ionomer
j ..... various
κ ..... species κ
l ..... liquid equilibrated state
low ..... low voltage regime
pm ..... porous medium
r ..... reverse
rev ..... reversible
sat ..... saturated vapor
sc ..... side chain scission
$trans$ ..... transition
u ..... unzipping
u_{in} ..... indirect unzipping
v ..... vapor equilibrated state
$*$ ..... complex number

Abstract

Polymer electrolyte membrane fuel cells are a clean alternative to the internal combustion engine with the potential to enable the mobility of tomorrow. The cells exhibit a high power density and very good dynamic behavior, which predestines them for the application in automobiles or planes. They are run on hydrogen and ambient air and their main emission is water. In perspective, they can, along with batteries, enable the decarbonization of the mobility sector.

Further dissemination of the technology is hindered by the lack of a hydrogen infrastructure, the high cost of production and degradation mechanisms which reduce the lifetime and performance of fuel cells. Therefore, it is the task of the scientific community, after identification of the relevant processes in the cell, to precipitate a cost reduction and improvement of durability through new materials, optimized cell design and operating conditions.

To identify the processes which govern the cell performance, in this work, a macroscopic polymer electrolyte membrane fuel cell model on the cell level was developed. The model could be validated with experimental measurements in different operating conditions and with different cell types, which proves its significance. With help of the model, through simulation of electrochemical impedance spectra, deep insights into the relevant physical processes, which govern the cell performance can be gained.

Further, a model for the simulation of chemical membrane degradation was developed and coupled to the existing cell performance model. The model was validated under different conditions and allows to predict the chemical membrane degradation depending on the operating parameters.

Kurzfassung

Polymerelektrolytmembranbrennstoffzellen sind eine saubere Alternative zum Verbrennungsmotor mit dem Potential die Mobilität von Morgen zu ermöglichen. Die Zellen weisen eine hohe Leistungsdichte auf und sehr gutes dynamisches Verhalten, was sie zum Einsatz in Automobilen oder Flugzeugen prädestiniert. Sie werden mit Wasserstoff und Umgebungsluft betrieben wobei ihre Hauptemission Wasser ist. Perspektivisch können sie, neben Batterien, die Dekarbonisierung des Mobilitätssektors ermöglichen.

Einer Weiterverbreitung der Technologie stehen bisher die mangelnde Wasserstoffinfrastruktur, die hohen Herstellungskosten und Degradationsmechanismen, welche die Lebenszeit und Leistung der Brennstoffzellen reduzieren, im Weg. Daher ist es die Aufgabe der wissenschaftlichen Gemeinschaft, nach Identifikation der relevanten Prozesse in der Zelle, durch neue Materialien, optimiertes Zelldesign und optimierte Betriebsbedingungen eine Kostenreduktion sowie eine Erhöhung der Lebensdauer herbeizuführen.

Um die relevanten Prozesse, welche die Zellleistung bestimmen, zu identifizieren, wurde in dieser Arbeit ein makroskopisches Modell einer Polymerelektrolytbrennstoffzelle auf Zellebene entwickelt. Das Modell konnte mit experimentellen Messungen in unterschiedlichen Betriebsbedingungen und mit unterschiedlichen Zelltypen validiert werden, was seine Aussagekraft belegt. Mithilfe des Modells können, durch die Simulation elektrochemischer Impedanzspektren, tiefe Einblicke in die rele-

vanten physikalischen Prozesse gewonnen werden, welche die Zellleistung bestimmen.

Darüber hinaus wurde ein Modell zur Simulation der chemischen Membrandegradation entwickelt und mit dem bestehenden Zellleistungsmodell gekoppelt. Das Modell wurde unter verschiedenen Bedingungen validiert und erlaubt es Vorhersagen bezüglich der chemischen Membrandegradation in Abhängigkeit der Betriebsparameter zu treffen.

1 Introduction

Guybrush: I'm on a whole new adventure.
Bart: Growing a moustache?
Guybrush: No. Bigger than that.
Bart: A beard?!?

(Monkey Island 2: LeChuck's Revenge)

On a global scale, the anthropogenic climate change is among the most urging problems humanity is facing today. Since the beginning of the industrial revolution, fossil fuel consumption and greenhouse gas (GHG) emissions are continuously rising. In ten thousand years, our planet has never experienced such a dramatic increase in GHG emissions (see Figure 1.1). As a result, earth's average surface temperature, and the sea levels are rising (see Figure 1.2) along with an increase in floods, heavy rain and droughts [83].

To reduce the hazards due to climate change, the United Nations Framework Convention on Climate Change (UNFCCC) aims to reduce the global warming to 2 °C. In order to achieve this goal, a drastic cut in GHG emissions has to be achieved in all industrial

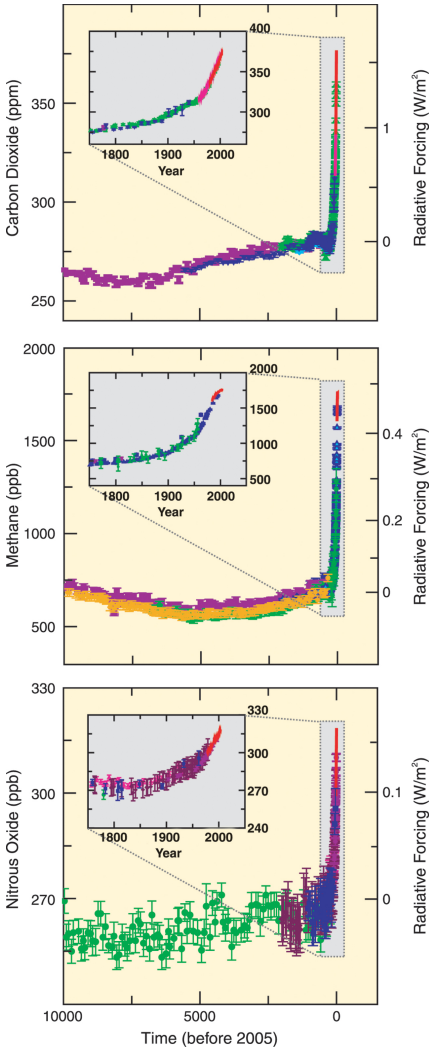

Figure 1.1: Atmospheric concentrations of CO_2, CH_4 and N_2O [82].

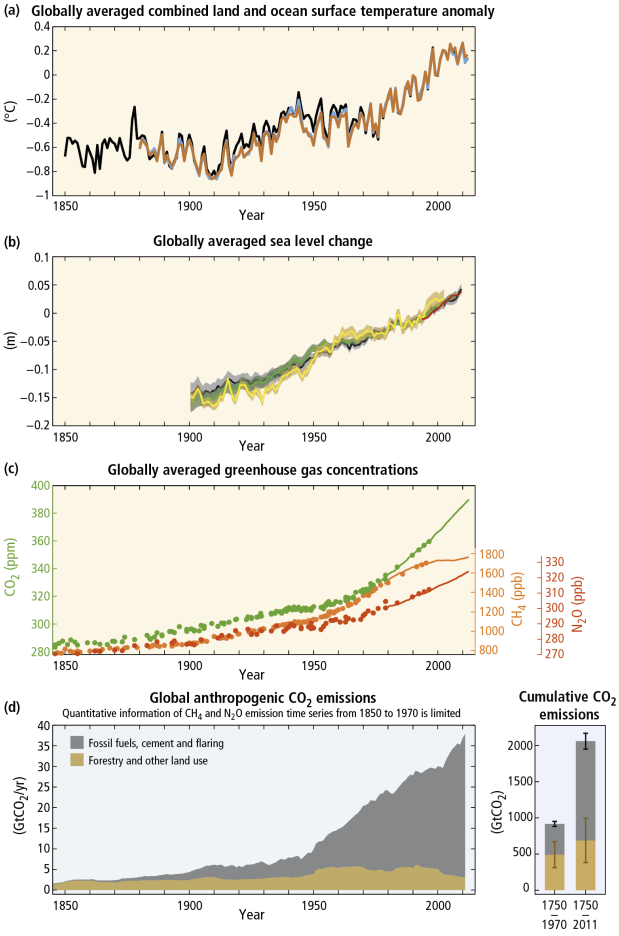

Figure 1.2: Globally averaged temperature anomaly, sea level change, atmospheric GHG concentrations and anthropogenic CO_2 emissions [83].

countries. However, market ready technologies to achieve this goal are missing.

Figure 1.3 shows the world wide GHG emissions sorted by the economic sectors. The third largest contribution to the direct GHG emissions after agriculture, forestry and other land use (AFOLU) and the industry sector is the transport sector. This is due to the prevalence of the internal combustion engine running on fossil fuels. Therefore, in order to achieve the 2 °C-goal, alternatives to this technology need to be developed.

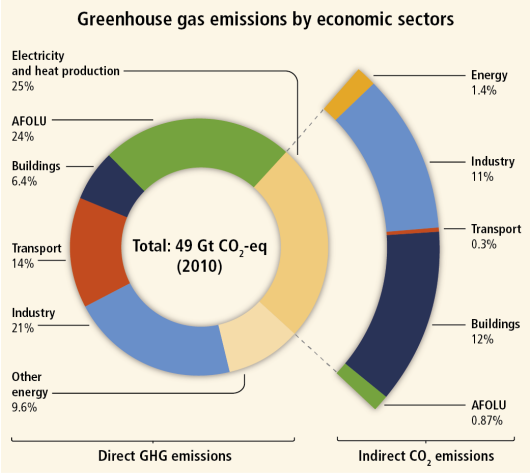

Figure 1.3: GHG emissions by economic sectors [83].

Among the most promising candidates to replace the internal combustion engine and to ensure emission free mobility, are fuel cells. Especially low-temperature polymer electrolyte membrane fuel cells (PEMFCs) with their fast start-up time and high efficiency are an alternative and are already commercially available

today. However, for widespread market penetration, a well developed hydrogen infrastructure is mandatory. Further, the cost of the fuel cell stacks needs reduction, durability needs to be improved and an increase in performance has to be achieved.

Therefore, more fundamental research on the low-temperature PEMFCs is needed. A fuel cell stack for e.g. automobile applications consists of several cells with only a few millimeters thickness. The thickness of the polymer electrolyte membrane (PEM) and the catalyst layers (CLs), the heart of the fuel cell, is in the micrometer range. Consequently, *in situ* and *in operando* measurements are extremely challenging. Luckily, numerical models can help to understand the processes inside a fuel cell and may guide further development in cell components and design.

In a numerical model, the fuel cell is split up into the different layers constituting the cell. For each layer, a specific model is required, describing the dominant processes. These models are then coupled in order to describe the system. From the experimental observations, physical models can be established which can then be translated into mathematical models. Since the relations of processes in the fuel cell are complicated, no analytical solution to the arising mathematical equations is known without strong assumptions. Therefore, the equations need to be discretized which allows the numerical solution.

The aim of this work is to establish a numerical model on the cell level. In Chapter 2 on page 7, the fundamental equations describing the fuel cell from the point of thermodynamics are presented. Chapter 3 on page 17 contains a scientific review on macroscopic

fuel cell models for the PEM and CLs. In Chapter 4 on page 33, several models are then combined to describe the relevant processes of the cell. The model is validated against experimental data obtained in different operating conditions (Chapter 6 on page 109). This is extremely challenging and seldom achieved for macroscopic fuel cell models. The theory presented in this work is very well able to predict the fuel cell performance under various conditions and for different cell types, and is therefore state-of-the-art. On top of the performance model, a model for the chemical membrane degradation is established and validated in different operating conditions (Chapter 7 on page 151). From this model, insights can be gained on the processes which may cause the failure of a fuel cell. Summary and outlook of this work are presented in Chapter 8 on page 209.

2 Thermodynamics and Kinetics of PEMFCs

> In the beginning there was nothing, which exploded.
>
> *(Terry Pratchett, Lords and Ladies)*

In this chapter, a general overview on how a fuel cell works, will be presented. The main components of a cell and the working principle are explained in Section 2.1. In Section 2.2, the equilibrium voltage and its dependencies on temperature, pressure and concentration will be derived. In Section 2.3, the main losses determining the cell voltage under non-equilibrium conditions will be discussed.

2.1 Components and Working Principle

The PEMFC is a device for the conversion of chemical energy into electrical energy. A schematic view of a PEMFC is depicted in Figure 2.1. In a classical cell design, it consists of two electrodes,

anode and cathode, which are composed of four layers each: the bipolar plate (BP) with the gas channels (GCs), gas diffusion layer (GDL), micro-porous layer (MPL) and CL. In the center of the cell, the PEM is located. It is conductive for protons and at the same time isolates the electrodes from electrical short circuits.

On the anode side, hydrogen is fed to the cell which reacts via the hydrogen oxidation reaction (HOR) in the catalyst layer, forming protons and electrons. The protons are transported through the membrane to the cathode side, while the electrons do electrical work in an external circuit. On the cathode side, oxygen as part of the air is pumped through the cell. In the oxygen reduction reaction (ORR), it reacts with the electrons and protons forming water which is then transported out of the cell.

The two half-cell reactions and the overall redox-reaction in the cell are:

$$\mathrm{H_2} \rightleftharpoons 2\,\mathrm{H^+} + 2\,\mathrm{e^-} \tag{2.1}$$

$$\frac{1}{2}\,\mathrm{O_2} + 2\,\mathrm{H^+} + 2\,\mathrm{e^-} \rightleftharpoons \mathrm{H_2O} \tag{2.2}$$

$$\mathrm{H_2} + \frac{1}{2}\,\mathrm{O_2} \rightleftharpoons \mathrm{H_2O}. \tag{2.3}$$

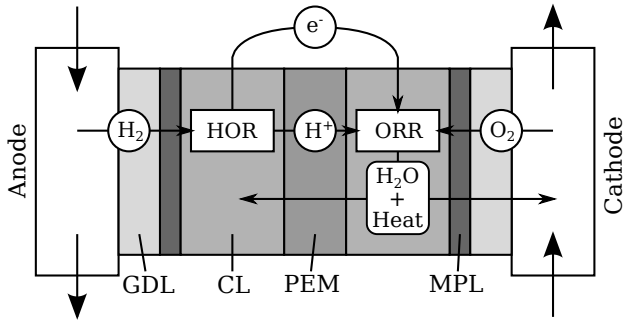

Figure 2.1: Simplified 2D representation of a fuel cell in counterflow mode.

2.2 Equilibrium Voltage

According to the first law of thermodynamics, energy is conserved at all times. Therefore, the internal energy of a system may only change due to transfer of heat and work:

$$\mathrm{d}U = \mathrm{d}Q - \mathrm{d}W. \tag{2.4}$$

The second law of thermodynamics introduces the concept of entropy. It states that the change of entropy in an isolated system will always be equal to or larger zero:

$$\mathrm{d}S \geq 0. \tag{2.5}$$

For a process at constant pressure and temperature, the change of entropy can be expressed as [131]

$$\mathrm{d}S = \frac{\mathrm{d}Q_{rev}}{T} \tag{2.6}$$

where $\mathrm{d}Q_{rev}$ is a reversible transfer of heat. With $W = pV$, Equations (2.4) and (2.6) yield

$$\mathrm{d}U = T\mathrm{d}S - p\mathrm{d}V. \tag{2.7}$$

The *Gibbs* free energy is obtained from a *Legendre transform* of U [131]:

$$G = U - TS + pV = H - TS. \tag{2.8}$$

It represents the work potential of the system. Using molar quantities at standard conditions ($T = 298.15$ K, $p = 101325$ Pa), Equation (2.8) becomes

$$\Delta g^0 = \Delta h^0 - T\Delta s^0 = -w_{elec}. \tag{2.9}$$

which allows to calculate the electrical work done by a fuel cell from the reaction enthalpy and entropy. The electrical work is defined as the work done by a molar charge c moving through an electrical potential difference E:

$$w_{elec} = Ec \tag{2.10}$$

From Equations (2.9) and (2.10) with $c = n\mathrm{F}$, where n is the number of electrons transferred and F is *Faraday's* constant, the relationship between the theoretical equilibrium voltage under standard conditions and the molar *Gibbs* free energy is [131]

$$E^0 = -\frac{\Delta g^0}{n\mathrm{F}}. \tag{2.11}$$

The variation of the equilibrium voltage with temperature, is determined using

$$E = E^0 + \frac{\Delta s}{n\mathrm{F}}\left(T - T^0\right). \tag{2.12}$$

Additionally, the equilibrium voltage changes with pressure and concentration. Introducing the concept of chemical potential, these dependencies can be described using the *Nernst* equation:

$$E = E^0 - \frac{\mathrm{R}T}{n\mathrm{F}}\ln\frac{\Pi_i \left(a^i\right)^{\upsilon^i}}{\Pi_j \left(a^j\right)^{\upsilon^j}}. \tag{2.13}$$

Here, the indices i and j represent the product and educt species respectively. The symbols $a^{i,j}$ and $\upsilon^{i,j}$ denote the species activity

and the stoichiometry coefficient of the corresponding species. Combining equations (2.12) and (2.13) gives

$$E = E^0 + \frac{\Delta s}{n\mathrm{F}}\left(T - T^0\right) - \frac{\mathrm{R}T}{n\mathrm{F}}\ln\frac{\Pi_i \left(a^i\right)^{\upsilon^i}}{\Pi_j \left(a^j\right)^{\upsilon^j}}, \tag{2.14}$$

which is the general expression for the equilibrium voltage under non-standard conditions.

2.3 Voltage Losses

In the last chapter, the cell voltage at thermodynamic equilibrium was derived. At open circuit voltage (OCV), when no current is drawn from the cell, and under load, thermodynamic equilibrium does not hold and the cell voltage is reduced. In Figure 2.2 a schematic polarization curve of a PEMFC is depicted. Additionally, the regions where different types of losses dominate the cell behavior are shown. In the following, these losses will be discussed.

2.3.1 Losses at Open Circuit Voltage

At OCV, the experimentally measured cell voltage is usually in the range of $\sim 0.95 - 1.05$ V [193] which is only $\sim 77 - 85$ % of the theoretical thermodynamic equilibrium voltage. In the literature, several explanations can be found for this type of

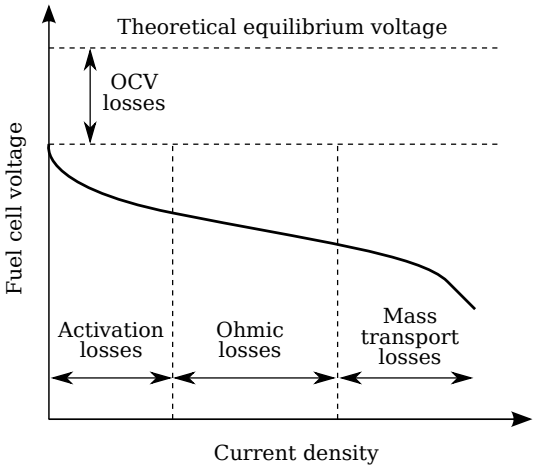

Figure 2.2: Schematic of a polarization curve with the regions dominated by different voltage loss mechanisms.

loss: additional side reactions to the ORR which lead to a mixed potential [23, 53, 69, 79] or the formation of platinum oxides [137].

In [179], these mechanisms are discussed in detail and a third hypothesis is introduced. OCV measurements were carried out with cells containing membranes of varying thickness and it was observed that cells with thicker membranes exhibit a higher OCV. Since gas cross-over is reduced by a thicker membrane, it is argued that the oxidation of cross-over of hydrogen at the cathode leads to a small internal short circuit current which lowers the cell voltage significantly.

2.3.2 Activation Losses

In the electrochemical half-cell reactions of a PEMFC (Equations (2.1) and (2.2)), electrons are produced and consumed causing an electrical current. Each half-cell reaction may proceed in the forward or the reverse direction. Therefore, the net current density of a reaction can be written as $i = i^f - i^r$, where i^f is the current density due to the forward reaction and i^r is the current density due to the reverse reaction. In a dynamic equilibrium, both i^f and i^r are equal to the reactions exchange current density i^0 and therefore, the net current density is zero. Changing the cell potential leads to a shift of equilibrium and either the forward or the reverse reaction will dominate, causing a net electrical current. This means that a part of the cells equilibrium voltage has to be sacrificed in order to produce an electrical current. For a single step electron transfer the relationship between potential and current can be described with the *Butler-Volmer* equation [131]:

$$\begin{aligned} i = i^0 \Bigg[& \Pi_j \left(a^j\right)^{\upsilon^j} \exp\left(\frac{\alpha n \mathrm{F} \eta}{\mathrm{R}T}\right) \\ & -\Pi_i \left(a^i\right)^{\upsilon^i} \exp\left(-\frac{(1-\alpha)\, n \mathrm{F} \eta}{\mathrm{R}T}\right) \Bigg] . \end{aligned} \tag{2.15}$$

In this equation, α is the reactions transfer coefficient, and η represents the so-called activation overvoltage or overpotential. It is the activation loss due to a half-cell reaction. Since i_0 of the ORR is much smaller than the corresponding value for the HOR,

the activation losses in a PEMFC are mostly due to the cathodic half-cell reaction.

2.3.3 Ohmic Losses

In the anode catalyst layer (ACL) charge in the from of ions and electrons is generated. Both types of charges need to be transported to the cathode catalyst layer (CCL) in order to close the circuit. Neglecting all but electrical forces, charge transport may be expressed using *Ohm's* law and the electrical or ionic current is written as

$$i = \sigma \nabla \Phi, \tag{2.16}$$

where σ is the conductivity and $\nabla\Phi$ represents the electrical or ionic potential gradient. From Equation (2.16) it is clear that charge transport will result in so-called ohmic voltage losses equal to $\nabla\Phi$.

2.3.4 Mass Transport Losses

In the *Butler-Volmer* equation (2.15), the species activities at the active sites enter the calculation of the forward and reverse reaction rate. The higher the reactant activities and the lower the product activities, the faster the net reaction rate will be. Therefore, it is desirable to maximize reactant transport to and

product transport from the active site to increase the fuel cell performance especially at higher current densities. Each layer of the fuel cell sandwich represents a transport resistance for reactants and products and will influence the species concentration at the active site in a different way. In this work, the different transport losses will be investigated in detail, along with the losses at OCV, activation- and ohmic losses.

3 Review of Macroscopic PEMFC Models

> Chaos is found in greatest abundance wherever order is being sought. It always defeats order, because it is better organized.
>
> *(Terry Pratchett, Interesting Times)*

A fuel cell can be investigated on many different scales, depending on the processes of interest. These scales can be divided into micro-, meso-, macro-, stack- and system scale. On each scale, the models to describe a process will rely on different assumptions and simplifications. Therefore, their structure, capabilities and results will vary significantly. To review models relevant for PEMFCs on all of these scales is a tremendous task and out of scope of this work. A good overview of PEMFC performance and degradation models can be found in [87] and [186]. Here, the focus will be on macroscopic models for the description of transport in the PEM and CLs.

3.1 Membrane

For the macroscopic description of the polymer electrolyte membrane, two types of models need to be distinguished: sorption and transport models. Sorption models aim to describe the properties of the membrane in equilibrium with an adjacent fluid. Transport models describe how protons and water are transported through the polymer matrix and how they interact. The following review of both types of models is a revised version of the author's contribution to a recent review paper on PEMFC modeling [87].

3.1.1 Sorption Models

The aim of sorption models is to determine the water concentration inside the membrane. This concentration is conveniently expressed as the unit-less quantity $\lambda^{\mathrm{H_2O}}$ which is defined as the number of water molecules per sulfonic acid site in the polymer and depends on the water activity in a vapor phase next to the membrane. Additionally, a complete model needs to explain the water sorption from an adjacent liquid phase as liquid water is formed in the cathode during fuel cell operation. Theoretically, the sorption from a fully saturated vapor phase and a liquid phase should be the same as the activity of water in both phases is equal to unity. However, there is experimental evidence, that the water concentration in the membrane is considerably higher for equilibrium with a liquid phase [178]. This discrepancy is called *Schröder's paradox* [164].

Whether the persistent *Schröder's paradox* really exists, is under discussion since more recent experiments support its absence [90, 135]. It might have been observed even though it may not exist if a non-equilibrium state has been measured for the contact with water vapor at 100% relative humidity. In this case, the equilibration may take hours or even days [96, 116] and stopping the experiment too early results in observation of lower water content. On the other hand, assuming the existence of the paradox, its absence may be observed, if the relative humidity close to 100% is not exactly controlled and liquid water condensates on the membrane surface [96]. As a result, equilibrium with a liquid phase would be measured and the paradox would not appear.

A proposed thermodynamic explanation for *Schröder's paradox* is the existence of a so called *Van der Waals* loop, i.e., a double root solution for the *Gibbs* stability criteria [178]. In this case two distinct equilibrium states satisfying the *Gibbs* stability criteria would exist, resulting in bifurcation of the sorption isotherm curve above a certain activity. However, as pointed out by Freger [59], this would also lead to swelling hysteresis, which was not observed experimentally.

If thermodynamic equilibrium between membrane and adjacent fluid phase can be assumed, an equilibrium sorption model is applicable. In this case, the water content of the membrane is related to water chemical potential outside the membrane. In the following, several equilibrium sorption models will be reviewed, which have been developed to explain *Schröder's paradox*.

The first model presented here was developed by Choi and Datta [33] and further improved by Choi et al. [35]. It is based on *Flory-Huggins* theory for the water/polymer interactions, includes the internal swelling pressure due to water uptake and the formation of the primary hydration sheath on the sulfonic acid groups. *Schröder's paradox* is explained by a *Laplace* pressure forming at the open mouths of the hydrophobic membrane pores when the membrane is in contact with water vapor. Upon contact with liquid water, the pressure is released, lowering the chemical potential of water in the membrane thus leading to further water uptake.

In contrast to the work presented above, Eikerling and Berg [48] argue that the existence of hydrophobic pores in the membrane is not reasonable. On the contrary, they assume perfect wetting of the membrane pores which leads to a reduced vapor pressure over the curved interfaces between pore water and vapor. This causes capillary condensation and it is argued that this process is governing water uptake for high water content while hydration of the sulfonic acid groups governs sorption for low values of $\lambda^{\mathrm{H_2O}}$. In their model, the water content is determined from thermal and chemical equilibrium and mechanic equilibrium between gas or liquid pressure outside the membrane pores and liquid, osmotic and elastic pressure inside the pores. An analytic expression for the wall charge density as function of swelling of a single pore is derived. Again, *Schröder's paradox* is attributed to the lack of capillary pressure for liquid equilibrium, this time raising the internal pressure as the pores are hydrophilic, and described as a first-order phase transition inside the membrane. The model predicts insensitivity of water sorption on the gas

pressure in accordance with experiments but small variations of the relative humidity cause large variations of internal pressure in the range of 10^2 bars. Therefore, it is concluded that hydraulic flux is the prevalent mechanism of water transport in PEM.

In another model, Kreuer uses a *Langmuir* type expression for the chemical potential of water in the hydration shells around the sulfonic acid groups inside the membrane together with a second expression for the chemical potential of the bulk water in the membrane [96]. Both depend on the internal swelling pressure of the polymer which is determined from the storage modulus, being a function of the water content. Assuming equilibrium between these potentials and the chemical potential of an adjacent vapor phase, $\lambda^{\mathrm{H_2O}}$ as a function of relative humidity and temperature is obtained. Up to a relative humidity of 65%, water sorption is found to be exothermal. At higher humidification, sorption proceeds endothermic. From the model, the heats of hydration for water molecules forming the hydration shell around the sulfonic acid groups are obtained and the internal pressure is estimated to be as high as 10 MPa. It is stated that this high internal pressure cannot be caused by the surface tension of the polymer since it is about three orders of magnitude too low. Therefore, the existence of an "extended" surface layer with higher elasticity than the bulk membrane is proposed. The surface layer can maintain a large internal pressure until contact with liquid water causes its rapid restructuring. This leads to a drop of the internal pressure, causing *Schröder's paradox*.

Both, the model of Choi et al. [35] and the model of Eikerling and Berg [48] assume an open pore configuration on the membrane surface. However, such a system would tend to re-

duce the interfacial area between the liquid water and vapor by reorganization of the polymer, resulting in an energetically more favorable state [59]. The model of Kreuer does not rely on this assumption but further experiments are required to establish a physical and mathematical model accounting for the reorganization of the proposed surface layer.

The assumption of thermodynamic equilibrium between membrane and adjacent fluid fails if the gas relative humidity or liquid water content in the cell is changing fast, for example, under automotive conditions. In that case, the operating conditions may change within a few seconds while it could takes minutes or hours for the membrane to equilibrate. Therefore, a description of the water sorption and desorption kinetics is needed. This can be done by describing the flux of water into and out of the membrane using mass transfer coefficients which may depend on temperature, humidity and mechanical properties of the membrane [62, 68, 74, 116, 155, 160, 169, 170]. These mass transfer coefficients are then multiplied with the deviation in water activity from the equilibrium state at the interfaces.

In order to do so, the equilibrium water activity inside the membrane due to the conditions outside the membrane needs to be determined from an equilibrium sorption model.

In the studies mentioned above, it is shown that the processes of sorption and desorption have a strong impact on the water profiles inside the membrane. This indicates the need for physical models of the structure and the relevant transport- and reorganization processes at the membrane surface. For now, mostly

simple empirical functions for the mass transfer coefficients have been used.

3.1.2 Transport Models

The macro-scale transport models for poly-fluorinated sulfonic acid (PFSA) membranes presented in the literature can roughly be divided into three different approaches, being the chemical potential-, diffusion and hydraulic models. They can be distinguished by the driving forces which are considered. The most general driving force for transport is the chemical potential. Depending on its definition, the driving forces for diffusion (gradients of species concentration) and convection (pressure gradients) may be included.

Two early models for the transport of protons and water in the membrane were developed by Springer et al. [174] and Bernardi and Verbrugge [18, 19]. Both are 1D, isothermal, stationary models based on dilute solution theory [128]. Springer et al. [174] employed a diffusion coefficient for water transport, incorporated electro-osmotic drag, and accounted for non-uniform water content in the membrane. The model is suited for conditions where the membrane is equilibrated with water vapor but does not treat the liquid equilibrated case thoroughly. They concluded that water diffusion and electro-osmosis may balance each other to a great extent and that water is flowing from the anode to the cathode.

Bernardi and Verbrugge [18, 19] used the *Nernst-Planck* equation in combination with *Schlögl's* equation [162] to model water

transport in a uniformly, fully hydrated membrane in contact with liquid water. This hydraulic model incorporates pressure differences between anode and cathode. For low current density, the model predicts water transport from cathode to anode, while for high current density it is vice versa.

Another hydraulic model by Eikerling [46] considers electro-osmotic drag for the transport of water in the membrane counterbalanced by *Darcy* flow. In addition to the Bernardi-Verbrugge-model, it considers the local dehydration of the membrane and the membrane permeability as a function of the water content is calculated using the *Hagen-Poiseuille-Kozeny* equation. For the conductivity a percolation-type dependence on the water content is considered. The model predicts a critical current at which the membrane gets dehydrated at the anode side and the conductivity drops dramatically. Optimal membrane hydration is predicted for anode humidification with high water removal rates at the cathode side or for higher cathode pressures and anode water removal. In this work, diffusive and convective transport models are compared to experimental results. It is concluded that diffusive models fail to reproduce the experimental data because membrane dehydration is overestimated.

The model by Fuller and Newman [61] uses *Stefan-Maxwell* equations derived from concentrated solution theory in combination with material balances for each species. It predicts higher membrane conductivity with increasing current, but is not capable to reproduce transport losses at high current density due to its single phase nature. In the simulated concurrent flow channel, there is a high net flux of water from anode to cathode near the inlet and a comparably small flux from cathode to

anode near the end of the channel. This is due to variation of the local current density and the water concentration. In this model, the chemical potential acts as a general driving force for the transport. This concept has been adapted several times, for example in the model of Janssen [88]. Unlike in the diffusion- or hydraulic models, the chemical potential is not separated in this approach. Therefore, no specific transport mechanism is assumed and the formulation is kept general. This results in the flaw that pressure- and activity variations inside the membrane cannot be resolved.

Again, based on [61], Weber and Newman developed a model [187] which represents a combination of the diffusive Springer [174]- and the convective Bernardi/Verbrugge-model [18, 19]. For the vapor equilibrated membrane diffusive single-phase transport through collapsed channels is assumed while for a liquid-equilibrated membrane pressure driven convective flow through expanded channels is considered [187]. Both transport modes may occur in parallel, due to a coexistence of both kinds of channels. The fraction of expanded channels is determined from a measured pore size distribution, a contact angle estimation and use of the *Young-Laplace* equation. With this quantity, it is possible to continuously interpolate between the two transport modes, enabling the model to give a physical description of *Schröder's paradox* [164]. For validation, the model is incorporated into a simple cell model [189].

The model of Fuller and Newman [61] was also adapted by Thampan et al. [176]. To incorporate the interactions between hydronium ions and polymer matrix they used the "dusty-fluid model", which is based on [119]. The interactions between

the stationary polymer-"dust" and the liquid species result in frictional forces and consequently reduced diffusional velocity. In this model, in order to calculate the convective velocity, *Schlögl's* equation [162] was applied. As shown by Fimrite et al. [52] this approach was erroneous as extra viscous forces are introduced and therefore the binary friction model, developed in [124], is the favorable approach.

Consequently Fimrite et al. presented a new model [51] for transport and conductivity based on the binary friction model. Transport is modeled solving generalized *Stefan-Maxwell* equations with membrane hydration and potential as driving forces. In their work, a comparison of the order of magnitude of different driving forces elucidated that pressure gradients across the membrane may be neglected. The corresponding conductivity model is a reduction of the transport model, neglecting concentration gradients of water across the membrane and therefore the influence of water transport on the conductivity. However, the parameters for the transport and conductivity model are the same. This allows direct determination of the transport parameters from conductivity measurements.

Baschuk and Li [13] also used generalized *Stefan-Maxwell* equations with potential and partial density of water in the electrolyte as driving forces combined with non-equilibrium thermodynamics. This approach enabled them to easily couple the transport through the membrane and the electrodes by employing a single domain approach.

Apart from the approaches used above, Choi, Jalani and Datta [35] presented a conductivity model, accounting for transport of

protons via *en masse* diffusion, surface diffusion and *Grotthuss* mechanism. To describe the different transport mechanisms, the *Nernst-Einstein-* and *Einstein-Smoluchowski* equation were employed. The conductivity model is based on their thermodynamic sorption model [33] for Nafion® involving *Flory-Huggins* theory [55]. It forms a theoretical basis for proton conductivity in polymer electrolytes and the authors conclude that a high fraction of pore bulk water is essential for fast proton transport via the *Grotthuss* mechanism.

From the review presented in this section, it becomes clear, that modeling of water sorption and transport, being of utmost importance for the correct description of water management in fuel cells, is a task of high complexity. The kinetic sorption models critically depend on a good equilibrium model and both, transport and sorption are strongly interrelated. A consistent description of these phenomena has, to the authors' knowledge, not been achieved in any model published today.

3.2 Catalyst Layer

In the catalyst layers, two distinct processes need to be modeled: transport of chemical species to the catalyst and the electrochemical reactions. Transport can be divided into transport through the pores and the ionomer phase of the CL. In many models, the volume of the CLs is not resolved and therefore, transport through the pores is neglected. In this work, the importance of the spatial resolution of the CLs will be highlighted.

In Section 3.2.1, the models describing reactant transport through the solid parts of the catalyst layer, consisting of ionomer, carbon support- and catalyst particles, will be presented. Subsequently, the models for the electrochemical reactions at the catalyst surface will be reviewed in Section 3.2.2. Both processes, solid phase transport and reaction, have to be considered in combination for a rigorous description of the catalyst layer.

3.2.1 Agglomerate Models

Agglomerate models aim to describe lower scale transport in a macroscopic way. For these types of models an agglomerate structure of the solid catalyst layer components (see Figure 3.1) is assumed [28, 73, 122, 165, 168, 175].

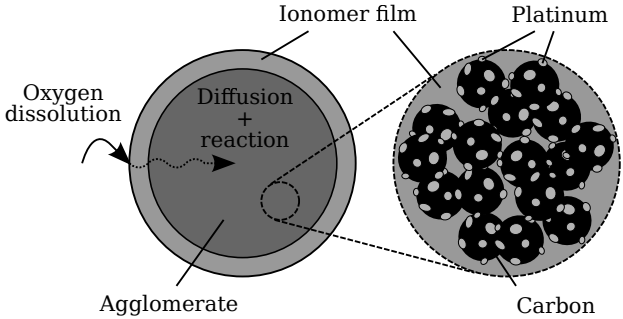

Figure 3.1: Schematic of the agglomerate structure.

It is composed of carbon support particles decorated with platinum particles. These Pt/C-particles are covered by a thin ionomer film and form larger agglomerates. For the ORR, oxygen

needs to be dissolved in the ionomer film covering the agglomerates and to be transported to the platinum particles in order to react. This will cause a concentration gradient inside the agglomerate. With the help of an efficiency factor, describing the agglomerate geometry, *Butler-Volmer* kinetics and the *Thiele* modulus representing the ratio between oxygen diffusion and the reaction kinetics, it is possible to describe oxygen transport and the ORR inside the agglomerates. The agglomerate size used in the models varies in the range of 0.75-3 μm. Additionally, to obtain realistic results, an effective agglomerate area in the range of 10^5 m^{-1} is used. Theoretically, this value should be in the same order of magnitude as the electrochemically active surface area (ECSA) of the catalyst layer, however, in some models, the ECSA values exceed the agglomerate area by ~ 2 orders of magnitude [73, 175]. This points to the fact that additional relevant transport resistances exist which are not included into the models above.

In [98], an analytical solution for the polarization curve of the CCL is derived and it is concluded that for modern catalyst, exhibiting agglomerate radii $\lesssim$ 100 nm, the agglomerate effects manifest themselves only at cell potential lower than 0.1 V and are therefore negligible. The transport resistances considered in this model are oxygen dissolution and diffusion through the ionomer.

More recent studies [97, 109, 136], investigating the oxygen transport resistance in ionomer thin-films, find additional resistances which might be attributed to the ionomer/Pt interface or other effects like anion poisoning. These additional resistances

are incorporated into an ionomer film model of the catalyst layer [70] which will be discussed in the following.

The model is mathematically equivalent to the agglomerate models discussed above, however, it does not depend on the assumption of unreasonably large agglomerates and too low ionomer film areas. The structure considered is a single ionomer-covered Pt/C-particle in accordance with experimental imaging techniques [125, 134, 173, 200]. Oxygen transport resistances due to water films covering the particles, oxygen dissolution into the ionomer, diffusion and an interfacial resistance at the ionomer/Pt interface are incorporated. Embedded into a cell model, the catalyst layer model is able to predict the fuel cell performance under a wide range of experimental conditions and for low platinum loading. Again, it is found that for agglomerates smaller than 150 nm the agglomerate effects are negligible.

3.2.2 Electrochemical Models

The main reactions in the anode and cathode catalyst layer are the hydrogen oxidation reaction and the oxygen reduction reaction respectively (Equations (2.1) and (2.2)).

Since the HOR is facile compared to the ORR, its influence on the fuel cell performance is neglected in several models [8, 73]. Other models which take the anode side into account, usually employ *Butler-Volmer* kinetics to describe the reaction [186]. Again, it should be stated that the *Butler-Volmer* equation (2.15) is strictly only valid for a single step reaction where only one electron is transferred. For low hydrogen concentrations

different formulations have to be applied and also when catalyst contamination is taken into account [87, 180, 182].

Compared to the HOR, the ORR is more complex and more sluggish. Therefore, it has a huge influence on the fuel cell performance and more effort has been made to model the reaction kinetics in detail. Experimental studies of the ORR indicate a doubling of the *Tafel* slope depending on the cathode potential [139]. Therefore, a good ORR model should be able to reproduce this behavior. In the following, two approaches with this capability are discussed.

***Butler-Volmer* or *Tafel* kinetics**

Assuming a single rate-determining step (RDS), simple *Butler-Volmer* or *Tafel* kinetics may be applied. Since several intermediates are involved in the reaction, the proportionality between reaction rate and oxygen concentration at the active site may differ from one. Proportionality factors ranging from 0.5-1, depending on the voltage, have been reported [9, 129, 138]. To model the doubling of the *Tafel* slope, a potential-dependent transfer coefficient and exchange current density have been used [73, 175]. This may be justified if the RDS changes with the potential. Additionally, simple models for the formation of platinum oxides on the catalyst surface are employed [92]. Here, it is assumed that the oxides act as site blockers reducing the active area available for the ORR. Taking into account these mechanisms, the doubling of the *Tafel* slope can be simulated.

Elementary kinetics
To relax the assumption that platinum oxides act as site blockers, the double-trap kinetic based on four elementary kinetic steps has been developed [118, 123, 183, 184]. It is assumed that platinum oxides are solely formed from oxygen and their coverage becomes zero if no oxygen is present. This is a strong simplification as platinum oxides may also be formed from water. Therefore, the platinum oxide coverages calculated with this model are not correct. Each of the four elementary steps becomes rate determining depending on the potential. With this approach, it is possible to describe the doubling of the *Tafel* slope and the platinum oxide coverage. In perspective, it has the capability to describe the platinum dissolution and the regime of high oxide coverage above 1 V [186]. For this approach, at least six parameters (two adsorption and four activation free energies) need to be fitted to cyclic voltammetry or kinetic polarization data. Preferably, they can be estimated from ab-inito modeling.

4 A New Model Formulation

> You will find only what you bring in.
>
> *(Master Yoda)*

In this chapter, a new fuel cell model formulation will be introduced. The basis for the formulation are two distinct models: one describing the membrane and one for the porous electrodes. The physical models and assumptions will presented in this chapter as well as the mathematical formulation. First, in Section 4.1, the basic assumptions will be made and the fundamental transport equations will be derived. In Section 4.2 the sorption model and the transport equations for the polymer electrolyte membrane will be summarized. The equations for the porous domains of the cell (CLs, MPLs, GDLs) and the gas channels are presented in Section 4.3. The mathematical models for the electrochemical half-cell reactions of a PEMFC and for transport in the solid carbon/platinum/ionomer system of the catalyst layers are introduced in Section 4.4. Since most of the source and sink terms of the balance equations presented in this chapter are caused by the electrochemical half-cell reactions, they will also be part of Section 4.4. Only the heat generation due to ohmic heating will be discussed in Sections 4.2 and 4.3 since it is directly related to the charge transport in the corresponding domains. In

Section 4.5, the conditions used to couple the membrane and porous electrode models will be presented.

4.1 Basic Assumptions and Equations

The main assumptions made for this model are:

- Each layer of the fuel cell sandwich can be described as a macro-homogeneous medium with effective transport properties
- The relevant transport processes in the GCs and the porous layers of the cell are the same: convection, diffusion and capillary transport.
- Inertia forces can be neglected.
- Gravitational forces can be neglected.
- Fluid phases in the porous domains are in local chemical equilibrium.
- Local chemical equilibrium between the membrane and the porous electrodes holds.
- Local thermal equilibrium holds.
- Gases behave ideal.

The backbone of a macroscopic PEMFC model is the solution of transient conservation equations. In fluid dynamics, these equations can be derived using the *Reynolds* transport theorem [190] [76]. An arbitrary property of a fluid E (e.g. mass, energy,

momentum) can be obtained by integration of the scalar field e over a control volume Ω moving with velocity $\mathbf{v}$:

$$E = \int_{\Omega} e \, \mathrm{d}\Omega. \tag{4.1}$$

According to the theorem, the temporal derivative of E inside Ω is related to the local changes of e by

$$\frac{\mathrm{d}E}{\mathrm{d}t} = \frac{\mathrm{d}}{\mathrm{d}t} \int_{\Omega} e \, \mathrm{d}\Omega = \int_{\Omega} \frac{\partial e}{\partial t} + \nabla \cdot (e\mathbf{v}) \, \mathrm{d}\Omega. \tag{4.2}$$

Requiring conservation of E, the property can change due to sinks and sources inside Ω which gives

$$\frac{\mathrm{d}E}{\mathrm{d}t} = \int_{\Omega} \frac{\partial e}{\partial t} + \nabla \cdot (e\mathbf{v}) \, \mathrm{d}\Omega = \int_{\Omega} q^e. \tag{4.3}$$

More generally, Equation (4.3) may be written as

$$\frac{\partial \xi^e}{\partial t} + \nabla \cdot \Psi^e - q^e = 0. \tag{4.4}$$

The general structure of this conservation equation is the same for all fuel cell layers and disregarding the conserved quantity (mass, charge and energy). The first term on the left of Equation (4.4) represents the storage term, describing the change of quantity e with time, the second term is the flux term and

q^e denotes the sources and sinks of e. The formulation of these three terms may differ for each fuel cell layer and the conserved quantity considered. For each quantity and layer, the formulation will be presented in the following.

4.2 Membrane

4.2.1 Sorption Model

To describe the water uptake by the polymer membrane as a function of water activity, the sorption isotherm from [121] is used. Assuming chemical equilibrium of the de-protonation reaction of the sulfonic groups ($\mathrm{SO_3H + H_2O \rightleftharpoons SO_3^- + H_3O^+}$) and between membrane water and water in the adjacent gas phase, results in the following system of equations:

$$\begin{aligned} &\frac{\lambda^{\mathrm{H_3O^+}}}{\left(1-\lambda^{\mathrm{H_3O^+}}\right)\left(\lambda^{\mathrm{H_2O}}-\lambda^{\mathrm{H_3O^+}}\right)}\exp\left(\phi_1\lambda^{\mathrm{H_3O^+}}\right) \\ &\times\exp\left(\phi_2\lambda^{\mathrm{H_2O}}\right)=K_1 \end{aligned} \tag{4.5}$$

$$\begin{aligned} \frac{p^{\mathrm{H_2O}}}{p_{sat}^{\mathrm{H_2O}}} =& K_2\left(\lambda^{\mathrm{H_2O}}-\lambda^{\mathrm{H_3O^+}}\right) \\ &\times\exp\left(\phi_2\lambda^{\mathrm{H_3O^+}}\right)\exp\left(\phi_3\lambda^{\mathrm{H_2O}}\right). \end{aligned} \tag{4.6}$$

The parameters ϕ_{1-3} are calculated via

Table 4.1: Parameters of the sorption model.

Parameter	Value	Units	Reference
K_1	100	-	[121]
K_2	$0.217\text{exp}\left[\frac{1000}{\text{R}}\left(\frac{1}{T_{ref}}-\frac{1}{T}\right)\right]$	-	[188]
$E^*_{\text{H}_2\text{O},\text{H}_2\text{O}}$	-4.17×10^{-2}	kg / mol	[121]
$E^*_{\text{H}_3\text{O}^+,\text{H}_2\text{O}}$	-5.2×10^{-2}	kg / mol	[121]
$E^*_{\text{H}_3\text{O}^+,\text{H}^+}$	3.7216	kg / mol	[121]

$$\phi_1 = 2\left(E^*_{\text{H}_2\text{O},\text{H}_2\text{O}} - 2E^*_{\text{H}_3\text{O}^+,\text{H}^+} - 2E^*_{\text{H}_2\text{O},\text{H}_3\text{O}^+}\right)/EW \tag{4.7}$$

$$\phi_2 = 2\left(E^*_{\text{H}_3\text{O}^+,\text{H}_2\text{O}} - E^*_{\text{H}_2\text{O},\text{H}_2\text{O}}\right)/EW \tag{4.8}$$

$$\phi_3 = 2E^*_{\text{H}_2\text{O},\text{H}_2\text{O}}/EW, \tag{4.9}$$

where EW denotes the equivalent weight (EW) of the polymer. The values of the corresponding parameters $E^*_{\text{H}_2\text{O},\text{H}_2\text{O}}$, $E^*_{\text{H}_3\text{O}^+,\text{H}^+}$ and $E^*_{\text{H}_2\text{O},\text{H}_3\text{O}^+}$ along with the values for K_1 and K_2 are listed in Table 4.1.

Since Equations (4.5) and (4.6) need to be solved simultaneously, a two-dimensional lookup table was generated, returning the

values of $\lambda^{\mathrm{H_2O}}$ and $\lambda^{\mathrm{H_3O^+}}$ as a function of water activity and temperature, to speed up the computations.

4.2.2 Membrane Transport

In the ionomer, *concentrated solution theory* [128, 188] is applied to describe the transport of water and protons. If chemical membrane degradation is neglected, the source and sink terms for all species q^{κ} are equal to zero. The storage term of Equation (4.4) for H_2O is

$$\xi^{\mathrm{H_2O}} = c^{\mathrm{H_2O}} = \frac{\phi_{ion}\rho_{PEM,dry}\lambda^{\mathrm{H_2O}}}{EW}, \tag{4.10}$$

where $\lambda^{\mathrm{H_2O}}$ is determined from Equations (4.5) and (4.6) of the sorption model. Here, ϕ_{ion} denotes the volume fraction of ionomer phase in the polymer electrolyte membrane. This value may locally differ from unity due to additives in the membrane, e.g. due to a polytetrafluoroethylene (PTFE) reinforcement layer which is added to improve mechanical stability of the membrane. The dry density of the membrane, $\rho_{PEM,dry}$, and the equivalent weight EW are material parameters.

The flux term is

$$\begin{aligned}\Psi^{\mathrm{H_2O}} =& S_{ch}\left[-\frac{\sigma_{ion} n_{drag,l}}{\mathrm{F}}\nabla\Phi_{ion}\right.\\ &\left.-\left(\alpha_l+\frac{\sigma_{ion} n_{drag,l}^2}{\mathrm{F}^2}\right)\nabla\mu^{\mathrm{H_2O}}\right]\\ &+(1-S_{ch})\left[-\frac{\sigma_{ion} n_{drag,v}}{\mathrm{F}}\nabla\Phi_{ion}\right.\\ &\left.-\left(\alpha_v+\frac{\sigma_{ion} n_{drag,v}^2}{\mathrm{F}^2}\right)\nabla\mu^{\mathrm{H_2O}}\right],\end{aligned} \tag{4.11}$$

where S_{ch} is the fraction of expanded water channels in the membrane [188], n_{drag} denotes the electro-osmotic drag coefficient and α is a transport parameter. The indices v and l stand for the vapor- or liquid equilibrated state of the membrane respectively. In this equation, the primary variables are the ionic potential Φ_{ion} and $\mu^{\mathrm{H_2O}}$, the chemical potential of water. It is defined as

$$\mu^{\mathrm{H_2O}} = \mathrm{R}T\ln\left(a^{\mathrm{H_2O}}\right) + v^{\mathrm{H_2O}}p, \tag{4.12}$$

where $v^{\mathrm{H_2O}}$ is the partial molar volume of H_2O. The expressions for p, $v^{\mathrm{H_2O}}$, $n_{drag,l}$, $n_{drag,v}$, α_l and α_v can be found in [188]. For the ionic conductivity in the membrane $\sigma_{ion,PEM}$, the relation of [174] is used:

$$\begin{aligned}\sigma_{ion,PEM} =& \left(0.5139\lambda^{\mathrm{H_2O}} - 0.326\right)\\ &\times \exp\left[1268\left(\frac{1}{303}-\frac{1}{T}\right)\right] \quad / \quad \mathrm{S\ m^{-1}}.\end{aligned} \tag{4.13}$$

The polymer electrolyte membrane is not perfectly gas tight, but allows small amounts of H_2, O_2, N_2 and other species that may be present in the cell to cross the PEM. Since the concentrations of these species in the ionomer are comparably small, *dilute solution theory* [128] is applied. This means that only the interactions considered are the ones between the cross-over species and the polymer matrix. All other interactions can be neglected [188]. Combining *Henry's* and *Fick's* law allows to describe the transport using permeation coefficients and the species partial pressure as driving force. The conservation equations for the cross-over species read

$$\frac{\partial \phi_{ion} c^{\kappa}}{\partial t} + \nabla \cdot \left[S_{ch} \left(-\psi_l^{\kappa} \nabla p^{\kappa} \right) + \left(1 - S_{ch} \right) \left(-\psi_v^{\kappa} \nabla p^{\kappa} \right) \right] = 0. \quad (4.14)$$

For the vapor- and liquid equilibrated membrane, the permeation coefficients of O_2 are expressed as

$$\begin{aligned} \psi_v^{\mathrm{O_2}} = & \left(1.9 \times 10^{-14} \phi_{\mathrm{H_2O}} + 1.1^{-15} \right) \\ & \times \exp \left[\frac{2.2 \times 10^4}{\mathrm{R}} \left(\frac{1}{303.15} - \frac{1}{T} \right) \right] \\ & / \quad \text{mol m}^{-1}\ \text{s}^{-1}\ \text{Pa}^{-1} \end{aligned} \quad (4.15)$$

and

$$\psi_l^{\mathrm{O_2}} = 1.2 \times 10^{-14} \mathrm{exp}\left[\frac{2 \times 10^4}{\mathrm{R}}\left(\frac{1}{303.15} - \frac{1}{T}\right)\right] \quad / \quad \mathrm{mol\ m^{-1}\ s^{-1}\ Pa^{-1}} \tag{4.16}$$

respectively [188]. The term $\phi_{\mathrm{H_2O}}$ denotes the volume fraction of the water phase in the ionomer, which is a function of the membrane water content $\lambda^{\mathrm{H_2O}}$ and the partial molar volumes of ionomer and water.

For hydrogen the permeation coefficients are

$$\psi_v^{\mathrm{H_2}} = \left(2.2 \times 10^{-14}\phi_{\mathrm{H_2O}} + 2.9^{-15}\right) \times \mathrm{exp}\left[\frac{2.1 \times 10^4}{\mathrm{R}}\left(\frac{1}{303.15} - \frac{1}{T}\right)\right] \quad / \quad \mathrm{mol\ m^{-1}\ s^{-1}\ Pa^{-1}} \tag{4.17}$$

and

$$\psi_l^{\mathrm{H_2}} = 1.8 \times 10^{-14} \mathrm{exp}\left[\frac{1.8 \times 10^4}{\mathrm{R}}\left(\frac{1}{303.15} - \frac{1}{T}\right)\right] \quad / \quad \mathrm{mol\ m^{-1}\ s^{-1}\ Pa^{-1}}. \tag{4.18}$$

For the vapor equilibrated case, the permeation coefficients of O_2 and H_2 increase with higher membrane hydration. The effect of

nitrogen cross-over is not included in the model since the effect on the fuel cell performance is assumed to be negligible as long as it is not operated in dead-end mode.

For proton transport in the membrane, again *concentrated solution theory* [128, 188] is applied. Assuming electro-neutrality, the number of H^+ and SO_3^- in the membrane must be the same. When chemical degradation of the membrane is not considered, the concentration of sulfonic acid groups is constant and therefore, the storage term for the protonic charge balance vanishes.

The flux term is written as

$$\begin{aligned}\Psi^{\mathrm{H}^+} &= S_{ch}\left[-\sigma_{ion}\nabla\Phi_{ion} - \frac{\sigma_{ion}n_{drag,l}}{\mathrm{F}}\nabla\mu^{\mathrm{H_2O}}\right] \\ &+ (1-S_{ch})\left[-\sigma_{ion}\nabla\Phi_{ion} - \frac{\sigma_{ion}n_{drag,v}}{\mathrm{F}}\nabla\mu^{\mathrm{H_2O}}\right].\end{aligned} \tag{4.19}$$

The polymer matrix consists of aqueous and PTFE-like domains. Therefore, the amount of energy stored in the ionomer system will depend on the hydration and can be written as

$$\xi^{energy} = \phi_{\mathrm{H_2O}}\rho_{\mathrm{H_2O}}h^{\mathrm{H_2O}} + (1-\phi_{\mathrm{H_2O}})\,\rho_{\mathrm{PTFE}}c_{p,\mathrm{PTFE}}T, \tag{4.20}$$

where $c_{p,\mathrm{PTFE}} = 960$ J kg^{-1} K^{-1} [1] is used.

For a rigorous description of the system, the internal energy of water $u^{\mathrm{H_2O}} = h^{\mathrm{H_2O}} - p/\rho_{\mathrm{H_2O}}$ should be used. However, a rigorous definition of pressure inside the membrane is lacking and the change of pressure with time is assumed to be small. Therefore, the specific enthalpy $h^{\mathrm{H_2O}}$ is used instead.

Further, assuming heat transport to proceed mainly via heat conduction and convection, the flux term of the energy conservation equation inside the membrane may be written as

$$\Psi^{energy} = -\lambda \nabla T + \Psi^{\mathrm{H_2O}} M^{\mathrm{H_2O}} h^{\mathrm{H_2O}}, \tag{4.21}$$

where λ denotes the heat conductivity. It is expressed as a function of $\lambda^{\mathrm{H_2O}}$ [26]:

$$\lambda_{PEM} = 0.177 + 3.7 \times 10^{-3} \lambda^{\mathrm{H_2O}} \quad / \quad \mathrm{W\ m^{-1}\ K^{-1}}. \tag{4.22}$$

Finally, charge transport in the membrane causes ohmic heating. The heat source due to ohmic heating is calculated via

$$q^{energy} = -\mathbf{i} \nabla \Phi_{ion} \tag{4.23}$$

and the considered current density is calculated according to Equation (4.19).

4.3 Porous Media

4.3.1 Mass Transport

Modeling concepts for porous media
The transport of species through the void space of a porous medium is described based on porous medium theory [76]. All relevant quantities are defined on the basis of the representative elementary volume (REV) [12]. The most important concepts will be briefly discussed:

- *Phases - wetting and non-wetting behavior*: In a multi-phase model, two or more fluid phases may fill the pore space inside the solid matrix. These phases are assumed immiscible and form sharp interfaces. Two different phases can be classified as wetting and non-wetting phase depending on the contact angle θ of the fluid/fluid interface on the solid surface. For a wetting phase, $\theta < 90°$ while for a non-wetting phase, $\theta > 90°$.
- *Components*: Each phase may consist of different components or species. For example, humidified air, which is usually fed to the cathode side of a fuel cell mainly consists of the components nitrogen, oxygen and water. If these species are allowed to dissolve in all phases, the model is called a compositional multi-phase model.
- *Saturation*: The saturation of a phase α is defined as the ratio of the phase volume and total pore volume:
  $S_\alpha = \frac{\text{volume of the phase within the REV}}{\text{volume of the void space within the REV}}$

- *Porosity*: The porosity ϕ is defined as:
  $\phi = \frac{\text{void space within the REV}}{\text{total volume of the REV}}$
- *Intrinsic and relative permeability*: The intrinsic permeability $\mathbf{K}$ is a property of the porous medium, independent of the phases that may flow through it. It is the inverse resistance of the porous medium to flow and is generally a tensorial quantity since porous media may be anisotropic. The concept of relative permeability describes the effect that fluid phases may block pores. This increases the tortuosity of the porous medium for the other phases, reducing their effective permeability.
- *Capillarity*: In small pores, the interfaces between fluid phases are curved due to interfacial tension. Equilibrium at the interface leads to a pressure difference in the phases which is called the capillary pressure p_c. The capillary pressure is defined as follows: $p_c = p_n - p_w$. Here, p_n is the pressure of the non-wetting phase and p_w is the pressure of the wetting phase. For a single capillary, p_c can be calculated using the *Young-Laplace* equation. In a macroscopic view, the capillary pressure can be expressed as a function of the phase saturation.

Governing equations
Based on the assumptions and concepts listed above, the mass balances of the chemical species are derived from the *Reynold's* transport theorem (see Section 4.1). For a system with M different phases and N components, the storage and flux terms of Equation (4.4) for each component κ are [102]

$$\xi^{\kappa} = \phi \sum_{\alpha=1}^{\mathrm{M}} \rho_{mol,\alpha} x_{\alpha}^{\kappa} S_{\alpha} \tag{4.24}$$

$$\Psi^{\kappa} = -\sum_{\alpha=1}^{\mathrm{M}} \left(\rho_{mol,\alpha} x_{\alpha}^{\kappa} \mathbf{v}_{\alpha} + \mathbf{d}_{\alpha}^{\kappa} \right), \tag{4.25}$$

where $\rho_{mol,\alpha}$ is the molar density of phase α, x_{α}^{κ} is the mole fraction of component κ in phase α and S_{α} is the phase saturation. The term $\mathbf{d}_{\alpha}^{\kappa}$ represents the diffusive flux density of component κ in phase α and is described in detail in the paragraph on diffusion below. The phase velocity $\mathbf{v}_{\alpha}$ in Equation (4.25) is calculated based on a multi-phase *Darcy* approach [76, 161]:

$$\mathbf{v}_{\alpha} = -\frac{k_{r\alpha}}{\mu_{\alpha}} \mathbf{K} \nabla p_{\alpha}. \tag{4.26}$$

Constitutive relations

The phase relative permeability for the GDLs is calculated as $k_{r\alpha} = S_{\alpha}^{2.5}$. The exponent in this expression usually ranges from 2-3 [156]. Due to a lack of data, the same expression is used for the MPLs and CLs. In the gas channels, the relative permeability is assumed to be equal to the phase saturation resulting in higher phase mobilities for low saturation.

Transport due to capillary forces is tacitly included in Equation (4.25). The capillary pressure is expressed as a function of the liquid saturation, material wettability, permeability and

porosity using a *Leverett* approach [104]. For a contact angle smaller $90°$,

$$\begin{aligned} p_c =& \sigma^{surface} \cos(\theta) \left(\frac{\mathrm{K}}{\phi}\right)^{-\frac{1}{2}} \\ & \times \left[1.417\,(1-S) - 2.12\,(1-S)^2 + 1.263\,(1-S)^3\right], \end{aligned} \tag{4.27}$$

for a contact angle larger $90°$,

$$\begin{aligned} p_c =& \sigma^{surface} \cos(\theta) \left(\frac{\mathrm{K}}{\phi}\right)^{-\frac{1}{2}} \\ & \times \left[1.417S - 2.12S^2 + 1.263S^3\right] \end{aligned} \tag{4.28}$$

is used, where $\sigma^{surface}$ denotes the surface tension.

Since the pressure of the gas and the liquid phase are related by the capillary pressure, saturation gradients will cause pressure gradients resulting in convective transport.

The intrinsic permeability, porosity and the wetting properties may differ for each of the porous layers (CL, MPL, GDL). In this case, also the capillary pressure saturation relation will be a different one. At the interfaces of two layers, the phase pressures must be continuous in order to fulfill local mechanical equilibrium. Therefore, in case of different capillary pressure saturation relations, the phase saturation must exhibit a discontinuity at the interface.

4.3.2 Diffusion

The molar flux densities of two species i and j in phase α consisting of N components is calculated according to the *Stefan-Maxwell* equation [22]:

$$\nabla x_\alpha^i = \sum_{j=1}^{\mathrm{N}} \frac{c_\alpha^i c_\alpha^j}{c_\alpha^2 D_{eff,\alpha}^i} \left(\frac{\mathbf{d}_\alpha^j}{c_\alpha^j} - \frac{\mathbf{d}_\alpha^i}{c^i \alpha} \right). \tag{4.29}$$

The effective diffusion coefficients $D_{eff,\alpha}^\kappa$ are calculated based on binary diffusion coefficients D_α^κ calculated with the *Fuller*-method [60]. To account for the influence of the porous medium, a *Bruggemann*-correction is applied. The resulting diffusion coefficients in the porous medium are

$$D_{pm,\alpha}^\kappa = (\phi S_\alpha)^{1.5} D_\alpha^\kappa. \tag{4.30}$$

In the liquid phase, $D_{eff,l}^\kappa = D_{pm,l}^\kappa$. In the gas phase, since the pore radii in the CLs and MPLs are in the nanometer range [47], *Knudsen* diffusion has to be considered and the effective diffusion coefficient is calculated with a *Bosanquet* formulation

$$D_{eff,g}^\kappa = \left(\frac{1}{D_{pm,g}^\kappa} + \frac{1}{D_{Knudsen,g}^\kappa} \right)^{-1}, \tag{4.31}$$

where

$$D^{\kappa}_{Knudsen,g} = r_{pore}\frac{2}{3}\sqrt{\frac{8\mathrm{R}T}{\pi M^{\kappa}}}. \tag{4.32}$$

4.3.3 Phase Equilibrium

To simulate the two-phase water management inside a fuel cell, the phase equilibrium between a liquid and a gas phase needs to be incorporated into the numerical model. At elevated humidity or high current density, liquid water will evolve in certain locations and then spread across the modeling domain. At the spreading fronts, oscillations of the phase presence may occur. This effect strongly decreases the simulated time step size, and therefore, the numerical efficiency [102].

To tackle this problem, the approach of [102] is pursued. It will be briefly presented in the following. If a physical quantity exceeds a given threshold a fluid phase will appear or vanish. E.g. if the partial pressure of H_2O exceeds the vapor pressure a liquid phase will appear. Therefore, the conditions for the local phase presence can be formulated as a set of *Karush-Kuhn-Tucker* (KKT) conditions. These KKT-conditions can be reformulated as non-differential but semi-smooth nonlinear complementarity problems (NCPs). In combination with the balance equations presented above (Equation (4.24) and Equation (4.25)), a system of nonlinear equations is obtained which can be solved using a semi-smooth *Newton* method. The NCPs are set up as follows:

1. If a phase is not present, its saturation must be zero. At the same time, the sum over all N mole fractions of the phase is allowed to be smaller than unity:

$$\forall \alpha : S_\alpha = 0 \rightarrow \sum_{\kappa=1}^{\mathrm{N}} x_\alpha^\kappa \leq 1. \tag{4.33}$$

2. By implication, if a phase is present, its saturation must be larger zero and the sum over all N mole fractions yields unity:

$$\forall \alpha : \sum_{\kappa=1}^{\mathrm{N}} x_\alpha^\kappa = 1 \rightarrow S_\alpha > 0. \tag{4.34}$$

3. From Equations (4.33) and (4.34) follows

$$\forall \alpha : S_\alpha \left(1 - \sum_{\kappa=1}^{\mathrm{N}} x_\alpha^\kappa \right) = 0. \tag{4.35}$$

4. Equations (4.33), (4.34) and (4.35) constitute the NCPs. The solution to such a problem is a nonlinear complementarity function f^{NCP}. Here,

$$f^{NCP}(a,b) = \min \left\{ S_\alpha, 1 - \sum_{\kappa=1}^{\mathrm{N}} x_\alpha^\kappa \right\}, \tag{4.36}$$

fulfilling $f^{NCP}(a,b) = 0$ and $a \geq 0 \wedge b \geq 0 \wedge a \cdot b = 0$ is used.

4.3.4 Proton Transport

In the porous electrodes, protons may only be transported in the ionomer containing catalyst layers. Here, the ionomer exists in the form of thin-films covering the carbon and platinum particles. The properties of these thin-films may differ significantly from the those of a bulk membrane [100, 167]. Further research is needed to investigate the properties of these films. Therefore, a simpler approach to describe proton transport compared to the one presented in Section 4.2 is chosen here. Neglecting all but electrical forces, *Ohm's* law is applied to describe proton transport in the catalyst layers. Since protons may be stored in the electrical double layers, the storage term for the charge conservation is

$$\xi^{\mathrm{H}^+} = -C_{DL}\left(\Phi_{elec} - \Phi_{ion}\right). \tag{4.37}$$

The flux term is expressed as

$$\Psi^{\mathrm{H}^+} = -\sigma_{eff}^{\mathrm{H}^+} \nabla \Phi_{ion} \tag{4.38}$$

with the ionic potential acting as the only driving force for proton transport. For the proton conductivity, a material-dependent empirical relation is used which describes the dependence on the water activity. A value $a_{trans}^{\mathrm{H_2O}}$ is defined which separates the water activity range into two domains. For each domain, an exponential relation [141, 167] (f_1 or f_2) with a different

exponent is used and the function is required to be continuous for $a^{\mathrm{H_2O}} = a_{trans}^{\mathrm{H_2O}}$:

$$f_1\left(a^{\mathrm{H_2O}}\right) = A \times \exp\left(B a^{\mathrm{H_2O}}\right) \tag{4.39}$$

$$f_2\left(a^{\mathrm{H_2O}}\right) = A \times \exp\left[\left(B - C\right) a_{trans}^{\mathrm{H_2O}}\right] \exp\left(C a^{\mathrm{H_2O}}\right) \tag{4.40}$$

$$\sigma_{eff,CL}^{\mathrm{H^+}} = \min\left(f_1, f_2\right). \tag{4.41}$$

The resulting function, with the parameters A, B, C and $a_{trans}^{\mathrm{H_2O}}$ given in Table 4.2, is depicted in Figure 4.1.

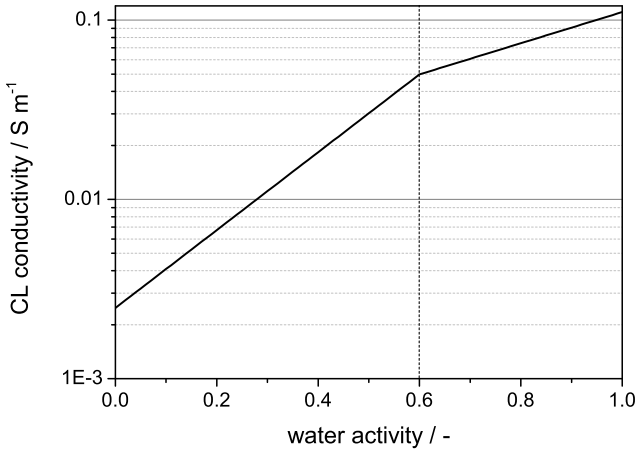

Figure 4.1: Relation for the ionic conductivity in logarithmic scale as a function of the water activity.

Table 4.2: Parameters for the ionic conductivity relation in the CLs.

Parameter	Value and Unit
$a_{trans}^{\mathrm{H_2O}}$	0.6 / -
A	1.5e-2 / S m^{-1}
B	2 / -
C	5 / -

The calculation of source- and sink terms for the protonic charge balance is presented in Section 4.4.3.

4.3.5 Electron Transport

Electrons are transported through all layers of the fuel cell except the polymer electrolyte membrane. In the bipolar plates and the solid matrix of the porous domains, electron transport is described using *Ohm's* law and gradients of the electrode potential are considered as the only driving force. Outside the CLs, the balance equation for electrons is reduced to the flux term:

$$\Psi^{\mathrm{e}^-} = \sigma_{eff}^{\mathrm{e}^-} \nabla \Phi_{elec}. \tag{4.42}$$

Mind that Equation (4.42) has a different sign compared to Equation (4.38). This is due to the fact that, by definition, protons move from high to low potential, while for electrons it is

just the other way round since the charge carried by an electron is negative.

In the catalyst layers, electrons may be stored in the electrical double layers. The storage term describing the charging and discharging of the double layers is the same for protons and electrons and is calculated with Equation (4.37). The calculation of the source- and sink terms is given in Section 4.4.3.

4.3.6 Energy Transport

Assuming thermal equilibrium between the gas, liquid and solid phase allows to write the energy balance of the compositional multi-phase system as one single equation [102]. The energy stored in a volume is composed of the energy of the fluid phases and the energy contained in the solid phase. Therefore, storage term can be written as

$$\xi^{energy} = \phi \sum_{\alpha=1}^{\mathrm{M}} \rho_\alpha u_\alpha S_\alpha + (1-\phi)\, \rho_s c_{p,s} T. \tag{4.43}$$

The energy flux density consists of convective and diffusive contributions in the fluid phases and heat conduction in the solid. It is formulated as

$$\begin{aligned}\Psi^{energy} = &- \sum_{\alpha=1}^{\mathrm{M}} \frac{k_{r\alpha}}{\mu_\alpha} \rho_\alpha h_\alpha \mathbf{K} \nabla p_\alpha \\ &- \sum_{\kappa=1}^{\mathrm{N}} \sum_{\alpha=1}^{\mathrm{M}} h_\alpha^\kappa M^\kappa \mathbf{d}_\alpha^\kappa \\ &- \lambda_{pm} \nabla T.\end{aligned} \tag{4.44}$$

For the heat conductivity of the porous medium, λ_{pm}, depending on the liquid phase saturation S_l, is given by [172]

$$\lambda_{pm} = \lambda_{dry} + \sqrt{S_l} \left(\lambda_{wet} - \lambda_{dry} \right), \tag{4.45}$$

where

$$\lambda_{dry} = \lambda_s^{(1-\phi)} \lambda_g^{\phi} \tag{4.46}$$

and

$$\lambda_{wet} = \lambda_s^{(1-\phi)} \lambda_l^{\phi} \tag{4.47}$$

denote the thermal conductivity of the gas- and liquid-filled porous medium respectively. The thermal conductivity of the gas phase λ_g is is calculated from the pure gas phase species thermal conductivities and the phase composition, for λ_l, the value for liquid water according to [81] is used. The thermal conductivity of the solid phase, λ_s, is assumed to similar to the one of natural graphite, which ranges from 25-470 W m^{-1} K^{-1} [2].

Since the thermal conductivity of the liquid phase is higher than the one of the gas phase, the effective thermal conductivity of the porous media increases with the liquid saturation. With $\lambda_s = 128.95$ W m^{-1} K^{-1}, the effective thermal conductivity, ranges from ~ 0.9 to ~ 5 W m^{-1} K^{-1} for the dry and the fully saturated state which is well within the range of values reported in literature [17, 93].

The source and sink term q^{energy} incorporates energy production and consumption due to the electrochemical reactions and ohmic heating due to proton transport. The contribution from ohmic heating due to electron transport is neglected due to the comparably high electrical conductivity. Ohmic heating due to proton transport is calculated with Equation (4.23). The current density considered in this case, is the one calculated with Equation (4.38).

4.4 Catalyst Layer

In the catalyst layers the electrochemical half-cell reactions proceed. They will be discussed separately for each electrode in Sections 4.4.1 and 4.4.2.

An important parameter for the characterization of the CLs is the ECSA. Assuming spherical platinum particles of a representative radius r_{Pt}, it can be calculated from the platinum loading using [73, 175]

$$ECSA = \frac{\epsilon 3 m_{\mathrm{Pt}}}{r_{\mathrm{Pt}} \rho_{\mathrm{Pt}} d_{CL}}, \tag{4.48}$$

where ϵ is an effectiveness factor for the catalyst utilization.

4.4.1 Anode

The main reaction in the anode catalyst layer of a PEMFC is the hydrogen oxidation reaction (Equation (2.1)). Due to its high exchange current density [130], the contribution of HOR to the cell performance is comparably low. Therefore, a simple model based on the *Butler-Volmer* equation (2.15) was chosen for the calculation of the corresponding reaction rate. To describe the half-cell reaction using *Butler-Volmer* kinetics, it is required to calculate the reaction overpotential. For an arbitrary reaction, it is defined as

$$\eta^i = \Phi_{elec} - \Phi_{ion} - E^{0,i}, \tag{4.49}$$

where $E^{0,i}$ is the equilibrium voltage of reaction i. In case of the HOR, $E^{0,\mathrm{HOR}}$ was chosen as the reference potential and is therefore equal to zero.

The volumetric reaction rate is then calculated as

$$r^{\mathrm{HOR}} = \frac{p^{\mathrm{H_2}}}{p^{\mathrm{H_2}}_{ref}} ECSA_{Anode} i^{0,\mathrm{HOR}} \times \left[\exp\left(\frac{\alpha^f n \mathrm{F} \eta^{\mathrm{HOR}}}{\mathrm{R}T} \right) - \exp\left(-\frac{\alpha^r n \mathrm{F} \eta^{\mathrm{HOR}}}{\mathrm{R}T} \right) \right]. \tag{4.50}$$

4.4.2 Cathode

The slow reaction kinetics of the oxygen reduction reaction influences the performance of a fuel cell to a great extend. Therefore, a more detailed model was developed for the description of the ORR, consisting of three parts:

1. A platinum oxide formation model to calculate the potential dependent coverage of platinum oxides on the electrochemically active surface area.
2. A model for the reaction rate capturing the doubling of the *Tafel* slope.
3. An ionomer film model describing the oxygen transport through the water- and ionomer thin-films covering the Pt/C-particles in the catalyst layer.

These models will be discussed in the upcoming paragraphs.

Platinum Oxide Model
Experimental data exists which indicates that at high cell voltage, platinum oxides are formed on the catalyst surface, slowing down the ORR [111, 139, 184]. Further, there is a strong influence of these oxides on the platinum particle dissolution in the catalyst layers [32, 177] which is out of scope of this work. In this model, regarding the fuel cell performance, platinum oxides are considered as site blockers, reducing the active surface area [92]. The oxides are assumed to be formed according to

$$\mathrm{Pt} + \mathrm{H_2O} \rightleftharpoons \mathrm{PtO} + 2\,\mathrm{H^+} + 2\,\mathrm{e^-}, \tag{4.51}$$

with the estimated equilibrium voltage $E^{0,\mathrm{PtOx}} = 0.81$ V. An additional balance equation is solved in the catalyst layers describing the oxide coverage of the active area:

$$\frac{\partial \theta^{\mathrm{PtOx}}}{\partial t} - q^{\mathrm{PtOx}} = 0. \tag{4.52}$$

For the sake of simplicity, reaction (4.51) is assumed to be the only relevant electrochemical reaction for platinum oxide formation. The source- and sink term of Equation (4.52) is then expressed via [92]

$$
\begin{aligned}
q^{\mathrm{PtOX}} =& k^{\mathrm{PtOX}} \left[a^{\mathrm{H_2O}} \exp\left(\frac{-E_{act}^{\mathrm{PtOX}}}{\mathrm{R}T} \theta^{\mathrm{PtOX}} \right) \right. \\
& \times \left(1 - \theta^{\mathrm{PtOX}}\right) \exp\left(\frac{\alpha^{\mathrm{PtOX}} \mathrm{F} \eta^{\mathrm{PtOX}}}{\mathrm{R}T} \right) \\
& \left. - \theta^{\mathrm{PtOX}} \exp\left(- \frac{\alpha^{\mathrm{PtOX}} \mathrm{F} \eta^{\mathrm{PtOX}}}{\mathrm{R}T} \right) \right],
\end{aligned}
\tag{4.53}
$$

where the rate constant of platinum oxide formation, k^{PtOX}, is assumed to be 0.0128 s^{-1}. In this work, the original formulation was extended to take into account the dependence of the platinum oxide formation on the water activity [198]. This is represented using an *Arrhenius* expression which increases the forward reaction kinetics with higher water activity [43]. The activation energy E_{act}^{PtOX} was estimated to be 10^4 J mol^{-1} in this work. The overpotential η^{PtOX} is calculated with Equation (4.49) and the transfer coefficient α^{PtOX} considered in the *Butler-Volmer* terms is estimated to be 0.5.

The contributions of the platinum oxide model to the proton-, electron and water balance are expressed as

$$
\begin{aligned}
q^{\mathrm{H^+}} = q^{\mathrm{e^-}} =& ECSA_{eff} n 2.1 q^{\mathrm{PtOX}} \\
q^{\mathrm{H_2O}} =& ECSA_{eff} \frac{2.1}{\mathrm{F}} q^{\mathrm{PtOX}},
\end{aligned}
\tag{4.54}
$$

where the factor 2.1 denotes the charge, which is transferred per platinum surface [25], and the effective electrochemical active surface area is calculated with

$$ECSA_{eff} = \left(1 - \theta^{\mathrm{PtOX}}\right) ECSA. \tag{4.55}$$

$ECSA$ is calculated using Equation (4.48).

ORR Reaction Rate

The formulation of the ORR used in this work is given in Equation (2.2) on page 8. Since in this reaction, water is formed in the liquid phase and for the sake of simplicity, its activity is assumed to be equal to unity. Further, the proton- and electron activities are assumed to be unity. The equilibrium voltage of this reaction is then calculated using Equation (2.14) on page 12,

$$\begin{aligned} E^{0,\mathrm{ORR}} =& 1.23 - 9 \times 10^{-4} \left(T - 298.15\right) \\ & - \frac{\mathrm{R}T}{n\mathrm{F}} \ln\left(\frac{1}{\left(a^{\mathrm{O_2}}\right)^{\upsilon^{\mathrm{O_2}}}}\right), \end{aligned} \tag{4.56}$$

where $n = 2$ is the number of transferred electrons and $\upsilon^{\mathrm{O_2}} = 0.5$ is the stoichiometry coefficient of oxygen in Equation (2.2) on page 8.

Experimentally, a doubling of the *Tafel* slope of the ORR has been observed in the range of 0.75 - 0.8 V [139]. This feature is interpreted as a change in the oxygen reduction mechanism. To describe this phenomenon, models based on *Butler-Volmer* kinetics were developed, which use two different sets of parameters for the corresponding voltage regimes [73, 175]. The same approach was applied in this work.

To distinguish between the two voltage regimes, the electrode potential is compared to a defined transition overpotential $\eta_{trans}^{\mathrm{ORR}} = 0.76$ V:

$$\begin{aligned} &\textbf{if } \Phi_{elec} - \Phi_{ion} \geq \eta_{trans}^{\mathrm{ORR}} \Rightarrow \text{high voltage regime} \\ &\textbf{if } \Phi_{elec} - \Phi_{ion} < \eta_{trans}^{\mathrm{ORR}} \Rightarrow \text{low voltage regime.} \end{aligned} \tag{4.57}$$

In each of the voltage regions, different transfer coefficients and exchange current densities are used to determine the ORR reaction rate with a *Butler-Volmer* equation. In the high voltage regime, $\alpha_{high}^{f} = \alpha_{high}^{r} = 0.5$ is assumed and in the low voltage regime, $\alpha_{low}^{f} = \alpha_{low}^{r} = 0.25$ is used. These values are well within the range of reported values [9, 129, 138] when the correct number of transferred electrons is considered in the *Butler-Volmer* equation. The exchange current density in the high voltage regime is calculated with an *Arrhenius* approach (e.g. [73])

$$i_{high}^{0} = i_{ref}^{0} \mathrm{exp}\left[\frac{-E_{act}}{\mathrm{R}}\left(\frac{1}{T} - \frac{1}{323}\right)\right]. \tag{4.58}$$

For the reaction rate to be continuous at the transition of the regimes, the exchange current density of the low voltage regime is calculated as

$$i_{low}^{0} = i_{high}^{0} \mathrm{exp}\left[\left(\alpha_{low}^{f} - \alpha_{high}^{f}\right)\frac{n\mathrm{F}}{\mathrm{R}T}\left(\eta_{trans}^{\mathrm{ORR}} - E^{0,\mathrm{ORR}}\right)\right]. \tag{4.59}$$

In this work, the reaction rate is assumed to be proportional to the square root of the oxygen concentration. This assumption may be justified if the ORR proceeds via more than a single RDS [118, 123, 183, 184]. This assumption is no longer valid close to the limiting current density of the cell. In this case, oxygen transport becomes the RDS and therefore, the reaction rate should be proportional to the oxygen concentration. The reaction rate is formulated as

$$r^{\mathrm{ORR}} = \sqrt{c_{\mathrm{Pt}}^{\mathrm{O_2}}}\, k^{\mathrm{ORR}}, \tag{4.60}$$

where $c_{\mathrm{Pt}}^{\mathrm{O_2}}$, the oxygen concentration at the platinum surface is considered. The rate constant of the ORR is given by

$$k^{\mathrm{ORR}} = \begin{cases} \textbf{high voltage regime}: \\ ECSA_{eff} i_{high}^{0,\mathrm{ORR}} \left(c_{g,ref}^{\mathrm{O_2}}\right)^{-\frac{1}{2}} \\ \times \left[\exp\left(\dfrac{\alpha_{high}^{f} n\mathrm{F}\eta^{\mathrm{ORR}}}{\mathrm{R}T}\right)\right. \\ \left. -\exp\left(\dfrac{-\alpha_{high}^{r} n\mathrm{F}\eta^{\mathrm{ORR}}}{\mathrm{R}T}\right)\right] \\ \\ \textbf{low voltage regime}: \\ ECSA_{eff} i_{low}^{0,\mathrm{ORR}} \left(c_{g,ref}^{\mathrm{O_2}}\right)^{-\frac{1}{2}} \\ \times \left[\exp\left(\dfrac{\alpha_{low}^{f} n\mathrm{F}\eta^{\mathrm{ORR}}}{\mathrm{R}T}\right)\right. \\ \left. -\exp\left(\dfrac{-\alpha_{low}^{r} n\mathrm{F}\eta^{\mathrm{ORR}}}{\mathrm{R}T}\right)\right]. \end{cases} \tag{4.61}$$

Ionomer Film Model

The ionomer film model is based upon the model of [70]. It is mathematically equivalent to the agglomerate model of [92], however, it is physically more reasonable as will be explained in the following.

A sketch of the catalyst layer is depicted in Figure 4.2.

It consists of carbon support particles decorated with the electrochemically active platinum particles. These structures are covered with a thin ionomer film forming a network across the

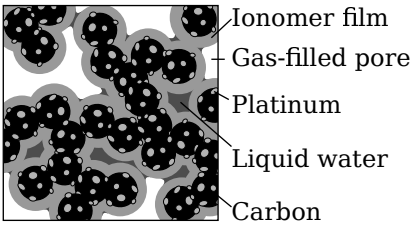

Figure 4.2: Sketch of the catalyst layer structure considered in this model.

catalyst layer. The void space between the ionomer-covered particles may be filled with gas or liquid water.

In order to react, oxygen needs to reach the platinum particle surface. Since water and ionomer films pose a resistance to transport to the active sites, the oxygen concentration at the platinum surface will be lower than in the gas phase. A sketch of the oxygen concentration inside an ionomer thin-film, reproduced after [70], is depicted in Figure 4.3.

The determination of the oxygen concentration at the platinum particles is the purpose of this model. Here, the following resistances are considered:

1. Transport resistance due to water films covering the ionomer
2. Diffusion through the ionomer

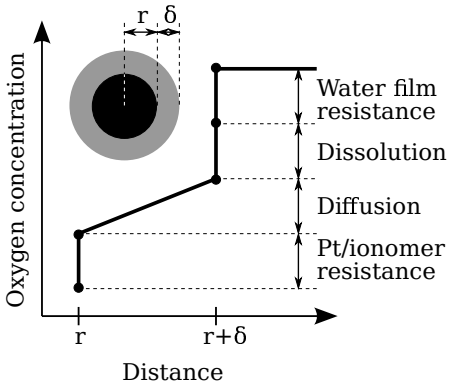

Figure 4.3: Sketch of oxygen concentration inside an ionomer thin-film of thickness δ covering a carbon particle of radius r.

3. A lumped interfacial resistance describing the humidity-dependent dissolution into the ionomer and the interfacial resistance at the platinum / ionomer interface [91].

The flux of oxygen to the platinum surface is

$$\Psi^{\mathrm{O}_2} = \frac{c_g^{\mathrm{O}_2} - c_{\mathrm{Pt}}^{\mathrm{O}_2}}{R}. \tag{4.62}$$

The symbol R denotes the sum of the single resistances, calculated as

$$R = \left(R_l + R_{diff} + R_{int}\right). \tag{4.63}$$

The expressions used in this work for each resistance are

$$R_l = A\sqrt[3]{S_l} \tag{4.64}$$

$$R_{diff} = \frac{\delta_{ion}}{D_{ion}^{\mathrm{O_2}}} \tag{4.65}$$

$$R_{int} = B \exp\left(Ca^{\mathrm{H_2O}}\right), \tag{4.66}$$

where A, B and C are fitted constants. The thickness of the ionomer film, δ_{ion}, is in the range of 7-9 nm which is typical for modern catalyst layers [125].

The effective diffusion coefficient for oxygen in Nafion® is calculated as [175]

$$D_{ion}^{\mathrm{O_2}} = 4.38 \times 10^{-6} \exp\left(\frac{-2.5 \times 10^4}{\mathrm{R}T}\right) \quad / \quad \mathrm{m^2\ s^{-1}}. \tag{4.67}$$

The flux of oxygen calculated with Equation (4.62) is proportional to the volumetric *Butler-Volmer* rate of the ORR (Equation (4.60)) and is expressed as

$$\Psi^{\mathrm{O_2}} = \frac{r^{\mathrm{ORR}}}{n\mathrm{F}ECSA_{eff}} = \frac{\sqrt{c_{\mathrm{Pt}}^{\mathrm{O_2}}}k^{\mathrm{ORR}}}{n\mathrm{F}ECSA_{eff}}. \tag{4.68}$$

In [70], the reaction rate of the ORR was considered to be proportional to the oxygen concentration and an analytical solution is derived for $c_{\mathrm{Pt}}^{\mathrm{O_2}}$. It was stated that numerical methods are required to find an analytical solution if a different proportionality is assumed. However, in this work, the reaction rate is assumed to be proportional to the square root of the oxygen concentration and still an analytical solution can be found for this case as will be shown in the following.

Combination of Equation (4.62) and Equation (4.68) yields

$$n\mathrm{F}ECSA_{eff}c_{\mathrm{Pt}}^{\mathrm{O_2}} + k^{\mathrm{ORR}}R\sqrt{c_{\mathrm{Pt}}^{\mathrm{O_2}}} - n\mathrm{F}ECSA_{eff}c_g^{\mathrm{O_2}} = 0. \quad (4.69)$$

With $\tilde{c}_{\mathrm{Pt}}^{\mathrm{O_2}} = \sqrt{c_{\mathrm{Pt}}^{\mathrm{O_2}}}$ follows

$$n\mathrm{F}ECSA_{eff}\left(\tilde{c}_{\mathrm{Pt}}^{\mathrm{O_2}}\right)^2 + k^{\mathrm{ORR}}R\tilde{c}_{\mathrm{Pt}}^{\mathrm{O_2}} - n\mathrm{F}ECSA_{eff}c_g^{\mathrm{O_2}} = 0. \quad (4.70)$$

The physically reasonable solution to Equation (4.70) is

$$\begin{aligned}\tilde{c}_{\mathrm{Pt}}^{\mathrm{O_2}} &= \sqrt{c_{\mathrm{Pt}}^{\mathrm{O_2}}} \\ &= \frac{-Rk^{\mathrm{ORR}} + \sqrt{4ECSA_{eff}^2 n^2\mathrm{F}^2 c_g^{\mathrm{O_2}} + R^2\left(k^{\mathrm{ORR}}\right)^2}}{2n\mathrm{F}ECSA_{eff}}.\end{aligned} \quad (4.71)$$

Inserting Equation (4.71) into Equation (4.60) gives the final expression for the reaction rate of the ORR:

$$r^{\mathrm{ORR}} = \frac{-Rk^{\mathrm{ORR}} + \sqrt{4ECSA_{eff}^2 n^2 \mathrm{F}^2 c_g^{\mathrm{O_2}} + R^2 \left(k^{\mathrm{ORR}}\right)^2}}{2n\mathrm{F}ECSA_{eff}} k^{\mathrm{ORR}}. \tag{4.72}$$

4.4.3 Sources and Sinks

The electrochemical half-cell reactions in the catalyst layers are, apart from ohmic heating, the sole processes resulting in source and sink terms for the governing equations. The calculation of the source and sink terms for mass, charge and energy will be presented in the following

Mass
The volumetric current densities calculated with Equations (4.50) and (4.72) are directly related to volumetric sources and sinks for the mass balance. The required relation is given by *Faraday's* law. It states that a charge c is required to electrochemically separate n mol of a single-valent ionic species:

$$c = n\mathrm{F} \tag{4.73}$$

Therefore, the volumetric source and sink terms for the mass balance of species κ due to reaction i may be written as

$$q^{\kappa} = \pm \frac{r^i}{n\mathrm{F}}, \tag{4.74}$$

depending on whether the species is consumed or produced in the reaction.

Charge
Due to the formulation as volumetric reaction rates, the Equations (4.50) and (4.72) can be used directly in the source and sink terms of the charge balance equations. Since electroneutrality holds for the half-cell reactions, the source term for the electrical and the ionic charge balance are equal and have the same sign.

Energy
As stated in Section 2.3.2, a certain overpotential is required for each half-cell reaction in order to produce a net current. This energy is dissipated as heat and is related to the volumetric reaction rate of reaction i, the reaction entropy and the overpotential [101]:

$$q^{energy,i} = -|r^i| \left(\Pi^i - |\eta^i| \right). \tag{4.75}$$

where η^i is calculated according to Equation (4.49). The *Peltier* coefficient Π^i is defined as [186]

$$\Pi^i = \frac{T \Delta s^i}{n\mathrm{F}}. \tag{4.76}$$

The reaction entropy Δs^i is determined from the educt and product entropies which have been calculated obtained using NASA Glenn polynomials [120].

4.5 Model Coupling

In this section, the conditions to couple the membrane and porous electrode models will be discussed.

4.5.1 Proton Transport and Secondary Species

The basis for the coupling is the assumption of local thermodynamic equilibrium. Therefore, for protons, the cross-over species hydrogen and oxygen and for the energy balance, the formulation of the coupling conditions is trivial. Electrochemical equilibrium at the interface yields continuity of flux densities and primary variables for the conservation equations. The protonic current density and the ionic potential is assumed to be continuous at the interface. Since the transport of H_2 and O_2 is described using permeation coefficients which combine the diffusivity and solubility (Equations (4.14) to (4.18)), the species partial pressures are continuous over the interface. From local thermal equilibrium follows the continuity of energy fluxes and temperature.

4.5.2 Water Transport

Water transport in the electrodes and the PEM is described by Equations (4.25) and (4.11) respectively. One primary variable of Equation (4.11) is the chemical potential of water calculated according to Equation (4.12). Since a *Dirichlet* type condition is set in the PEM domain, the chemical potential is calculated from the thermodynamic state in the catalyst layer. For the coupling of the liquid phase pressure, a macroscopic averaging approach is used. The pore space of the catalyst layers may be filled with liquid water, depending on the value of the liquid phase saturation S_l. If $S_l = 1$, the membrane is completely in contact with liquid water, for $S_l = 0$, the membrane is in the vapor-equilibrated state and the liquid phase pressure in the membrane is zero according to the physical membrane model of [187]. In between, a linear interpolation is used and the chemical potential inside the PEM is calculated via

$$\mu^{\mathrm{H_2O}} = \mathrm{R}T \ln\left(a^{\mathrm{H_2O}}\right) + S_l v^{\mathrm{H_2O}} p. \tag{4.77}$$

This way, *Schröder's paradox* (see Section 3.1 on page 18) is accounted for in a numerically sound way.

4.6 Initial Conditions

The initial conditions for the anode and cathode sub-domains are listed in Table 4.3. In this table RH denotes the relative

humidity which is an iput parameter to the model. In the PEM domain, the primary variables at the coupling interfaces are calculated according to Section 4.5. These values are then linearly interpolated in the through-plane direction of the cell to obtain the initial conditions inside the domain. The initial conditions at the interfaces are also given in Table 4.3.

Table 4.3: Initial conditions in the electrodes and at the coupling interfaces in the PEM.

Primary variable	Anode	Anode/PEM	PEM/Cathode	Cathode
p_g	$p_{g,out,anode}$	-	-	$p_{g,out,cathode}$
S_l	0	-	-	0
$x_g^{\mathrm{H_2O}}$	$RH_{anode} p_{sat}^{\mathrm{H_2O}} / p_g$	-	-	$RH_{cathode} p_{sat}^{\mathrm{H_2O}} / p_g$
$x_g^{\mathrm{O_2}}$	0	-	-	$0.21 \left(1 - x_{g,cathode}^{\mathrm{H_2O}}\right)$
$x_g^{\mathrm{N_2}}$	-	-	-	$0.79 \left(1 - x_{g,cathode}^{\mathrm{H_2O}}\right)$
$x_g^{\mathrm{H_2}}$	$1 - x_{g,anode}^{\mathrm{H_2O}}$	-	-	0
T	T_{init}	T_{init}	T_{init}	T_{init}
Φ_{ion}	0	0	0	0
Φ_{elec}	0	-	-	$\Phi_{elec,init}$
$\mu^{\mathrm{H_2O}}$	-	$\mathrm{R}T \ln\left(p_{g,anode}^{\mathrm{H_2O}} / p_{sat}^{\mathrm{H_2O}}\right)$	$\mathrm{R}T \ln\left(p_{g,cathode}^{\mathrm{H_2O}} / p_{sat}^{\mathrm{H_2O}}\right)$	-
$p^{\mathrm{H_2}}$	-	$x_g^{\mathrm{H_2}} p_{g,anode}$	$x_g^{\mathrm{H_2}} p_{g,cathode}$	-
$p^{\mathrm{O_2}}$	-	$x_g^{\mathrm{O_2}} p_{g,anode}$	$x_g^{\mathrm{O_2}} p_{g,cathode}$	-

4.7 Boundary Conditions

An overview of the boundary conditions for the different types of balance equations is depicted in Figure 4.4.

4.7.1 Inlet

At the inlets of the anode and cathode sub-domains, the molar fluxes densities of H_2 and O_2 are set as *Neumann* conditions for the corresponding conservation equations. They are calculated from the integrated cell current I using *Faraday's law*, multiplied with a lambda-control proportional constant and projected onto the inlet area. If the cell current is below a given minimum value I_{min}, the molar flux densities are calculated corresponding to this value:

$$\Psi^{\kappa} = \frac{\lambda^{flux,\kappa} \max\left(I_{min}, I\right)}{n \mathrm{F} A_{inlet}} \mathbf{n}. \tag{4.78}$$

At the same time, for all remaining mass balances of the sub-domain, a *Dirichlet* condition is set, specifying the mole fraction. This way, the fluxes as well as the phase composition are controlled at the inlets. For the NCP Equations (4.36), it is not necessary to provide boundary conditions. Further boundary conditions at the inlet are: $T = T_{inlet}$, $\mathbf{i}_{ion} = 0$, $\mathbf{i}_{elec} = 0$ and $S_l = 0$.

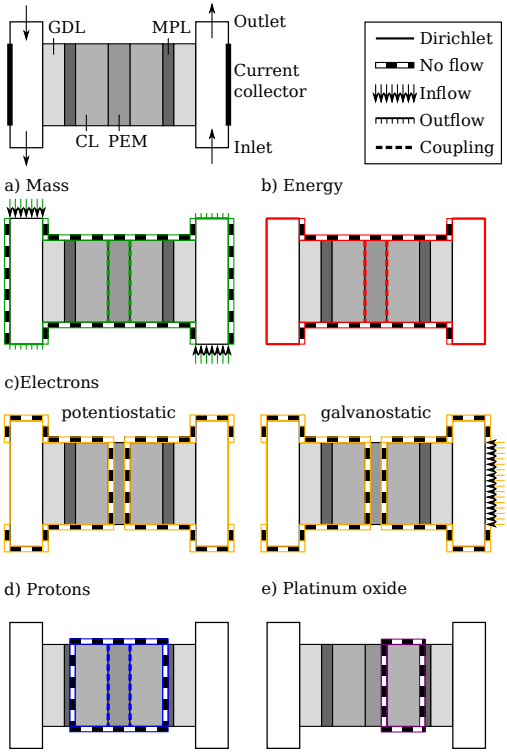

Figure 4.4: Summary of the boundary conditions for the different balance equations. a) Boundary conditions for the mass balances. The details of the inflow and outflow boundary conditions are explained in Sections 4.7.1 and 4.7.2 respectively. b) Boundary conditions for the energy balance. c) Boundary conditions for the electrical charge balance. Left: potentiostatic mode. Right: galvanostatic mode. d) Boundary conditions for the protonic charge balance. e) Boundary conditions for the platinum oxide coverage balance.

4.7.2 Outlet

For all mass conservation equations except one, outflow boundary conditions are set at this boundary. When using an outflow boundary condition, one has to make sure that the gradients of the solution are constant across the boundary. In a compositional system, this means that no diffusion in the through-plane direction may occur, or, that the phases have to be perfectly mixed. To ensure this, additional long tubes are added to the modeling domain at the outlets of the cell. The length of these tubes is chosen such that full mixing is achieved before the phases reach the outlet boundary.

The remaining mass balance equation is replaced by a *Dirichlet* boundary condition for the gas pressure. This is possible because the system is overdetermined, and the single component fluxes are not independent.

Experimentally, the gas pressure is kept constant at the outlets. Therefore, a *Dirichlet* condition for pressure is used setting $p_g = p_{g,outlet}$. The gas phase pressure is a primary variable which corresponds to one of the NCP functions (4.36). Numerically, setting a *Dirichlet* condition for this variable means that the corresponding equation is not solved anymore. In this case the local residual of the equation is replaced by the difference between the value of the primary variable and the value of the boundary condition. This would lead to unphysical behavior. Therefore, one of the mass balance equations is replaced instead as explained above. Again the boundary conditions for the energy and charge balances are: $T = T_{outlet}$, $\mathbf{i}_{ion} = 0$ and $\mathbf{i}_{elec} = 0$.

4.7.3 Current Collectors

The location of the current collectors is depicted in Figure 4.4 c). For all mass balances, no flow boundary conditions are set here. A *Dirichlet* condition for the temperature is applied at anode and cathode side. For the electrical charge balance, the electrode potential is set to the value of the reference potential at the anode: $\Phi_{elec} = 0$. At the cathode side, the boundary conditions depend on the cell operation mode. In potentiostatic mode, a *Dirichlet* condition specifies the value of Φ_{elec} equal to the cell voltage. In case of galvanostatic operation, a *Neumann* condition is used setting the electrical current density, which is calculated from the desired cell current and the cell area according to

$$\mathbf{i}_{elec} = I/A_{cell}\mathbf{n}. \tag{4.79}$$

4.8 Summary

In the following the physical processes represented in the performance model will be summarized along with the most important corresponding equations.

- Water sorption of the polymer electrolyte membrane: Equations (4.5) to (4.6).

- Detailed water- and proton transport in the polymer electrolyte membrane: Equations (4.10) to (4.11) and Equation (4.19).
- Gas cross-over through the membrane: Equation (4.14).
- Energy transport through the membrane and ohmic heating due to charge transport: Equations (4.20) to (4.21) and Equation (4.23).
- Compositional multi-phase flow in porous media due to convection, diffusion, and capillary forces: Equations (4.24) to (4.28)
- Detailed model for *Stefan-Maxwell* and *Knudsen* diffusion in porous media: Equations (4.29) to (4.32)
- Proton and electron transport in the porous electrodes: Equations (4.37) to (4.38) and Equation (4.42).
- Energy transport in the gas-, liquid- and solid phase in the porous electrodes: Equations (4.43) to (4.44).
- Electrochemical model for the hydrogen oxidation reaction: Equation (4.50).
- Detailed electrochemical model for the oxygen reduction reaction taking into account platinum oxide formation, a doubling of the *Tafel* slope and transport resistances due to water- and ionomer films in the catalyst layer: Equations (4.52) to (4.53), Equations (4.56) to (4.61) and Equation (4.72)

- Mass production and consumption due to the half-cell reactions: Equation (4.74)
- Heat production due to the half-cell reactions: Equation (4.75)
- Coupling of mass-, charge- and energy transport in the membrane and electrodes

5 NEOPARD-X

> "Forty-two," said Deep Thought, with infinite majesty and calm.
>
> *(Douglas Adams, The Hitchhiker's Guide to the Galaxy)*

The governing equations presented in Chapter 4 are implemented in the NEOPARD-X framework which was developed in the course of this work. The acronym NEOPARD-X stands for **N**umerical **E**nvironment for the **O**ptimization of **P**erformance **A**nd **R**eduction of **D**egradation of **X**, where **X** denotes an energy conversion device. It is designed as a flexible framework for transient 2D and 3D simulations of e.g. fuel cells and electrolyzers. The details of the framework will be presented in the following. Section 5.1 gives an overview of the NEOPARD-X code, in Section 5.2 the spatial and temporal discretization is presented. Sections 5.3 and 5.4 describe how different experiments can be simulated with the NEOPARD-X code. In Section 5.5 the most important features of the modeling framework, which can be controlled from the input file are discussed.

NEOPARD-X depends on DUNE [16] [15] as well as on Dumu^X [54]. Further, it requires Dune PDE-Lab, UG [14], Multidomain

Table 5.1: Software versions of the dependencies.

Software	Version
DUNE	2.3.1
Dumu^{X}	2.7 or 2.8
Dune PDELab	2.0.0
UG	3.11.0
Multidomain	2.0.0
Multidomaingrid	2.3.0
SuperLU	4.3

and Multidomaingrid [126, 127]. SuperLU [106, 107] is used as linear solver. The corresponding software versions used to obtain the results presented herein are listed in Table 5.1.

5.1 Code Structure

This section, gives an overview of the code structure of the NEOPARD-X framework. First, an overview based on the folder structure will be given in the following. The directory tree is depicted in Figure 5.1.

The content of main folders, `common`, `lowtemperature` and `material` will be, where the name is not self-explanatory, shortly discussed in the following.

- `common`: Header files which are not model-specific.

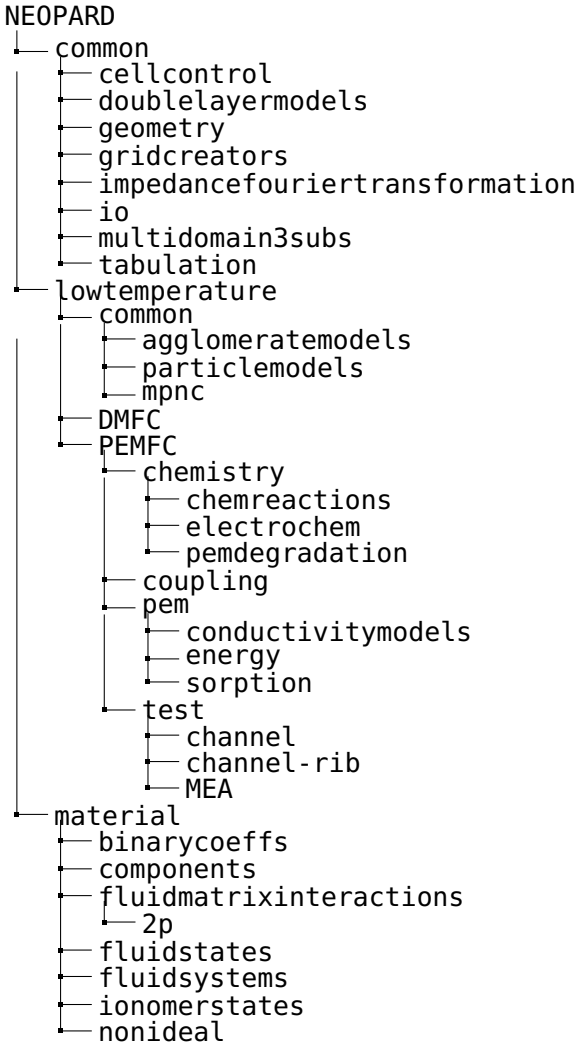

Figure 5.1: Directory tree of the NEOPARD-X framework.

  - `cellcontrol`: Galvano- or potentiostatic control of the cell.
  - `geometry`: Geometry information of the simulated cell.
  - `gridcreators`: Translation of the model geometry into a grid.
  - `impedancefouriertransformation`: Transformation of time-domain data of current and voltage into the frequency domain.
  - `io`: Header files required to write output.
  - `multidomain3subs`: The implementation of a multi-domain model consisting of three sub-domains.
  - `tabulation`: Header files for the tabulation of 2D and 3D functions with interpolation.
- `lowtemperature`: Models for low-temperature technologies (PEMFC, direct methanol fuel cell (DMFC), PEM-Electrolysis,...).
  - `common`: Models for the description of multi-phase flow, agglomerate models and models for the ionomer film resistance in the CLs.
  - `DMFC`: DMFC-specific models and test problems.
  - `PEMFC`: PEMFC-specific models and test problems: models for chemical and electro-chemical reactions, implementation of the coupling conditions between

porous electrodes and the membrane, transport models for the PEM, membrane conductivity models, sorption isotherms.

- `material`: Thermodynamic properties of components and phases and interaction between phases.
  - `binarycoeffs`: Interactions between components.
  - `components`: Thermodynamic properties of pure components.
  - `fluidmatrixinteractions`: Interactions between fluid phases and the solid.
  - `fluidstates`: State of fluids for given conditions (e.g. composition, pressure, temperature,...).
  - `fluidsystems`: Models for the calculation of the fluid states.
  - `ionomerstates`: State of the ionomer for given conditions (e.g. relative humidity, pressure, temperature,...).
  - `nonideal`: Models for the description of non-ideal mixing of components.

Algorithm 5.1 describes the time-stepping algorithm of a NEOPARD-X simulation. During the initialization, the following steps are executed:

1. Initialize the fuel cell geometry:
   - What is the geometry of the simulated cell?

Algorithm 5.1 Time-stepping algorithm of a NEOPARD-X simulation.

```
- initialize
for each time step do
    for each Newton iteration do
        for each element do
            - calculate local residual vector and Jacobian matrix
            - assemble into global residual vector and Jacobian
matrix
        end for
        - solve linear system
        - update solution
        - check for Newton convergence
    end for
    if Newton converged then
        - adapt time step size for the next time step
        - write result
    else
        - redo time step with smaller time step size
    end if
end for
- finalize
```

2. Create the grid based on the geometry information
   - How many elements are used to spatially discretize each layer?
   - Is grading of the grid desired? (see Section 5.2.3)
3. Initialize the cell control

- What is being simulated?
- Potentiostatic or galvanostatic simulation?
- Polarization curve, impedance, constant load operation, ...?

4. Initialize the fluid and ionomer systems of the model
   - Tabulate component properties
   - Initialize the NASA polynomial coefficients
   - Initialize the tabulated sorption isotherm
5. Divide the grid into sub-domains
6. Calculate the initial fluid states of the anode and cathode domain
7. Set the initial conditions
8. Create separate folder for simulation output

5.2 Discretization

To solve the equations presented in Chapter 4 numerically, they need to be discretized in time and space. For the spatial discretization, the so-called box method [80] was chosen and for the time discretization the fully implicit *Euler* scheme is applied. Both discretization schemes will be presented in the following sections.

5.2.1 Box Method

The information given in this section is taken from the Dumu^{X} handbook [3] and presented here for the sake of completeness.

The box method is a combination of the finite-volume (FV) and the finite-element (FE) method and unites the advantages of both: it is locally mass conservative and at the same time allows to use unstructured grids. With this method the modeling domain is discretized with a primary FE grid consisting of the nodes i which constitute the elements E_k. A secondary FV grid is constructed which forms boxes B_i surrounding the nodes by connecting the midpoints and barycenters of the elements surrounding i. These boxes are divided into subcontrolvolumes (scv's) b_i^k by the primary FE grid. Furthermore, the subcontrolvolumefaces (scvf's) e_{ij}^k between the scv's b_i^k and b_j^k having length $|e_{ij}^k|$ are required for the discretization. The resulting grids are depicted in Figure 5.2 along with the positions of the integration points x_{ij}^k on e_{ij}^k and the outer normal vector $\mathbf{n}_{ij}^k$.

With this discretization, it is possible to balance fluxes across the scvf's with the FV method while the FE gradients at the integration points are used for the calculation of these fluxes.

For an unknown field u, the discrete form of a general balance equation (Equation (4.3)) will be derived in the following. It is rewritten in integral form

$$f\left(u\right) = \int_{\Omega} \frac{\partial u}{\partial t} d\Omega + \int_{\Omega} \nabla \cdot \Psi\left(u\right) d\Omega - \int_{\Omega} q \, d\Omega = 0, \qquad (5.1)$$

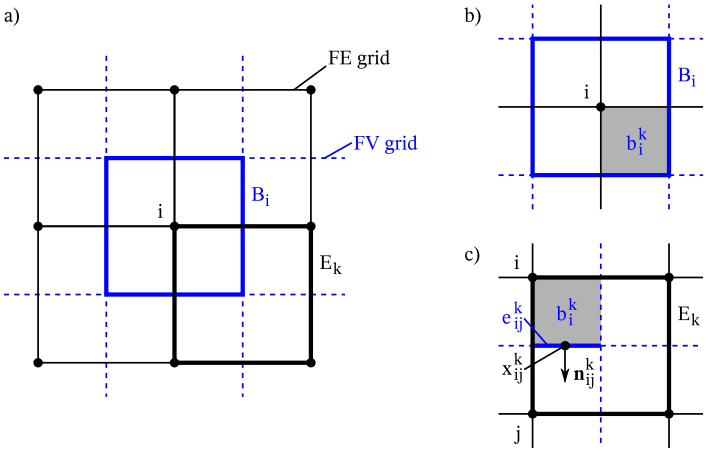

Figure 5.2: Spatial discretization with the box method, reproduced after [3].

where $F(u)$ is a flux due to gradients of u. At the integration point, an approximation $\tilde{u}\left(x_{ij}^k\right)$ of u is obtained using the discrete values at the nodes $\hat{u}_i$ and the linear basis function N_i.

$$\tilde{u} = \sum_i N_i \hat{u}_i \tag{5.2}$$

and the approximate gradient of u is calculated as

$$\nabla\tilde{u} = \sum_i \nabla N_i \hat{u}_i. \tag{5.3}$$

With these approximations, Equation (5.1) is no longer exactly fulfilled and an residual ϵ is produced:

$$f\left(\tilde{u}\right) = \epsilon \neq 0. \tag{5.4}$$

The principle of weighted residuals is expressed as

$$\int_{\Omega} W_j \epsilon \, d\Omega \stackrel{!}{=} 0, \tag{5.5}$$

where the the residual ϵ is multiplied with a weighting function W_j, $\sum_j W_j = 1$. It is claimed that this product vanishes when integrated over the whole domain (Equation (5.5)). Combination of Equation (5.1) and Equation (5.5) then yields

$$\begin{aligned} &\int_{\Omega} W_j \frac{\partial \tilde{u}}{\partial t} \, d\Omega + \int_{\Omega} W_j \left[\nabla \cdot \Psi\left(\tilde{u}\right)\right] \, d\Omega - \int_{\Omega} W_j q \, d\Omega \\ &= \int_{\Omega} W_j \epsilon \, d\Omega \stackrel{!}{=} 0 \end{aligned} \tag{5.6}$$

which is rewritten using the *Green-Gauss* theorem and the chain rule to obtain

$$\begin{aligned} &\int_{\Omega} W_j \frac{\partial \sum_i N_i \hat{u}_i}{\partial t} \, d\Omega + \int_{\partial\Omega} \left[W_j \Psi\left(\tilde{u}\right)\right] \mathbf{n} \, d\Gamma_{\Omega} \\ &- \int_{\Omega} \nabla W_j \Psi\left(\tilde{u}\right) \, d\Omega - \int_{\Omega} W_j q \, d\Omega = 0 \end{aligned} \tag{5.7}$$

Choosing a piecewise constant weighting function W_j inside B_i causes the the third term of Equation (5.7) to vanish. Therefore, the weighting function $W_j(x)$ at the location x is expressed as

$$W_j(x) = \begin{cases} 1 \; \forall \; x \in B_i \\ 0 \; \forall \; x \notin B_i \end{cases} \tag{5.8}$$

Further, a mass lumping technique is applied which allows the integral $M_{ij} = \int_\Omega W_j N_i \; d\Omega$ to be replaced by the mass lumping term M_{ij}^{lump} which is written as

$$M_{ij}^{lump} = \begin{cases} \int_\Omega W_j \; d\Omega = \int_\Omega N_i \; d\Omega = V_i & \textbf{if } i = j \\ 0 & \textbf{if } i \neq j \end{cases} \tag{5.9}$$

where V_i is the volume of box B_i. With $W_j = 1$ this gives the discrete form of Equation (5.1):

$$V_i \frac{\partial \hat{u}_i}{\partial t} + \int_{\partial B_i} \Psi \left(\tilde{u} \right) \mathbf{n} \; d\Gamma_{B_i} - V_i \cdot q = 0. \tag{5.10}$$

5.2.2 Modeling Domain

For the spatial 2D discretization of the fuel cell, the geometry depicted in Figure 5.3 is used, which is a simplified along-the-channel geometry in co-flow mode.

In counter-flow mode, the locations of the in- and outlet domains of the cathode side are exchanged and the cathode outlet tube points to the top. The geometry is described by the domain lengths l in the y-direction and the layer thicknesses d in the

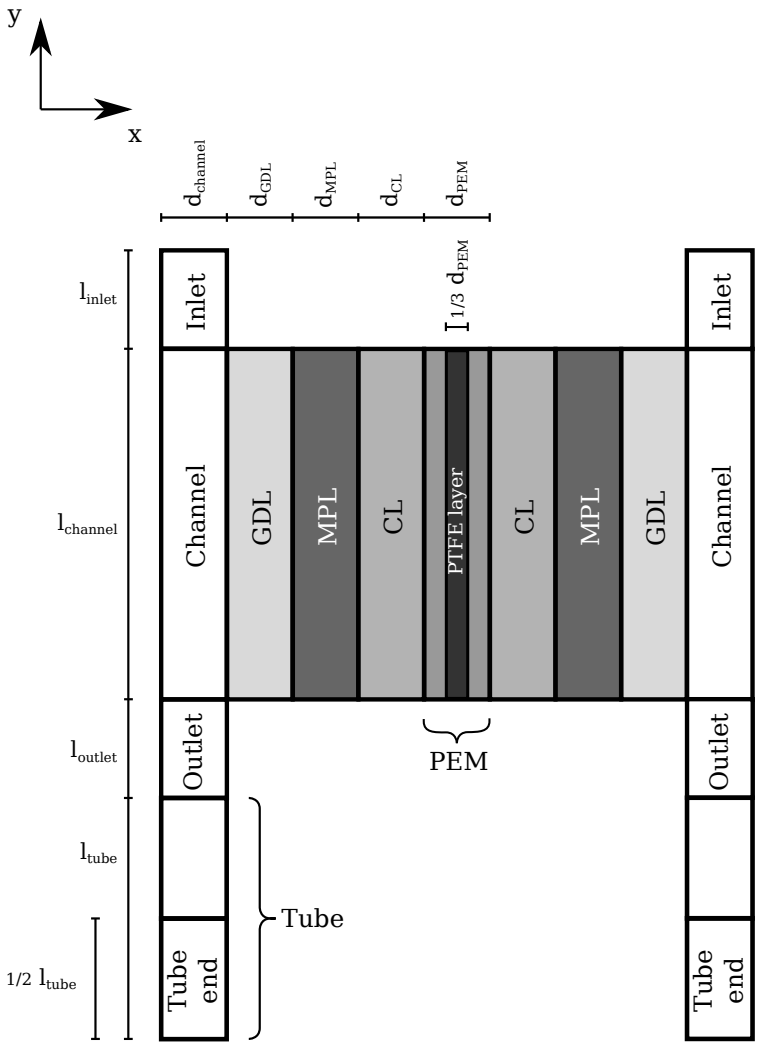

Figure 5.3: Geometry of the modeling domain. Not drawn to scale.

x-direction. The thicknesses for each layer are allowed to differ for the anode and cathode side of the cell. Typically, the extend of the modeling domain in y-direction is in the meter range, while the total thickness in x-direction is three orders of magnitude lower. In the center of the PEM, a PTFE layer may be present which enhances the membrane stability. Therefore, in this region, the volume fraction of the polymer may be reduced. The geometry can be divided into a domain describing the fuel cell and supplementary domains necessary for the numerical model. These supplementary domains will be discussed in the following.

In perspective, an advanced formulation for the transport in the gas channels, e.g. the *Navier-Stokes* equation may be used. Therefore, an inlet domain is added to the geometry of the cell which may be needed to obtain a fully developed velocity profile at the real cell inlet. Since in counter-flow, the y-coordinate of the cathode inlet corresponds to the y-coordinate of the anode outlet and vice versa, an outlet domain is added after the real cell exit. This allows to easily switch the geometry, and therefore, the operating mode from co- to counter-flow.

For the outflow boundary condition described in Section 4.7.2, a fully developed flow is required on the outflow boundary. To ensure this, a long tube is added to the modeling domain following the outlet domain. In the tube end domain, an increased temperature of 393.15 K is set as a *Dirichlet* condition on the boundaries. This way, all liquid water that may be present in the tube is evaporated before it reaches the tube outlet. This is required to further ensure the numerical stability of the outflow boundary condition. The increased temperature in the tube end

does not influence the solution inside the simulated cell since energy transport is purely convective in the inlet, outlet tube and channel domains.

Since the pressure boundary condition is set at the outlets of the tube, a high tube permeability ($\mathbf{K}_{tube} = 100 \times \mathbf{K}_{channel}$) is used to reduce the pressure build-up in the real cell due to transport along the tube length.

5.2.3 The Grid Creator

To mesh the modeling domain described in last section, a so-called grid creator was implemented. It is used to calculate the coordinates of the grid vertices and to connect these vertices to cells on which the simulation is carried out. This is done based on the geometrical information of the cell provided by the user. The different lengths and layer thicknesses depicted in Figure 5.3 need to be provided. In Algorithm 5.2, the algorithm of the grid creator is presented.

In order to keep the grid closed, the geometry is divided into domains for each dimension. Each of these domains is then divided into arbitrary number of cells in the corresponding dimension. Making use of the multidomaingrid capabilities [127] [126], the sub-domain grids are “carved” from the resulting grid. The whole process is sketched in Figure 5.4.

The grid creator has the capability to produce a so-called graded grid. This means that the discretization lengths for each domain and dimension may vary. This may be applied to obtain a finer

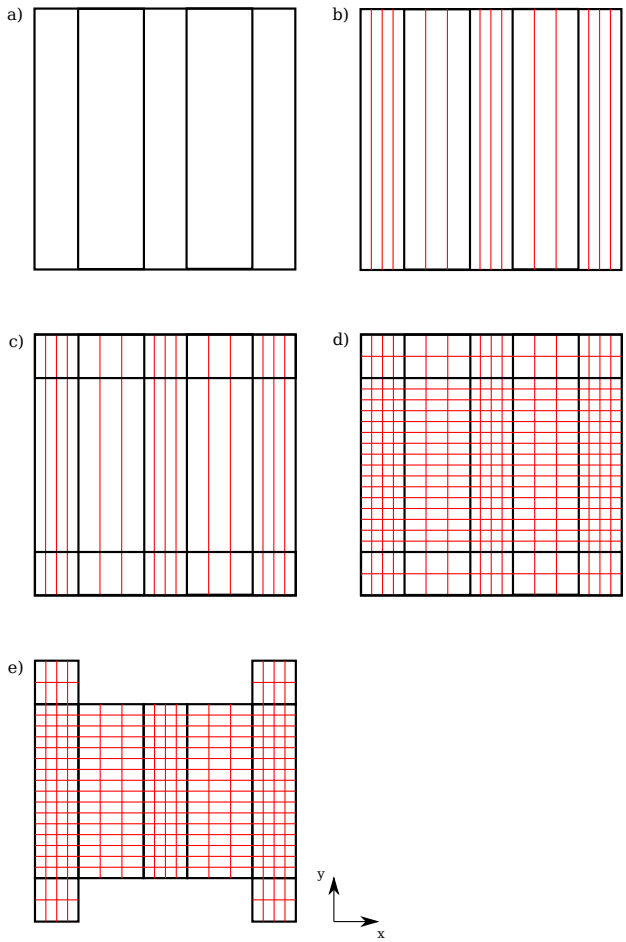

Figure 5.4: Sketch of the grid creation process in 2D. a) Domain discretization in x-direction. b) Element discretization in x-direction. c) Domain discretization in y-direction. d) Element discretization in y-direction. e) “Carving” of the sub-domain grids.

Algorithm 5.2 The grid creation algorithm.

for each dimension **do**
  for each domain **do**
    - assign element discretization lengths
    - determine spatial coordinates of the element vertices
  end for
end for
- place vertices
- construct elements

spatial discretization towards certain interfaces. Also, double grading may be used, meaning that discretization lengths in one dimension may first get larger and then smaller again or vice versa. An example of a grid with grading and double grading in different domains is depicted in Figure 5.5.

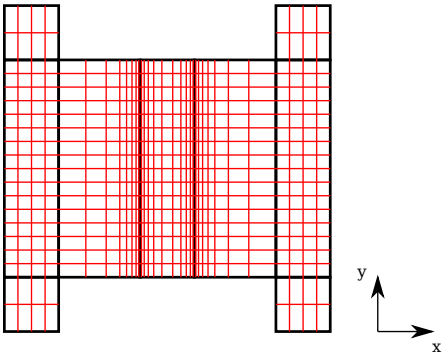

Figure 5.5: Sketch of a graded grid with refinement towards the central domain and double grading inside the central domain.

Grading is controlled by the value of the grading factor $f_i \in (-\infty, -1) \veebar (1, \infty)$ of domain i, where negative values indicate that the cells get smaller in positive direction of the domain and positive values indicate the opposite. The absolute value of f_i determines the discretization length ratio between the cells of i.

The parameter $n_i \in \mathbb{N}$ represents the total number of cells in a domain i. If grading is applied and $f_i < 1$, the discretization length of the cell with index k, $k \in [0, n_i - 1]$ is calculated as

$$h^k = h_{min,i} |f|^{(n_i - 1 - k)}, \tag{5.11}$$

If $f_i > 1$, the discretization lengths are determined via

$$h^k = h_{min,i} f^k, \tag{5.12}$$

where

$$h_{min,i} = d_i \frac{1 - |f_i|}{1 - |f_i|^{n_i}}. \tag{5.13}$$

The parameter d_i denotes the spatial extent of domain i in the considered dimension.

If double grading is applied, the domain is split in two halves. Then, for each half, the discretization lengths are calculated with $\tilde{n}_i = \frac{1}{2} n_i$ and $\tilde{d}_i = \frac{1}{2} d_i$ according to Equations (5.11)-(5.13). In this case, if $\tilde{n}_i \neq\in \mathbb{N}$, $\tilde{n}_i$ is rounded down.

With a graded grid, the spatial resolution can be increased locally. In parts of the modeling domain where the solution is uncritical with respect to the investigated phenomena, a coarser grid can be used, which strongly increases the efficiency of the simulations.

5.2.4 Time Discretization

For the discretization in time, an implicit *Euler* scheme is applied. The solution of the simulated problems is calculated at discrete points in time t^n, where the superscript n denotes the considered time level. The next point in time is

$$t^{n+1} = t^n + \Delta t, \tag{5.14}$$

where the temporal discretization length Δt is adaptive. To obtain the solution at t^{n+1}, Equation (5.10) is then written as

$$V_i \frac{\hat{u}_i^{n+1} - \hat{u}_i^n}{\Delta t} + \int_{\partial B_i} \Psi\left(\tilde{u}^{n+1}\right) \mathbf{n}\, d\Gamma_{B_i} - V_i \cdot q^{n+1} = 0. \tag{5.15}$$

For determination of the time step size Δt^{new}, an heuristic time step estimator is used. It is based on the number of *Newton* iterations k needed to achieve the convergence criterion and the old time step size Δt^{old}. A target number of *Newton* iterations

Algorithm 5.3 Time step estimation algorithm

if $k > k^{target}$ **then**
  $percent \leftarrow \left(k - k^{target}\right) / k^{target}$
  $\Delta t^{new} \leftarrow \Delta t^{old} / \left(1 + percent\right)$
else
  $percent \leftarrow \left(k^{target} - k\right) / k^{target}$
  $\Delta t^{new} \leftarrow \Delta t^{old} \left(1 + percent / c^{dampening}\right)$
end if

k^{target} is set and a maximum number of iterations k^{max} is defined. With these values, the time step size is determined using Algorithm 5.3.

In this algorithm $c^{dampening}$ represents a dampening factor which can be adjusted to increase the temporal resolution of the simulation. This is an important model feature for the simulation of electrochemical impedance spectra (EIS) since a high temporal resolution is needed to reduce oscillations in the frequency domain data obtained by *Fourier* transformation. The details of the impedance simulations will be presented in Section 5.4.

5.2.5 Coupling Conditions

Numerically, the modeling domain depicted in Figure 2.1, is divided into three sub-domains: the anode-, membrane- and cathode sub-domain. Since different transport mechanisms are considered in the membrane and the porous electrodes, coupling conditions for the conservation equations need to be formulated

at the interfaces. Figure 5.6 shows the interface between the PEM and CCL, discretized with the box method [11, 80].

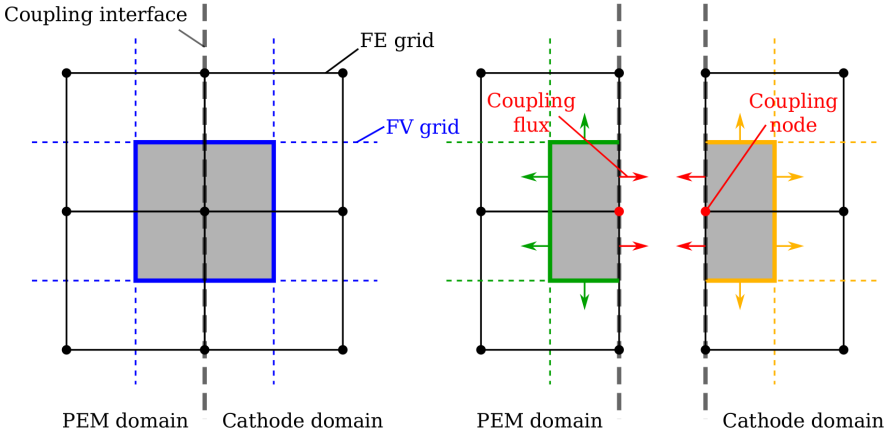

Figure 5.6: Discretization of the coupling interfaces with the box-method, reproduced after [11].

The coupling conditions considered in this work are *Dirichlet* type conditions and *Neumann* type conditions.

For a *Dirichlet* type condition, the value of a primary variable is set at the coupling nodes. It is calculated from the solution of the other sub-domain. Numerically, the local residual of the corresponding sub-control volumes is replaced by the difference of the boundary condition and the value of the primary variable. For a converged solution, this difference will vanish.

In case of a *Neumann* type condition, the flux over the coupling interface is used as boundary condition. First, the local residual inside the first sub-domain is calculated without consideration of

the interface flux. This value is then passed as a flux boundary condition to the other domain.

In this work, for all conservation equations *Dirichlet* type conditions are set on the interface nodes in the PEM domain and *Neumann* type conditions are applied on the coupling interfaces in the electrode domains.

5.3 Open Circuit Voltage and Polarization Curve Simulation

Ideally, the OCV of the cell corresponds to the *Nernst* voltage of the ORR (Equation (2.14) on page 12). However, in reality, a strongly reduced OCV is observed ($\sim$ 0.95 V) resulting from the cross-over of hydrogen which leads to a small short circuit current [179]. Since this mechanism is incorporated into the model, the OCV can be predicted by the simulation. To obtain the OCV, a simulation in galvanostatic mode at a net current density equal to zero is carried out until steady state is reached. The simulated cell voltage at steady-state is equivalent to the predicted OCV.

Since the model is transient, a polarization curve can be simulated using a slow ramp of the cell current density in galvanostatic mode. The slope of the ramp is about 0.01 A m^{-2} s^{-1}. In potentiostatic mode, the cell voltage is slowly ramped down at a rate of about 10^{-6} V s^{-1}. This way, the fuel cell is always at a pseudo-steady-state.

5.4 Impedance Simulations

For the simulation of impedance spectra in potentiostatic mode, the potential step method [20] is used. First the cell voltage is ramped to the desired value and held constant until steady-state is reached. Then, the voltage is ramped down rapidly (0.5 mV in 10^{-9} s) and subsequently held constant for 10^4 s. Since the potential step is faster than the fastest process inside the cell and the hold duration is longer than the relaxation time of the slowest process, all frequencies of an impedance spectrum are resolved. At the end of the simulation, the time domain data of current and voltage are converted into frequency domain data via a *Fourier transformation*.

With the simulation described above, time domain data of the cell voltage $V\left(t\right)$ and current density $i\left(t\right)$ are obtained at N discrete time points t^n. The start time of the voltage ramp is defined as $t^0 = 0$. Before the transformation, from both, the current density and voltage data points, the corresponding steady-state value at t^0 is subtracted.

Further, an artificial additional data point is added at $t = 2t^N$ where for $V\left(2t^N\right) = 0$ and $i\left(2t^N\right) = 0$. This may be interpreted as a very slow ramp driving the system back to the original state [20].

The complex impedance $Z^*\left(\upsilon\right)$ at frequency υ is obtained from complex division:

$$Z^*\left(\upsilon\right) = \frac{V^*\left(\upsilon\right)}{i^*\left(\upsilon\right)}. \tag{5.16}$$

The frequency-domain function $H^*(\upsilon)$ of an arbitrary quantity is calculated from the time-domain data $H(t)$ using the *Fourier* transform

$$H^*(\upsilon) = \int_{-\infty}^{\infty} H(t) \exp(-j2\pi\upsilon t)\, dt, \tag{5.17}$$

where $j = \sqrt{-1}$. Equation (5.17) is then rewritten as [192]

$$H^*(\upsilon) = \sum_{n=1}^{N-1} \int_{t^n}^{t^{n+1}} H(t) \exp(-j2\pi\upsilon t)\, dt. \tag{5.18}$$

Replacing $H(t)$ with a linear interpolation between two given points allows to solve Equation (5.18) analytically, yielding

$$\begin{aligned} H^*(\upsilon) = & \frac{j}{(2\pi\upsilon)^2} \\ & \sum_{n=1}^{N-1} \left[(-ja_n + 2\pi\upsilon b_n + 2\pi\upsilon a_n t_{n+1}) \right. \\ & \times \exp(-j2\pi\upsilon t_{n+1}) \\ & - (-ja_n + 2\pi\upsilon b_n + 2\pi\upsilon a_n t_n) \\ & \left. \times \exp(-j2\pi\upsilon t_n)\right], \end{aligned} \tag{5.19}$$

where $a_n = (H_{n+1} - H_n) / (t_{n+1} - t_n)$ and $b_n = H_n - a_n t_n$.

This way, a complete impedance spectrum is obtained at the desired cell voltage. In galvanostatic mode, a step in current

density (20 A m^{-2} in 10^{-9} s) is used to obtain the the impedance spectrum at a the desired current density.

During impedance simulation, the inlet fluxes are kept constant in accordance with the experiments.

5.5 Input File

In this section, the possibilities to control the simulations from the input file are presented. The input file is divided into different sections with their corresponding parameters. The functionality of the most important sections will be explained along with the corresponding parameters.

`[OperatingConditions]`: The simulated operating conditions.

- `GasPressureAnodeOutlet`: The back pressure at the anode.
- `GasPressureCathodeOutlet`: The back pressure at the cathode.
- `InitialTemperature`: The initial- and *Dirichlet* value for the temperature.
- `RelativeHumidityAnode`: The relative humidity in the anode gas stream.
- `RelativeHumidityCathode`: The relative humidity in the cathode gas stream.
- `CoFlow`: Triggers co- or counter-flow operation.
- `LambdaH2`: The lambda-control parameter for hydrogen.

- `Lambda02`: The lambda-control parameter for oxygen.

`[TimeManager]`: Manages the time discretization.

- `DtInitial`: The initial time step size for the simulation.
- `MaxTimeStepSize`: The maximum time step size for the simulation.
- `Restart`: Specifies whether the simulation should be restarted from the state of a former simulation.

`[CellControl]`: Specifies the load- or voltage profile.

- `ControlString`: A string which is translated into a load- or voltage profile. It is composed of human readable sub-strings corresponding to different operations (e.g. hold, ramp or impedance). Further, loops may be used to repeat sequences of sub-strings which makes it possible to conveniently simulate e.g. thousands of potential cycles.
- `OperatingMode`: Potentio- or galvanostatic simulation.

`[CellGeometry]`: Controls the model geometry. Here, the lengths and thicknesses depicted in Figure 5.3 are specified.

`[Grid]`: Controls the spatial discretization of the geometry. Sets the number of cells in each domain and dimension along with the corresponding grading factors.

`[SpatialParams]`: Specifies contact angles, permeabilities, porosities, representative pore radii, electrical- and thermal conductivities for each layer of the fuel cell.

`[ORR]`: The kinetic parameters of the ORR.

`[HOR]`: The kinetic parameters of the HOR.

`[CLConductivity]`: The parameters for the ionic conductivity model in the CLs.

`[ImpedanceFourierTransformation]`: The parameters for the *Fourier* transformation.

- `MinFrequency`: The minimum frequency considered in the transformation.
- `NFreqDecades`: The number of frequency decades .
- `NFreqPerDecade`: The number of frequencies per decade.

`[TabulatedLambda]`: The parameters for the tabulated sorption isotherm of the ionomer.

`[Newton]`: The parameters for the *Newton* method.

- `MaxRelativeShift`: The maximum of the relative shift of the primary variables triggering convergence of the *Newton* method.
- `ResidualReduction`: The maximum of the residual of a balance equation triggering convergence of the *Newton* method.
- `WriteConvergence`: Writes diagnostic output for each *Newton* iteration.
- `TargetSteps`: The target number of *Newton* steps. This parameter is used to steer the adaption of the time step size (see Algorithm 5.3).

- `TimeStepDampeningFactor`: Used to damp the increase of the time step during impedance simulation (see Section 5.2.4).

`[ModelAnalysis]`: Parameters for in-depth analysis of the model.

- `DisableChannel`: Specifies whether channel transport should be considered in the simulation.

`[Vtk]`: Controls the output. The output of certain quantities like fluxes or secondary variables can be switched on or off conveniently.

- `SimulationName`: Used to name the different output files which are written to disk by the simulation.

`[Output]`: Controls the amount of output written by the simulation.

6 Results - Performance

> It simply isn't an adventure worth telling if there aren't any dragons.
>
> *(J.R.R. Tolkien)*

In this chapter, the results of the fuel cell performance model will be presented. In Sections 6.1 and 6.2 a convergence study and the model validation will be presented respectively. In Section 6.3, the simulated impedance spectra are investigated in detail. From this systematic analysis, the processes constituting the features of the impedance spectra are revealed. For further validation, the simulated impedance spectra are compared to experiments.

6.1 Convergence Study

A study, testing the grid convergence, was carried out. In a first step, the spatial discretization is increased homogeneously until convergence is achieved. Subsequently, the domains, which are critical for the solution and therefore require high spatial resolution, are identified. Based on this analysis, a locally fine

Table 6.1: Convergence study simulations.

Nr.	n_{cells} per layer type through-plane	n_{cells} along the channel in-plane	n_{cells} total	CPU-time / s
1	3	10	270	2.9×10^2
2	6	20	1080	1.7×10^3
3	12	40	4320	8.3×10^3
4	24	80	17280	4.7×10^4

grid can be used where needed and a coarse one may be applied to the uncritical regions in order to improve the computational performance of the model.

For the convergence study, the simulations listed in Table 6.1 were carried out. The number of cells per layer type, along the channel and the total number of cells along with the corresponding central processing unit (CPU)-time are given. The number of cells in the inlet-, outlet- and tube domains is left unchanged throughout this study as the influence on the solution is negligible.

To indicate the convergence, the change of the polarization curve with changing spatial discretization is monitored. For this purpose, galvanostatic polarization curves were simulated and the change of the cell voltage at OCV and current densities of 1000, 2000, 4000, 6000, 8000, and 10000 A m^{-2} was investigated. The operating conditions correspond to the values of condition **1** of Table 6.2 and the parameters listed in Table 6.3 were used.

Figure 6.1 shows the comparison of the simulations **1**-**4**. Depicted is the absolute value of the voltage difference between simulation **4** and simulations **1**,**2** and **3** respectively.

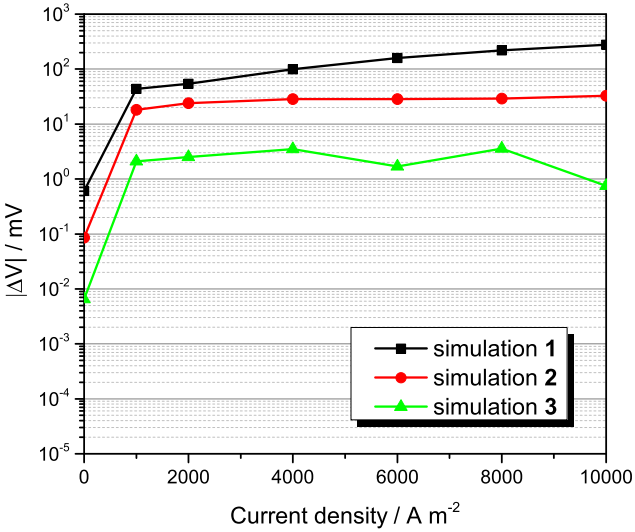

Figure 6.1: Influence of uniform grid refinement on the simulated polarization curve.

It can be observed that the voltage difference exhibits a minimum at OCV and increases with the cell current density or simulation time for simulations **1** and **2**. For simulation **3**, this trend is not observed. Further, the discretization error decreases with higher spatial discretization. For simulation **3**, the maximum voltage difference is below 4 mV which is within the range of the experimental error. Since this work is focused on the understanding of the processes which govern the fuel cell performance, simulation **3** is considered as a converged solution.

Subsequently, exploiting the grid creator capabilities (Section 5.2.3), the spatial discretization of the different layers in x-direction and along the channel in y-direction is changed individually in order to identify critical and uncritical domains.

Simulations with 3, 6, 12 and 24 cells in a specific layer were performed. Further, to investigate the influence of discretization along the channel, simulations with 10, 20, 40 and 80 cells in y-direction were carried out. In all cases, the remaining domains were left coarse. For each layer type and the y-direction, the obtained polarization curves were compared with simulation **3**. The results are depicted in Figures 6.2, 6.3 and 6.4.

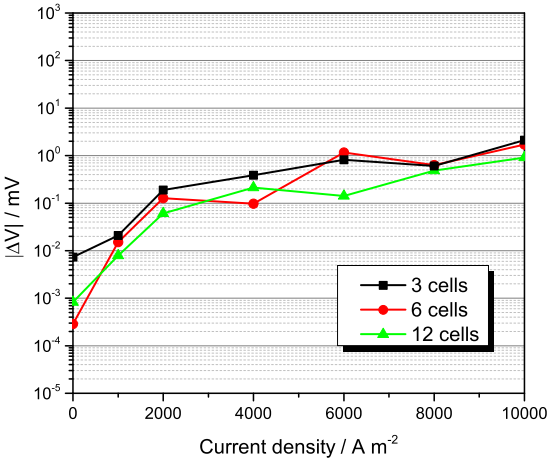

(a) Channels.

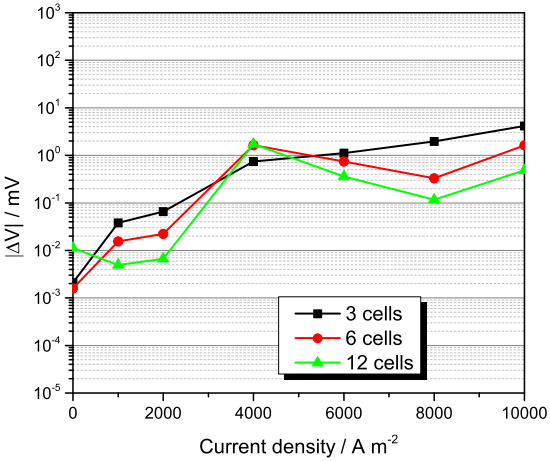

(b) GDLs.

Figure 6.2: Influence of spatial discretization in the GCs and GDLs.

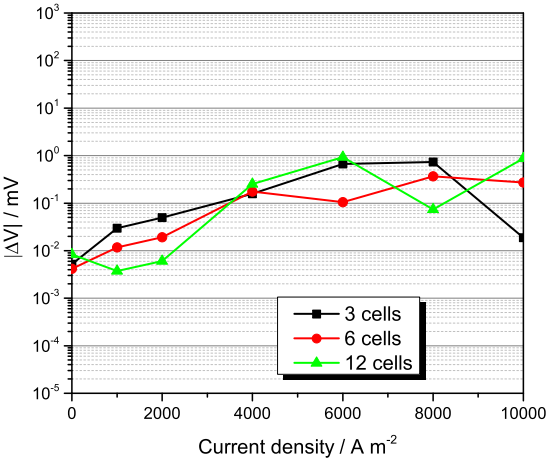

(a) MPLs.

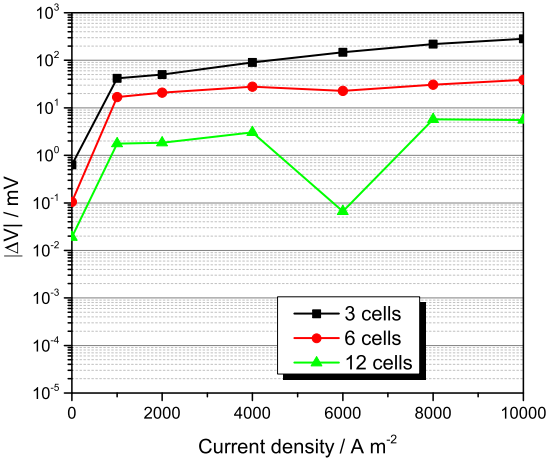

(b) CLs.

Figure 6.3: Influence of spatial discretization in the MPLs and CLs.

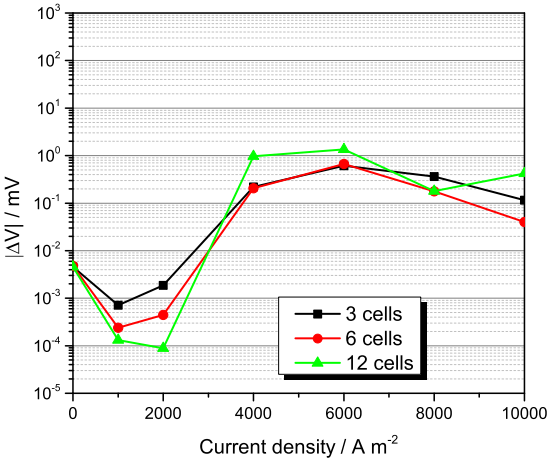

(a) PEM.

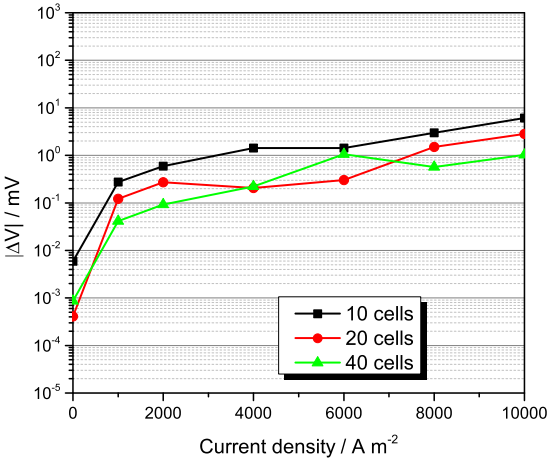

(b) Along the channel.

Figure 6.4: Influence of spatial discretization in the PEM and along the channel.

It can be observed, that finer discretization in the channels, MPLs, and PEM in the through-plane direction has a negligible influence on the solution. The maximum voltage difference, is observed for the GDL. It is below 4 mV (Figure 6.2b), which is again below the experimental error. Also, the discretization along the channel plays a minor role. For the simulation with 10 cells along the channel, the maximum voltage difference is $\sim$ 6 mV (Figure 6.4b). However, for the catalyst layers, a finer discretization is mandatory. Increasing the number of cells in the CLs from 3 to 12 reduces the maximum voltage difference from $\sim$ 280 to 5.5 mV (Figure 6.3b).

The polarization curves with 3, 6, 12, and 24 cells in the CLs are depicted in Figure 6.5.

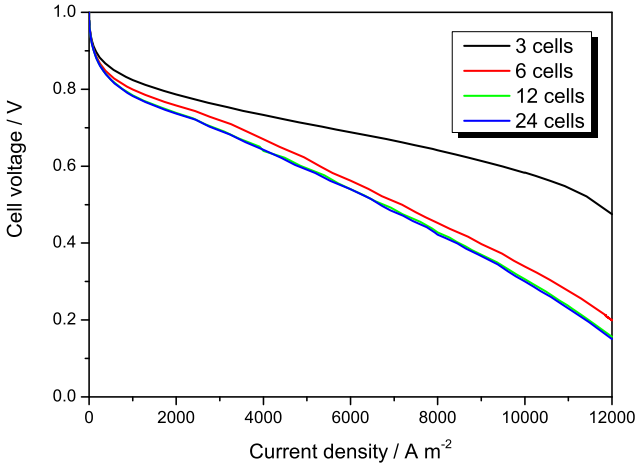

Figure 6.5: Polarization curves with varying spatial discretization of the CLs.

With finer discretization, the cell performance decreases significantly until convergence is achieved. This can be understood if the plot of the ionic potential inside the CCL, depicted in Figure 6.6 is considered.

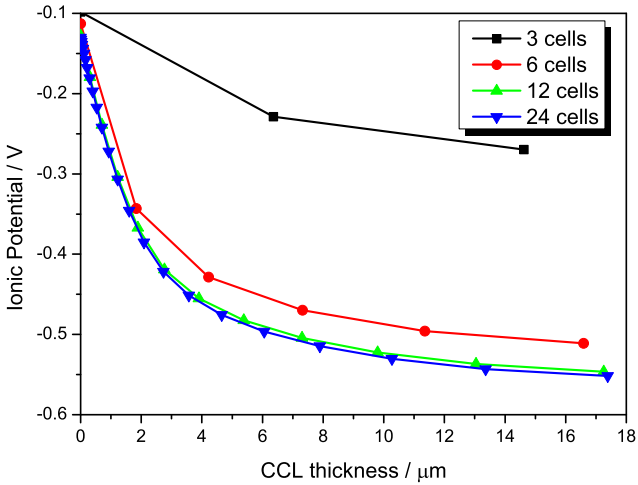

Figure 6.6: Through-plane cut through CCL in the center of the channel at a current density of 12000 A m^{-2}.

Under the simulated conditions, strong potential gradients in the CCL exist due to the low relative humidity and the consequently low ionic conductivity of the catalyst layer ionomer. For the coarse discretization, these gradients in the through-plane direction are not well resolved. Further, the control-volume in the CCL next to PEM is large in comparison with the more finely discretized simulations. This results in an underestimation of the ORR overpotential in a significant part of the catalyst layer and therefore an overestimation of the cell performance. This

effect is less pronounced if the relative humidity is higher. In case of higher humidity, a coarser discretization of the CLs might be applicable.

From the results presented in Figures 6.2, 6.3, 6.4, 6.5 and 6.6, follows that the catalyst layers are the most critical domains of the given fuel cell model. Consequently, a simulation where only the CLs are discretized with 12 cells and all other layers, as well as the discretization along the channel are left coarse is performed and compared to the solution of simulation **4** (see Figure 6.7).

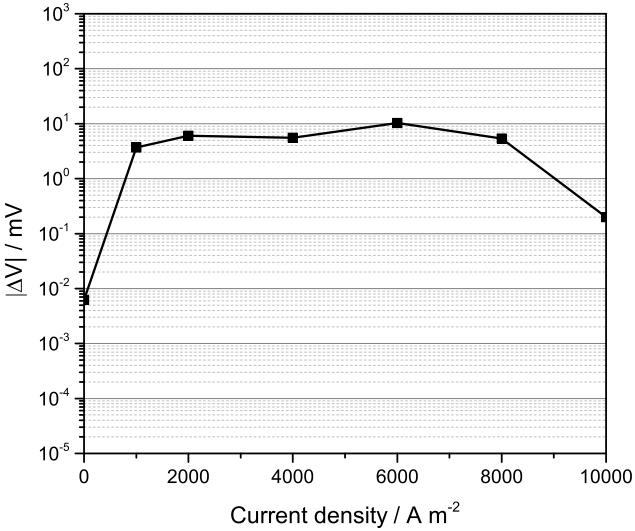

Figure 6.7: Comparison of simulation **4** and a simulation on a coarse grid with 12 cells in the CLs.

The maximum voltage difference in this comparison is $\sim$ 10 mV while the CPU-time is reduced by two orders of magnitude from 4.7×10^4 s to 5×10^2 s. This proves the extreme computational efficiency of the model. As a consequence, in the following, simulations on a coarse grid with fine discretization in the CLs are performed since the resulting error is small.

It should be noted, that for this convergence study, a grading factor of -1.3 and 1.3 (see Table 6.3) was applied for the discretization of the anode and cathode catalyst layer respectively. Therefore, the spatial resolution of the grid close to the PEM/CL interfaces is increased which helps to resolve the strong potential gradients which may occur in this region. A further analysis of the influence of the grading factor was not performed.

From the results presented above, it can be concluded that spatial resolution of the catalyst layers is of extreme importance for the present fuel cell model. Models which do not resolve these layers good enough will not be able to capture the relevant physics of the cell and the corresponding modeling results will not be realistic.

6.2 Model Validation

For validation, the model is compared to experimentally measured polarization curves and impedance spectra. The measurements where all carried out in co-flow mode at $80°$C with varying back pressure, relative humidity and lambda control parameters. The operating conditions are listed in Table 6.2.

Table 6.2: Experimental operating conditions.

Condition	$p_{anode/cathode}$ / Pa	RH / %	$\lambda^{flux,\mathrm{H_2/O_2}}$ / -
1	$1.46 \times 10^5/1.427 \times 10^5$	30	1.5/2
2	$1.46 \times 10^5/1.427 \times 10^5$	50	1.5/2
3	$1.46 \times 10^5/1.427 \times 10^5$	90	1.5/2
4	$2 \times 10^5/2 \times 10^5$	50	1.5/2
5	$1.46 \times 10^5/1.427 \times 10^5$	50	4/4

The model parameters used for the simulations are given in Table 6.3.

Table 6.3: Model parameters used for model validation.

Parameter	Units	Reference
Operating mode:		
co-flow		
Cell geometry:		
$A_{cell} = 1.243$	m^2	measured
$A_{inlet} = 0.35 \times 10^{-3}$	m^2	measured
$d_{channel} = 0.7 \times 10^{-3}$	m	measured
$d_{GDL} = 150 \times 10^{-6}$	m	estimated
$d_{MPL} = 50 \times 10^{-6}$	m	estimated
$d_{CL,anode} = 7 \times 10^{-6}$	m	estimated
$d_{CL,cathode} = 20 \times 10^{-6}$	m	estimated
$d_{PEM} = 27.5 \times 10^{-6}$	m	[4]

Table 6.3: Model parameters used for model validation continued.

Parameter	Units	Reference
$l_{channel} = 1.243$	m	measured
$l_{inlet} = l_{outlet} = 0.1$	m	
$l_{tube} = 2.5$	m	
Grid:		
$n_{cells,x,channel} = 3$		
$n_{cells,x,GDL} = 3$		
$n_{cells,x,MPL} = 3$		
$n_{cells,x,CL,anode} = 15$		
$n_{cells,x,CL,cathode} = 10$		
$n_{cells,x,PEM} = 3$		
$n_{cells,y,cell} = 10$		
$n_{cells,y,inlet} = n_{cells,y,outlet} = 2$		
$n_{cells,y,tube} = 12$		
$f_{grading,x,CL,anode} = -1.3$		
$f_{grading,x,CL,cathode} = 1.3$		
$f_{grading,y,tube} = d1.5$		
Spatial parameters:		
$\mathbf{K}_{channel} = \mathbf{K}_{inlet} = \mathbf{K}_{outlet} = 1.23 \times 10^{-8}$	m^2	fitted
$\mathbf{K}_{GDL} = 1.8 \times 10^{-11}$	m^2	estimated
$\mathbf{K}_{MPL} = 3.33 \times 10^{-15}$	m^2	estimated
$\mathbf{K}_{CL} = 2 \times 10^{-15}$	m^2	estimated

Table 6.3: Model parameters used for model validation continued.

Parameter	Units	Reference
$\mathbf{K}_{tube} = 100 \times \mathbf{K}_{channel}$	m^2	
$\phi_{channel} = \phi_{inlet} = \phi_{outlet} = \phi_{tube} = 1$		
$\phi_{GDL} = 0.625$		estimated
$\phi_{MPL} = 0.25$		estimated
$\phi_{CL} = 0.38$		estimated
$r_{pore,channel} = r_{pore,tube} = 1 \times 10^{-3}$	m	estimated
$r_{pore,inlet} = r_{pore,outlet} = 1 \times 10^{-3}$	m	estimated
$r_{pore,GDL} = 2.5 \times 10^{-6}$	m	estimated
$r_{pore,MPL} = 30 \times 10^{-9}$	m	estimated
$r_{pore,CL} = 20 \times 10^{-9}$	m	estimated
$\theta_{channel} = \theta_{inlet} = \theta_{outlet} = \theta_{tube} = 112$	°	estimated
$\theta_{GDL} = 104$	°	[94]
$\theta_{MPL} = 94$	°	[94]
$\theta_{CL} = 93$	°	estimated
$\phi_{ion,CL} = 0.4$		estimated
$\phi_{ion,PEM} = 1$		
Lambda control:		
$i_{min} = 2000$	$A\ m^{-2}$	
$\lambda^{flux,O_2} = 2/4$		
$\lambda^{flux,H_2} = 1.5/4$		

Table 6.3: Model parameters used for model validation continued.

Parameter	Units	Reference
ORR:		
$i^0_{ref} = 2.8 \times 10^{-3}$	A m^{-2}	fitted
$E_{act} = 2.77 \times 10^4$	J mol^{-1}	[140]
$\alpha^f_{high} = \alpha^r_{high} = 0.5$		[140]
$\alpha^f_{low} = \alpha^r_{low} = 0.25$		fitted
$\eta^{\text{ORR}}_{trans} = 0.76$	V	fitted
Platinum oxide:		
$E^{0,\text{PtOx}} = 0.81$	V	fitted
$\alpha^{\text{PtOx}} = 0.5$		fitted
$k^{\text{PtOx}} = 0.0128$	s^{-1}	fitted
HOR:		
$i^{0,\text{HOR}} = 3 \times 10^3$	A m^{-2}	[130]
$\alpha^f = \alpha^r = 0.5$		[130]
ECSA:		
$\epsilon = 0.75$		[105]
$m_{\text{Pt},anode} = m_{\text{Pt},cathode} = 2 \times 10^{-3}$	kg m^{-2}	measured
$r_{\text{Pt},anode} = 2.5 \times 10^{-9}$	m	estimated
$r_{\text{Pt},cathode} = 3.52 \times 10^{-9}$	m	estimated
$\rho_{\text{Pt}} = 2.145 \times 10^4$	kg m^{-3}	

Table 6.3: Model parameters used for model validation continued.

Parameter	Units	Reference
Double layers:		
$C_{DL,anode} = C_{DL,cathode} = 3.4 \times 10^7$	F m^{-3}	fitted
CL conductivity:		
$A = 1.5 \times 10^{-2}$	S m^{-1}	fitted
$B = 2$		fitted
$C = 5$		fitted
Ionomer film model:		
$\delta_{ion} = 7 \times 10^{-9}$	m	fitted
$A = 100$	s m^{-1}	fitted
$B = 9 \times 10^3$	s m^{-1}	fitted
$C = -3.5$		fitted

Figure 6.8 shows the experimental and simulated polarization curves for the test conditions **1-3**.

In these experiments and simulations, the relative humidity is set to 30%, 50% and 90% for test cases **1**, **2**, and **3** respectively. It can be observed that for the dry conditions of test case **1**, the cell performance is lowest and increases with increasing humidification. This can be explained by improved conductivity of the ionomer (Equation (4.13) on page 39, Equation (4.41)

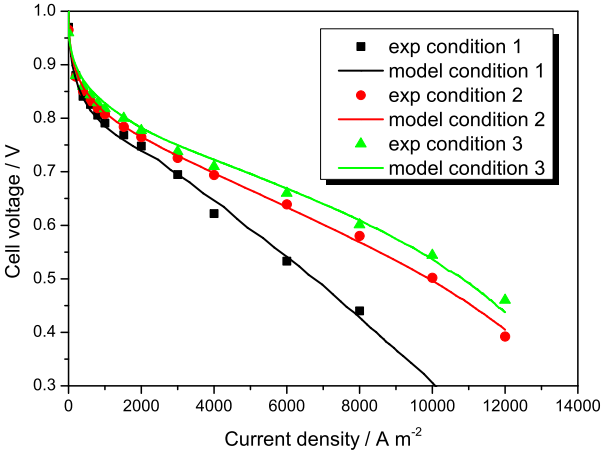

(a) Linear current density scale.

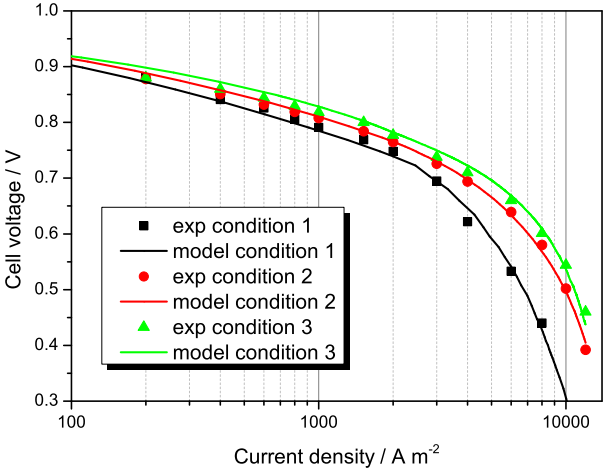

(b) Logarithmic current density scale.

Figure 6.8: Influence of relative humidity on the cell performance.

on page 52) and reduced oxygen transport resistance into the ionomer thin-films in the CLs (Equation (4.66) on page 67).

In Figure 6.9, the experimental and simulated polarization curves for test conditions **2** and **4** are depicted.

With increasing pressure, the cell performance is improved due to the higher oxygen concentration inside the cell. This effect is slightly overestimated by the model even though the ORR reaction rate is assumed to be proportional to $\sqrt{c_{\mathrm{Pt}}^{\mathrm{O_2}}}$ and not $c_{\mathrm{Pt}}^{\mathrm{O_2}}$ (Equation (4.60) on page 63).

The influence of the gas flow rates in the anode and cathode GCs is depicted in Figure 6.10. Here, test conditions **2** and **5** are compared.

Increasing the flow rates results in higher oxygen concentration in the cathode compartment of the cell which should increases the performance. However, stronger drying-out of the ionomer outweighs this effect and the overall cell performance is reduced.

It should be noted that all results shown in Figures 6.8, 6.9 and 6.10 have been obtained with a single set of parameters. The model is able to describe behavior of the fuel cell under varying operating conditions which underlines its predictive capabilities. In literature, seldom more than a single polarization curve is fitted for the purpose of validation. In comparison, the presented work put a large effort into the model validation.

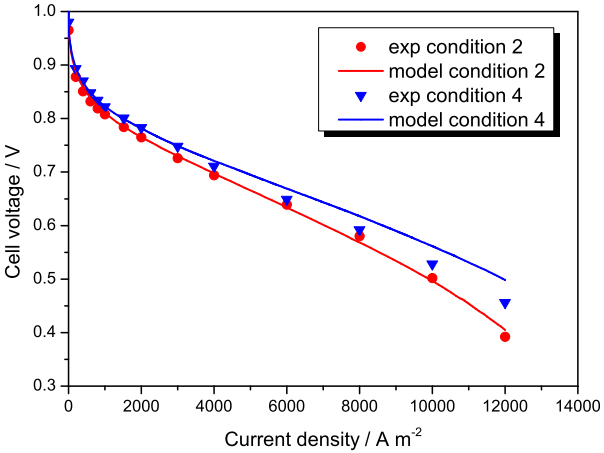

(a) Linear current density scale.

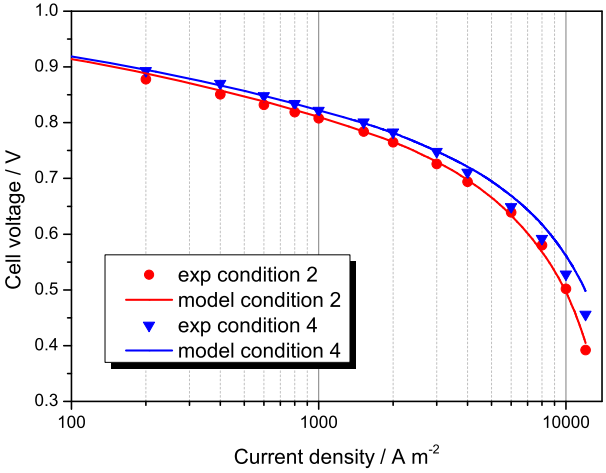

(b) Logarithmic current density scale.

Figure 6.9: Influence of pressure on the cell performance.

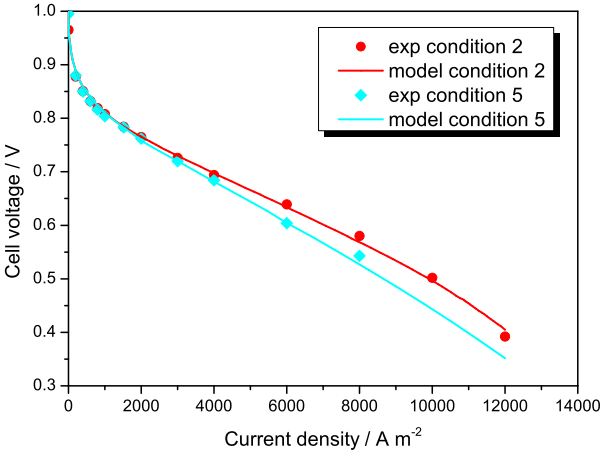

(a) Linear current density scale.

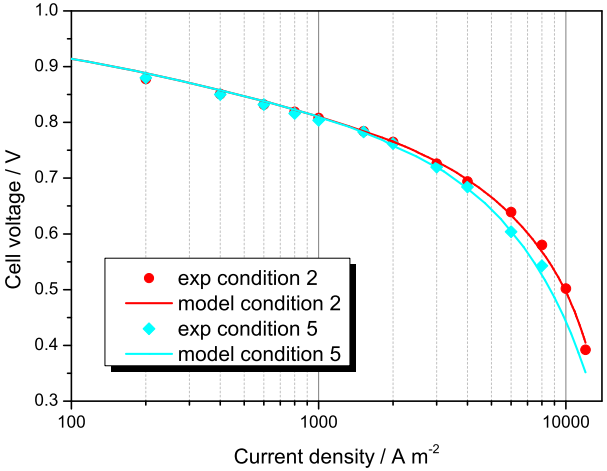

(b) Logarithmic current density scale.

Figure 6.10: Influence of the lambda control on the cell performance.

6.3 Electrochemical Impedance Spectroscopy

This section is divided into two parts. First, in Section 6.3.1, the features of the simulated impedance spectra will be analyzed. Then, a comparison between experimental measurements and simulations will be presented in Section 6.3.3

6.3.1 Process Identification

The analysis of impedance spectra of PEMFCs requires understanding of the underlying physical processes which determine the cell performance. The most common way to interpret experimental EIS is to fit an (often one-dimensional) equivalent circuit model to the experimental data [144, 145, 150, 196]. Though perfect agreement between experiment and simulation may be obtained with this approach, the elements of the equivalent circuits are missing a clearly defined physical meaning. Therefore, features of EIS are often misinterpreted.

With the physical fuel cell model, developed in this work, a more detailed analysis of the EIS is possible and the relevant mechanisms governing the fuel cell performance can be identified. In the following, an exemplary impedance spectrum will analyzed, where the identification of physical processes and their contribution to the overall EIS is obtained from systematic manipulation of the model equations.

The EIS that is investigated is simulated with the parameters presented in Table 6.3. The operating conditions are set according to condition **2** of Table 6.2 and the simulated cell current density is 6000 A m^2. The obtained *Bode*-plot of the imaginary part of the impedance for the base case, where all physical processes, which are incorporated into the model are operative, is depicted in Figure 6.11.

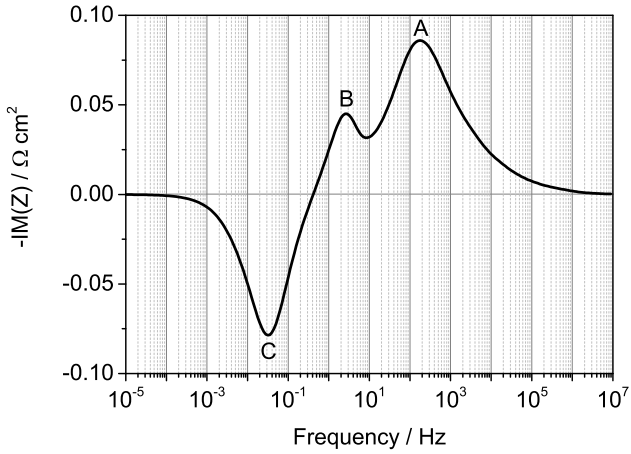

Figure 6.11: Base case for the analysis of the EIS.

Three main peaks can be observed: a capacitive peak at ∼1000 Hz (peak **A**), a second capacitive peak at ∼1 Hz (peak **B**) and an inductive peak below ∼0.1 Hz (peak **C**).

In literature, peak **A** is usually associated with the ORR and the HOR and peak **B** is attributed to diffusion processes inside the cell. The presence of the inductive peak **C** at low frequencies is often observed in literature [145], however, it is difficult to mea-

sure with conventional experimental equipment. Its presence bridges the gap between the experimentally observed slope of the polarization curve and the total cell resistance obtained from EIS measurements [145].

In the following, the contributions to these three peaks will be identified and discussed.

First, the influence of electrochemistry on the impedance will be investigated. To identify the contributions of the half-cell reactions, the storage terms of the ionic and electrical charge balances (Equation (4.37) on page 51) of the corresponding electrodes are set to zero. This is done separately for the ORR and the HOR.

Further, the influence of the platinum oxide formation on the cathodic platinum is determined by switching off the corresponding source- and sink terms and the reduction of the ECSA due to platinum oxides.

The *Bode*-plots, obtained with the manipulations discussed above, are presented in Figure 6.12 along with the base case where all mechanisms are operative.

The HOR manifests itself at high frequencies ($\sim 10^4$ Hz) and has a comparably small contribution to the impedance since the reaction is facile. Peak **A** mainly consists of the contribution of the ORR. Without it, two underlying peaks become visible: the HOR and the diffusion resistance which will be discussed in more detail below.

Without platinum oxide formation, peak **A** becomes smaller since the site blocker effect of the platinum oxides is eliminated and

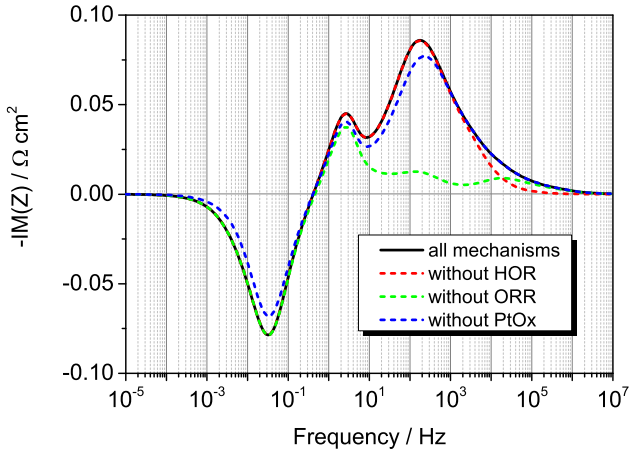

Figure 6.12: Influence of the electrochemistry on the simulated EIS.

the ORR becomes faster. Considering peak **C**, it may be observed that platinum oxide formation contributes to the inductive peak. This effect has been discussed in literature [145, 157, 167].

Next, the influence of the ionomer properties on the cell impedance will be analyzed. For this purpose, simulations with constant ionic conductivity of the PEM and CL ionomer and with a constant oxygen transport resistance R_{int} (Equation (4.66) on page 67) are carried out. The values which were used are listed in Table 6.4.

The comparison with the base case is depicted in Figure 6.13.

Since the considered dependence of $\sigma_{ion,CL}$ on the relative humidity is strong (Equation (4.41) on page 52), production of

Table 6.4: Ionomer properties, independent of the relative humidity, used for the EIS analysis.

Parameter	Value
$\sigma_{ion,PEM}$	5.4 / S m^{-1}
$\sigma_{ion,CL}$	0.1 / S m^{-1}
R_{int}	385.67 / s m^{-1}

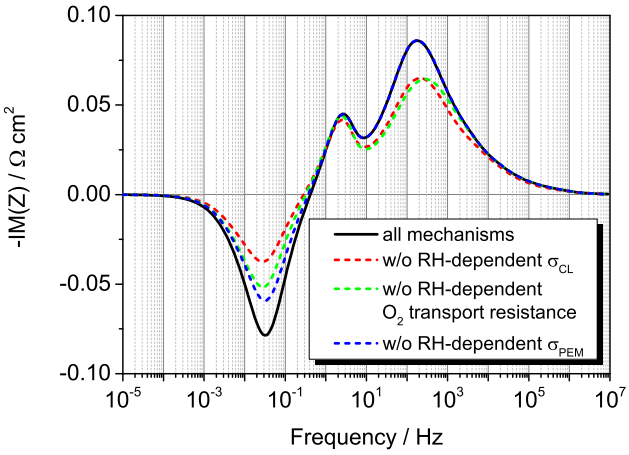

Figure 6.13: Influence of the ionomer properties on the simulated EIS.

water due to the tiny simulated current density step leads to a decrease of cell resistance. In the present analysis, this mechanism is the strongest contribution to the inductive peak **C** and manifests itself at low frequencies since the distribution of water inside the cell is slow. For $\sigma_{ion,PEM}$ and R_{int}, the effect is similar but less pronounced. With the estimated values for $\sigma_{ion,CL}$ and R_{int}, the rate of the ORR increases. Therefore, peak **A** is smaller in these simulations.

With the analysis above, the main mechanisms contributing to the peaks **A** and **C** have been identified. Next, source of peak **B** will be investigated. As stated above, this peak is usually attributed to transport resistance due to diffusion. Therefore, the influence of diffusion on the impedance was investigated. A simulation without the consideration of *Knudsen* diffusion and a simulation where the bulk diffusion coefficient were multiplied with a factor of 100 were carried out and compared to the base case (see Figure 6.14).

In both cases peak **A** becomes larger. This is due to the fact that the ionomer hydration is worse as the produced water can leave the CLs faster. Further, a frequency shift of peak **C** to higher frequencies is observed with increasing effective diffusion. A reduction of peak **B** is visible but the peak does not vanish.

Subsequently, the influence of concentration gradients along the channel is investigated. For this purpose, a simulation setup without the influence of the channel ("no channel") was used. For this purpose, the channel height is reduced to 2×10^{-6} m in order to eliminate the contribution of transport in gas channels. Further, along the channels, *Dirichlet* conditions are set.

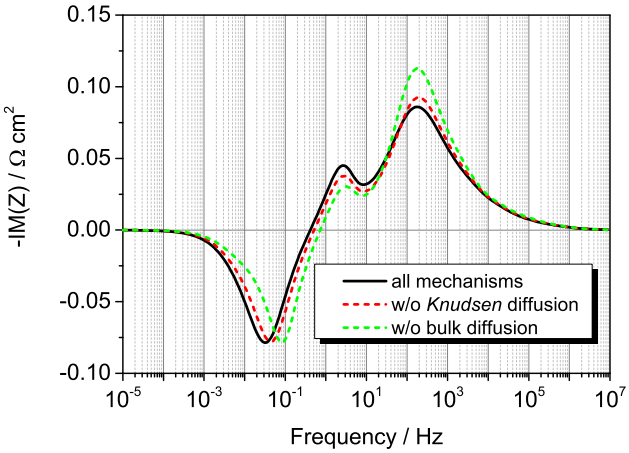

Figure 6.14: Influence of diffusion on the simulated EIS.

The pressure is set to the outlet pressure, phase saturation and composition are specified according to the inlet conditions. This results in a setup where species concentrations at the GC/GDL interfaces are constant along the channel and all transport is one-dimensional in the through-plane direction. The simulation in this setup is compared to the base case in Figure 6.15.

The comparison reveals, that peak **B** is mainly due to concentration gradients along the channel. Following the present analysis, the influence of diffusion on this peak is minor. Similar to the results of Figure 6.14, peak **A** becomes larger due to decreased hydration and a frequency shift in peak **C** is observed, revealing the inductive platinum oxide peak at 10^{-2} Hz and a shifted inductive ionomer peak at $\sim 3 \times 10^{-1}$ Hz.

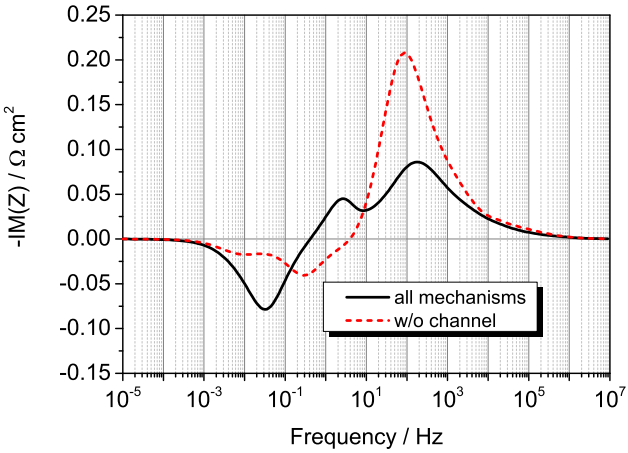

Figure 6.15: Influence of concentration gradients along the channel on the simulated EIS.

A minor contribution to the impedance is the temperature-dependence of $E^{0,\mathrm{ORR}}$ which causes a small capacitive peak since heat is produced in the cell due to the ORR.

To demonstrate that this analysis is complete, a simulation including all manipulations discussed above is compared to the base case in Figure 6.16.

In this case, no peaks are visible anymore. Figure 6.17 shows the *Bode*-plot in a different scale of the imaginary part.

The remaining peaks are below 0.2 mΩ cm^2 and are therefore insignificant.

To further analyze the transport processes in the anode and cathode compartment of the cell, simulations were carried out in

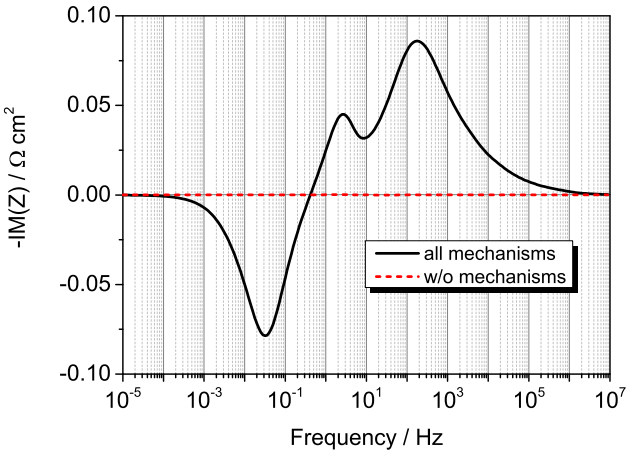

Figure 6.16: Comparison of EIS: base case and a simulation without all mechanisms considered in the model.

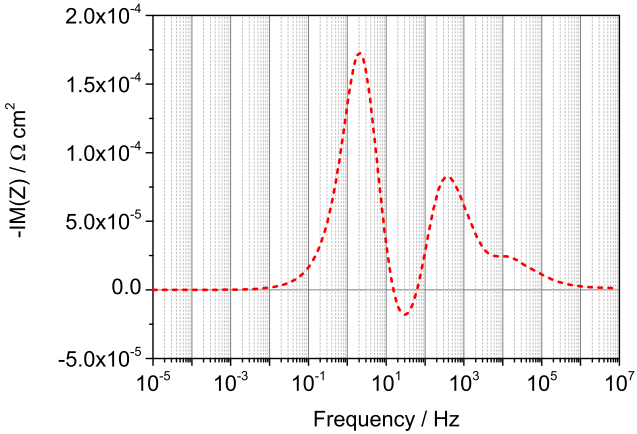

Figure 6.17: *Bode*-plot of a simulation without all mechanisms considered in the model.

the “no channel” setup. All manipulations discussed above were applied (no electrochemistry, PtOx-formation, constant ionomer properties, no *Knudsen* diffusion and $E^{0,\mathrm{ORR}}$ independent of T). The GDL thickness in one electrode is varied from 75-1200 μm and all porous layer thicknesses (GDL, MPL, CL) of the other electrode set to 10^{-6} m. For the sake of comparison, the ECSA was increased accordingly for the thin CLs to maintain the total active area. With this setup, the transport processes in each electrode can be revealed without the contribution of the other electrode.

Figure 6.18 shows the *Bode*-plots for different cathode GDL thicknesses.

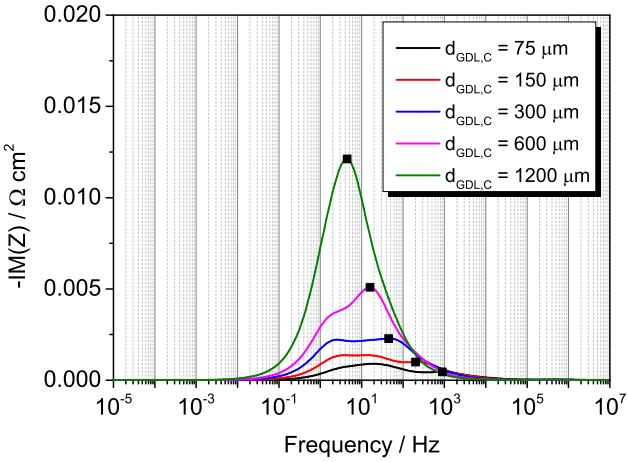

Figure 6.18: *Bode*-plot of simulations without all mechanisms but transport in the cathode for various GDL thicknesses.

Three peaks are visible: diffusion in the cathode at high frequencies and two peaks resulting from the anode which will be discussed later. The maximum of the cathode diffusion peak has been identified and the corresponding frequency is plotted over d_{GDL}^{-2} in Figure 6.19.

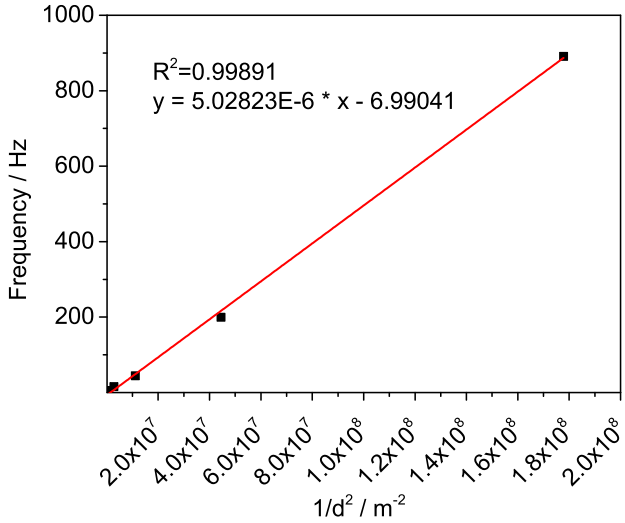

Figure 6.19: Cathodic diffusion peak frequency as a function of GDL thickness.

A linear relation is obtained which is typical for a diffusion process obeying the *Einstein-Smoluchowski*-relation [49, 171]

$$\upsilon = \frac{2D}{d^2}, \tag{6.1}$$

where $\upsilon = 1/t$ is the frequency and d the considered distance for diffusion. The *Bode*-plots for the anode side are depicted in Figure 6.20

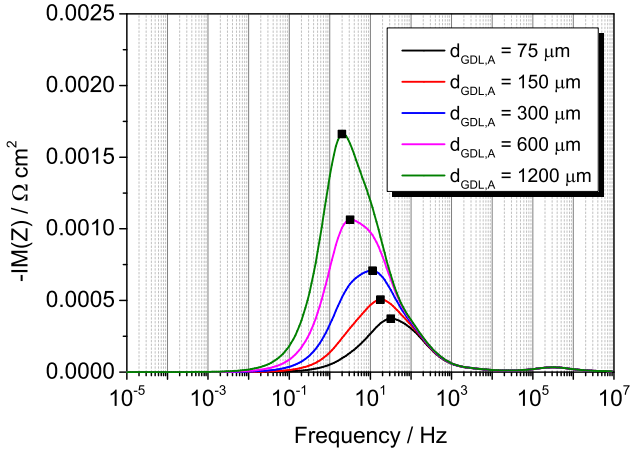

Figure 6.20: *Bode*-plot of simulations without all mechanisms but transport in the anode for various GDL thicknesses.

At $\sim 2 \times 10^5$ Hz, the diffusion in the cathode is visible which manifests itself at extremely high frequencies due to the short diffusion length in this simulation setup. For the anode side, two peaks which exhibit a certain offset in frequency are visible. Again, the maximum of the peak has been identified and is plotted, this time over $1/d_{GDL}$, in Figure 6.21.

Again, a linear relation is found which is expected for convective transport obeying Equation (4.26) on page 46.

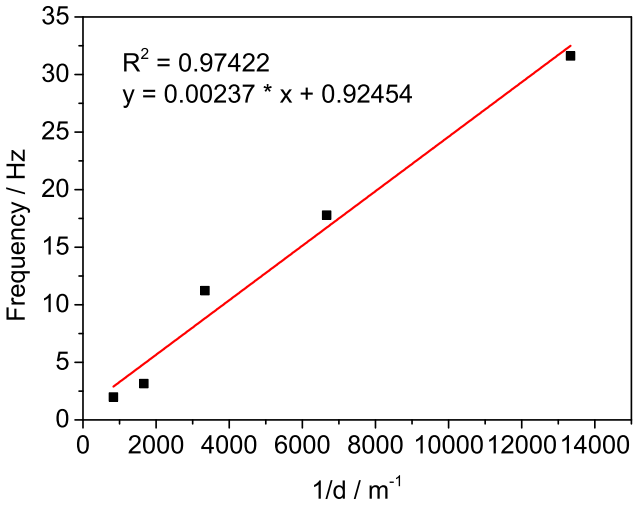

Figure 6.21: Anodic transport peak frequency as a function of GDL thickness.

From this analysis, it can be concluded that on the cathode side, diffusion is the dominant transport process and on the anode side convection prevails. Convective transport on the anode side is unexpected but the phenomenon will be explained in the following.

Comparing oxygen, water and hydrogen, the molecular weight of hydrogen is small. Therefore, the gas density does not change much when oxygen is converted into water via the ORR on the cathode side of a fuel cell. Consequently, convection is not operative. However, on the anode side, hydrogen is not converted but consumed. Further, each hydrogen molecule is split into two protons in the HOR. If an electroosmotic drag

coefficient $n_{drag} \geq 1$ is considered, each proton drags one or more water molecules with it across the membrane. This causes a pressure drop in the anode side towards the membrane resulting in convective transport.

To test this hypothesis, another simulation setup was designed. Again, the influence of the electrochemistry, ionomer and channel on the EIS was eliminated. In this setup, the simulated GDL thickness in the anode and cathode was 150 μm and the thickness of MPLs and CLs was 1 μm. To reduce convective through-plane transport in the anode, the coupling of the water fluxes across the membrane was eliminated. Consequently, no water is dragged from the anode to the cathode along with the protons. The resulting EIS is depicted in Figure 6.22 where it is compared to the corresponding EIS obtained with water transport across the membrane.

In the simulation without water flux through the PEM, the peak at 10 Hz is reduced to great extend. The remaining part is caused by convective transport due to hydrogen consumption via the HOR. The peak at $\sim 2 \times 10^2$ Hz, corresponding to the diffusion, remains almost unchanged. It can be concluded that, in the conditions simulated, convection must be operative in the anode and it is dominated by electroosmotic water transport.

6.3.2 Summary

- Inductive peaks, observed at low frequencies can be explained by

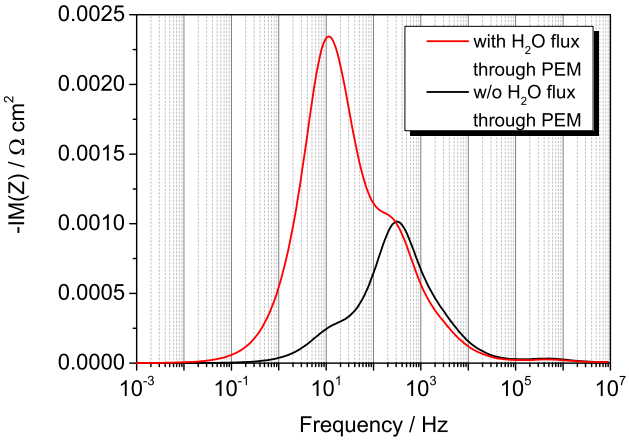

Figure 6.22: Influence of water transport across the PEM from anode to cathode.

1. Platinum oxide formation
2. Improved ionic conductivity with increasing relative humidity
3. Reduced oxygen transport resistance with increasing relative humidity

- Diffusion manifests itself as capacitive peak at $\sim 10^2$ Hz. The height of the peak, for a standard GDL of 150 μm thickness is in the range of 1 mΩ cm^2.
- The capacitive peak **B** at $\sim$ 1 Hz is not caused by diffusion but concentration gradients along the channel. In the solid oxide fuel cell (SOFC) modeling community, the effect

causing peak **B** is known as gas conversion impedance [86, 149].

- In the anode, convection is operative due to electroosmotic drag and hydrogen consumption.

6.3.3 Comparison of Model and Experiments

To further analyze the model, experimental and simulated impedance spectra are compared. EIS were recorded in conditions **1** and **2** (see Table 6.2). Figures 6.23 and 6.24 show the corresponding *Nyquist*-plots at current densities of 2000 and 6000 A m^{-2} respectively.

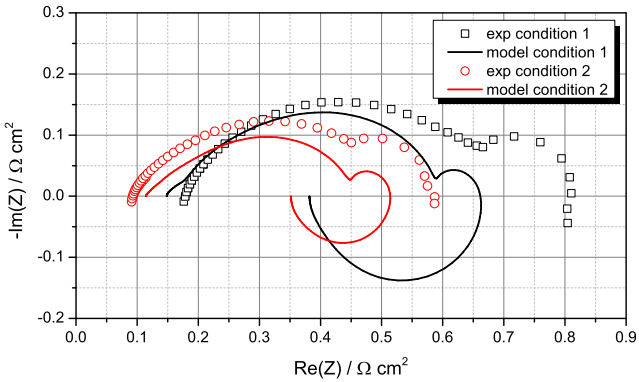

Figure 6.23: *Nyquist*-plot of the experimental and simulated impedance at 2000 A m^{-2}.

From these plots, the high frequency resistance of the cell can be obtained from the zero-crossing of the curves at low values of

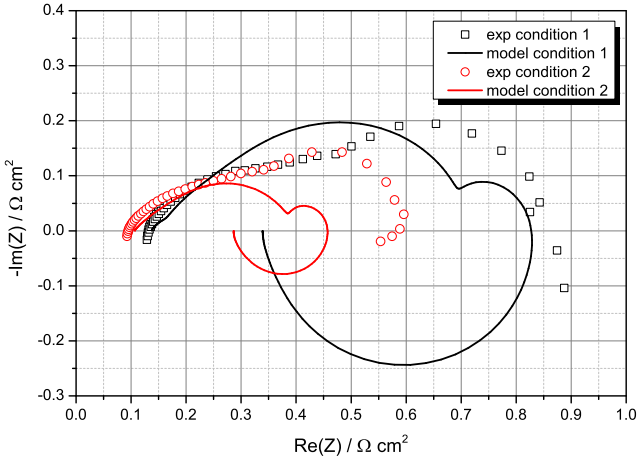

Figure 6.24: *Nyquist*-plot of the experimental and simulated impedance at 6000 A m^{-2}.

the real part $\mathrm{Re}(Z^*)$. In both *Nyquist*-plots, a higher resistance is observed for the dry condition **1**. The model is able to reproduced this trend. It can be explained by an increase in ionic conductivity of the PEM with increasing humidity.

At low frequencies, the total resistance of the cell is obtained. Theoretically, this value is equivalent to the slope of the polarization curve at the given current density. For the simulation and the experiments, this value differs significantly since, in the experiments, the inductive semi-circle cannot be resolved. It should be noted that for the model, the cell resistance from the EIS and polarization curve simulations match perfectly. Further, comparison between the experimental and simulated polarization curves (Figure 6.8 on page 125) shows that the slope of the polarization

curve is well captured by the model at the considered current densities. This is a strong indication that the inductive phenomena, discussed in Section 6.3.1, must be present in PEMFCs. For lower relative humidity, stronger inductive effects are predicted by the model.

Experimentally, two main capacitive “semi-circles” can be observed in Figures 6.23 and 6.24.

The left capacitive semi-circle which is mainly caused by the ORR is flattened which indicates a distribution of time constants for the corresponding reaction rate. This is caused by ionic potential gradients in the through-plane direction across the thickness of the CCL leading to local variations in the reaction overpotential. This finding is also predicted by the model (see Figure 6.6), which supports the proposed parameters listed in Table 6.3 for the calculation of the ionic conductivity (Equation (4.41) on page 52).

The right capacitive peak, which is underestimated by the model, can be explained by concentration gradients inside the cell (Section 6.3.1). A possible explanation for the deviation in this peak presents itself when the distribution of the cell current density, obtained from segmented cell measurements, is considered. Figures 6.25 and 6.26 show the experimental current density distribution in condition **1** at 6000 A m^{-2}. Additionally, the pathway of the gas channels through the single-serpentine flow field is sketched in Figure 6.25.

It can be observed, that the current density rises from the cell inlet in segment **A7** along the flow channel from the **A**- to the **F**-segments and then drops in segments of domain **G** towards

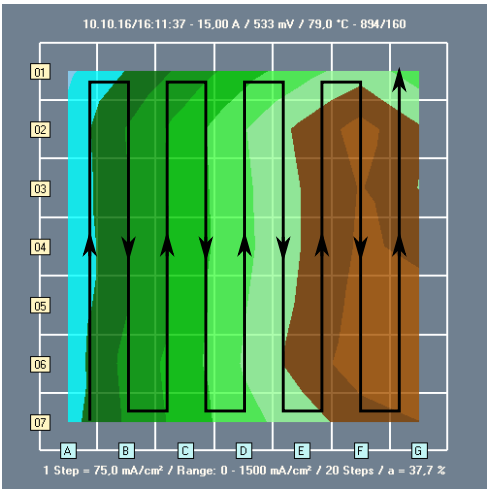

Figure 6.25: 2D plot of the experimental current density distribution in condition **1** at 6000 A m^{-2} with a sketch of the flow channel pathway through the bipolar plate. Note: The real flow field exhibits 24 bends along the channel.

the outlet of the cell. This can be explained by increasing humidification along the channel due to the water production of the ORR and flooding effects close to the outlet.

However, in the boundary segments **A1**-**G1** and **A7**-**G7** a drop in current density is observed. The cause for this drop in performance close to the boundary is, so far, unknown and the model is unable to resolve this effect due to its simplified two-dimensional geometry. The effect of a periodic performance loss along the flow channel can explain the observed deviations between experimental and simulated impedance spectra.

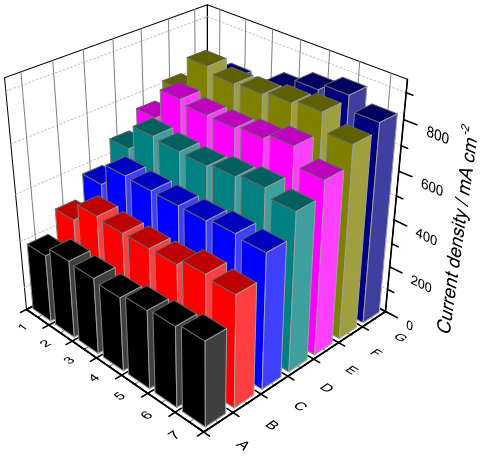

Figure 6.26: 3D plot of the experimental current density distribution in condition **1** at 6000 A m^{-2}.

In Figures 6.27 and 6.28, the *Bode*-plots corresponding to Figures 6.23 and 6.24 are depicted.

At a current density of 2000 A m^{-2}, the experimentally measured trends are qualitatively captured by the model. The high frequency peak due to the half-cell reactions is larger for the dry condition **1** than for condition **2**. This results from improved ionomer properties in the humid condition. The capacitive peak due to concentration gradients is similar for both conditions which is well captured by the model. The experiments indicate the existence of an inductive peak at low frequencies which becomes larger for dry conditions. Again this trend is well captured by the model.

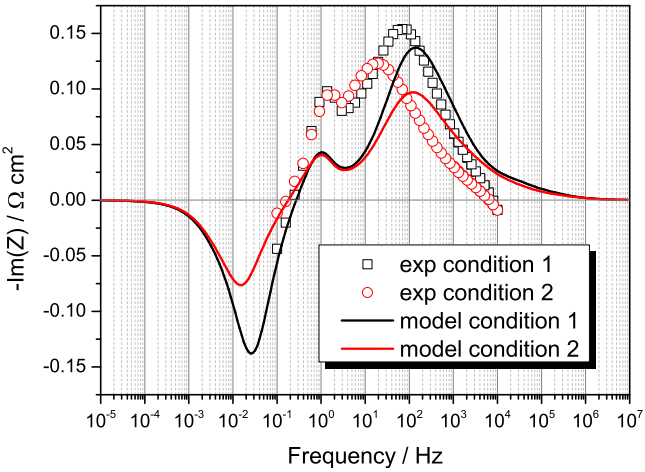

Figure 6.27: *Bode*-plot of the experimental and simulated impedance at 2000 A m^{-2}.

At 6000 A m^{-2}, the agreement between experiment and simulation is not satisfactorily. In the experimentally measured EIS, the loss due to concentration gradients in the cell is dominating over the electrochemically induced losses. This is vice versa for the model results.

From this analysis it can be concluded that a three dimensional model, able to describe the boundary effects in the cell, is necessary in order to match the simulated and experimentally measured impedance spectra. In the present model, losses due to the ORR may be overestimated, especially at elevated current density while transport losses are underestimated.

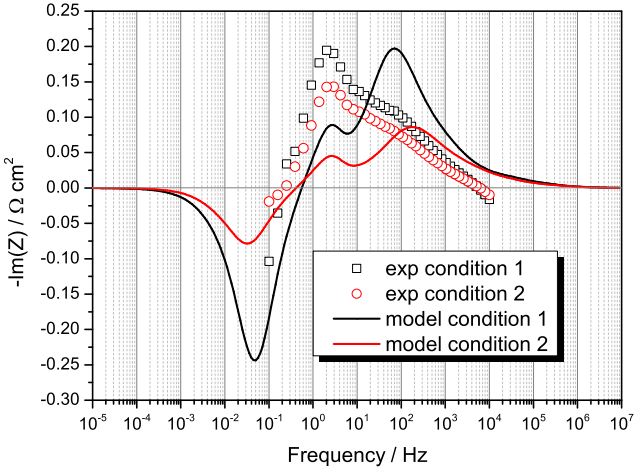

Figure 6.28: *Bode*-plot of the experimental and simulated impedance at 6000 A m^{-2}.

7 Chemical Membrane Degradation

> There are no safe paths in this part of the world. Remember you are over the Edge of the Wild now, and in for all sorts of fun wherever you go.
>
> *(J.R.R. Tolkien, The Hobbit)*

In this chapter, the model for the simulation of chemical membrane degradation will be presented. It is based upon the performance model presented in the Chapters 4 and 5 and extends its capabilities to describe the formation and transport of hydrogenperoxide (Section 7.2), the transport and redox reactions of iron impurities in the CLs and PEM (Section 7.3), formation of radical species (Section 7.4) and the subsequent attack on the polymer (Section 7.5). The corresponding initial, boundary- and coupling conditions will be presented in Section 7.6.

Before the discussion of these phenomena, a review on models describing chemical membrane degradation will be given in

Section 7.1. Sections on thermal and mechanical membrane degradation, written by the author, can be found in [87].

7.1 Review of Chemical Degradation Models

The following review of chemical membrane degradation models is a revised version of the author's contribution to a recent review paper on PEMFC modeling and degradation [87].

Chemical degradation covers the effects of membrane decomposition due to (electro-) chemical reactions and membrane contamination.

It is common agreement that, during fuel cell operation, the production of hydrogen peroxide H_2O_2 and subsequent decomposition to radical species is the main cause for chemical membrane degradation [31, 65, 66, 168]. However, reports on the location of membrane degradation are contradictory: Degradation was observed at the anode [110, 132] or at the cathode [99, 199]. Also the role of a platinum band, which may form during operation due to catalyst degradation, is still under discussion. In [133] and [154] higher degradation is attributed to the presence of a Pt band while in [114] the contrary is reported. Subsequent investigations found that membrane degradation decreases with increasing Pt particle density in the membrane [77, 78, 153].

It is proposed that H_2O_2 is formed at the electrolyte electrode interfaces by reaction of cross-over gases on the Pt-particles

[110, 166]. According to [65], H_2O_2 has a diffusion length in the millimeter range. Therefore, the location of H_2O_2-formation and membrane degradation are not necessarily coupled. H_2O_2 may form at the anode with O_2 crossing the membrane or as a side product of the ORR on the cathode side. Both ways of H_2O_2-formation are discussed in [168] but it is stated that the predominant mechanisms remain unclear.

When H_2O_2 is decomposed, $HO^\bullet$ and $HOO^\bullet$ radicals are formed which in turn attack the electrolyte material. Inside the membrane, this decomposition is catalyzed by metallic impurities [67] or Pt-particles from the catalyst layers [24].

For the attack on the polymer structure, several sites have been proposed. Some of the polymer backbones terminate in H-containing end groups which have been identified to be a weak spot and a mechanism for the attack on these sites has been proposed [41]. This mechanism causes an advanced unzipping of the backbone accompanied by the release of HF and CO_2. When such unzipping reaches a junction of the backbone and a side chain including sulfonic acid sites, the whole side chain is "cut off" and forms the so-called "molecule A" which can be found as a degradation product in the effluent water of the cell [75]. This loss of sulfonic acid sites leads to a reduction in membrane conductivity. Fluorination of the weak end groups resulted in greatly reduced fluoride emission rate (FER), and therefore enhanced chemical stability [41].

Also, the scission of polymer side-chains has been proposed as a degradation pathway [197]. This cutting of the side chain causes further degradation via unzipping until a junction of side

chain and backbone is reached. Then, two weak end groups on the backbone are produced leading to an irreversible increase in weak sites and therefore accelerated chemical degradation. In [30], it was proposed that at high humidity degradation is governed by the unzipping mechanism and under low humidity conditions scission of the side chains dominates. The exact location for radical attack on the side chain is under debate. Sulfonic acid sites as well as ether linkages have been proposed [30, 50, 84, 85].

For the modeling of chemical membrane degradation, two types of models have been developed. To gain insight in the basic mechanisms of degradation and to interpret experimental results, kinetic zero-dimensional models are applied [30, 31, 65, 197]. Further, one-dimensional models for chemical degradation of the membrane were embedded in a simulated fuel cell environment [66, 168].

7.1.1 Zero-dimensional Models

A kinetic model to determine the contribution of backbone unzipping and side chain cleavage to the overall chemical degradation process in various degradation environments was developed by Xie and Hayden [197]. A relationship for the fluorine fractional loss, the concentration of carboxylic acid in the membrane and the ratio of rate constants for side chain cleavage and unzipping were derived. Correlation of infrared spectroscopy measurements to this kinetic model gives the basis to determine the rate constants ratio under different experimental conditions. This

model allows for the prediction of the influence of the polymer structure on the degradation mechanisms, therefore giving guidance for improved chemical durability through meaningful molecular design.

Chen and Fuller conducted durability tests at different temperatures and degradation was studied at anode, cathode and in the center of the membrane using X-ray photoelectron spectroscopy (XPS) and HF/TFA ratio analysis [31]. Degradation was accelerated at higher temperatures and was found to be more severe on the anode side. Decomposition of the polymer backbone and side chains was also reported. Degradation in the bulk of the membrane was observed to be slow and mainly due to backbone decomposition. This was attributed to attack of molecular oxygen on carbon centered radical end group on the main polymer chain at low temperatures. To investigate the influence of the different mechanisms and explain the experimental results, a kinetic model was developed. In this model, four steps of membrane degradation are proposed: (1) radical formation via *Fenton's* reaction, (2) reaction of O_2 with carbon centered radicals located on the backbones and backbone unzipping due to $HO^{\bullet}$ attack, (3) termination of unzipping by reaction of two carbon centered radicals which again form a stable backbone structure and (4) side group degradation.

Assuming steady state, an expression for HF-formation is formulated allowing for a qualitative explanation of the experimental results. Based on this expression, a rate expression for fluorine loss is derived taking into account the contributions of *Fenton's*- and side group degradation reaction. The authors concluded that degradation accelerates with higher temperature, and that

it is more severe at the anode due to higher H_2O_2 and radical concentrations. In the bulk membrane, they observed that backbone decomposition outweighs degradation via the side chains and they found that O_2 attack on long chain radicals contributes to the membrane degradation.

In the following, the kinetic model of Gubler et al. [65] will be compared to the one of Ghelichi et al. [64]. Both aim to determine the chemical degradation resulting from H_2O_2 decomposition via *Fenton's* chemistry and subsequent radical attack on the polymer. Both start from a similar set of chemical reactions. While Gubler et al. use rate constants valid for room temperature only, Ghelichi et al. also give the activation energies enabling their model to determine degradation at fuel cell operating conditions.

After comparison of the different reaction rates, Ghelichi et al. discard the reaction of Fe^{2+} with $HO^\bullet$ because the $HO^\bullet$ concentration is low and the direct formation of $HO^\bullet$ from H_2O_2 because the reaction is negligibly slow. Gubler et al. consider reactions involving H_2 and O_2 which are present in the membrane due to gas cross over. Comparison of the reaction rates shows that these reactions are kinetically relevant and cannot be neglected as was done in [64]. Therefore, the results of Ghelichi et al. are only valid for ex situ *Fenton's* tests and not for in situ fuel cell operation.

Assuming constant Fe and H_2O_2 concentrations, Ghelichi et al. derive an analytic solution for the calculation of the $HO^\bullet$ radical concentration enabling direct calculation of the FER without the need to consider the $HOO^\bullet$ radicals in the system explicitly. One

flaw of this analytic solution is that the attack of the radicals on the polymer does not influence the steady state concentration of $HO^{\bullet}$. In [65] Gubler et al. show that radical attack on the polymer reduces the $HO^{\bullet}$ steady state concentration up to two orders of magnitude, depending on the iron content, which suggests that the model of Ghelichi et al. overestimates the $HO^{\bullet}$ concentration.

The model of Gubler et al. neglects radical attack on the side chains while the Ghelichi model incorporates the mechanism with the coarse-grained consideration of the polymer structure. Thus, even though both models give valuable insights into the mechanisms of chemical degradation, due to the assumptions and simplifications mentioned above, the models cannot be applied to predict membrane degradation under fuel cell operating conditions.

7.1.2 One-dimensional Models

Concerning the 1D models, Kundu et al. investigated degradation of a Gore™ PRIMERA® series 5510 catalyst coated membrane [99]. To increase mechanical stability, the membrane contains a layer which is reinforced with expanded polytetrafluoroethylene (ePTFE). The membrane electrode assembly (MEA) was tested under OCV conditions. Application of scanning electron microscopy (SEM) revealed membrane degradation at the cathode and a platinum band in the membrane was observed.

A semi-mechanistic 1D transient model was developed and compared to the experimental investigation of FER, crossover cur-

rent and OCV. In this model, degradation is assumed to start at the cathode and to advance in a wavelike manner to the anode causing thinning of the membrane. Crossover current, H_2O_2-formation, subsequent radical formation and membrane degradation is proposed to depend on the flux of H_2 from anode to cathode. The H_2O_2 formation from oxygen cross over is neglected in this model. The loss of electrochemical active surface area is incorporated and equations are solved using the "method of lines".

Cumulative fluoride release of anode and cathode, crossover current and the evolution of OCV are simulated. It is concluded that all fluoride emissions result from ionomer degradation next to the cathode. Further, degradation is assumed to advance to the reinforcement layer. When the degradation front reaches the ePTFE layer, the fluoride generation slows down as the reinforcement is assumed inert. The lower anode FER is attributed to the larger diffusion resistance when fluoride is generated at the cathode and needs to cross the membrane.

Another 1D fuel cell model incorporating chemical degradation of the membrane was presented by Shah, Ralph and Walsh [168]. It is based on the solution of conservation equations for mass, charge and energy including a detailed description of the transport phenomena in different layers of the fuel cell. A sub-model describes H_2O_2 formation, evolution of radicals from *Fenton's* reaction and direct formation at the anode. Chemical degradation is assumed to proceed via unzipping of the backbone, side chain cleavage and decomposition of "molecule A".

Model results are concentration profiles of the considered species and their evolution with time. These results suggest that degradation propagates from the anode to the cathode. Therefore, it is concluded that FER measurements alone are not sufficient to determine the main location for degradation as the process is time-dependent, localized and diffusion effectively distributes HF in the membrane.

The influence of oxygen concentration at OCV, membrane thickness, load operation, temperature, water activity and reaction rate constants was investigated.

A third 1D continuum model was developed by Gummalla et al. [66] where the model domain consists of the membrane and the electrodes. Diffusive transport and reaction of crossover gases, radical formation and attack on the membrane with subsequent HF release under OCV conditions is incorporated into the model.

The resulting reaction diffusion equations are solved using a central finite difference scheme and a nonlinear solver implemented in software package gPROMS [5].

Radicals can be formed and quenched at Pt-particles which are assumed to be uniformly distributed inside the membrane. This assumption is due to an earlier study [115] where, in contrast to other experiments, no platinum band was observed, but a homogeneous distribution of Pt-particles was found in the membrane.

A general reaction of hydroxyl radicals with Nafion® is incorporated but no specific degradation mechanism is assumed. The

model results are fitted to the measured FER data from the OCV-tests conducted in [115]. Hydroxyl radicals are assumed to be produced directly by partial oxygen reduction on the Pt particles in the membrane. Influence of the Pt-particle size and the spacing between them, concentration of oxygen at the cathode, relative humidity and membrane thickness on the degradation rate was simulated.

It is found that the FER strongly depends on the particle size as the quenching of produced radicals is more likely on bigger particles. The spacing between particles determines whether radical formation is controlled by diffusion or the reaction kinetics. For small distances between particles, radical generation takes place in a narrow region where H_2 and O_2 are almost completely consumed while for larger spacing, H_2 and O_2 concentrations are higher throughout the membrane and radical production takes place in the whole membrane. Variations of the relative humidity influence degradation is three ways: (1) decreasing RH increases the oxygen molar fraction in the supply gases, (2) decreasing RH decreases the gas permeability and (3) higher membrane hydration influences the hydration shell of the Pt-particles, reducing the available surface area for radical generation. This leads to an increase in degradation up to a RH of approximately 20-40%, for higher RH, the FER decreases again.

The first model to incorporate the effect of chemical degradation on the macroscopic properties of the membrane was developed by Coulon et al. [39, 40]. In [40], an elementary kinetic model is presented simulating H_2O_2 formation at the anode, $HO^{\bullet}$ formation via *Fenton's* reaction and radical attack which leads to side chain cleavage and loss of sulfonic acid sites. It couples a new

model for the membrane to the multi-scale electrode models [57, 58] of MEMEPhys® [56, 72]. For the membrane, the conductivity model presented in [34] is extended resulting in an equation for the conductivity depending on chemical degradation.

For the first time, a feedback between chemical degradation and the transport properties of the membrane is established. It was concluded that membrane degradation has a pronounced effect on the fuel cell performance above 1000 h of operation. Cell current and membrane thickness have only minor influence on the increase in specific membrane resistance.

Recently, Wong and Kjeang developed a model for simulation of in-situ chemical degradation [194] They consider H_2O_2 formation via two-electron-transfer at the anode and radical formation from a single *Fenton's* reaction of H_2O_2 with Fe^{2+}.

The radical attack on the polymer structure starts at the side chains with attack on the ether bond of the αOCF2 group. Unzipping along the side chain leads to an intermediate oxygen centered radical and further degradation results in main chain scission with the formation of two carboxylic acid groups on the polymer backbone. From there, the degradation proceeds via unzipping along the backbone.

This degradation model is incorporated into a 1D, single phase transport model in the GDLs, MPLs and CLs of the cell with electron transport through the solid phase. In the catalyst layers and the membrane, an equation is solved for the electrolyte potential and transport of water, H_2O_2, H_2 and O_2 is simulated and additional transport of degradation products and hydroxyl radicals is modeled in the membrane.

Evolution of the polymer structure, dry membrane thickness, evolution of the membrane ionic resistance and cell open circuit voltage are simulated and the model is validated against experimental results [108].

In a following work [195], the model is expanded to incorporate the transport of Fe^{2+} and Fe^{3+} in the catalyst layers and the membrane and the redox cycle of these ions. Radical formation strongly depends on the presence of H_2O_2 and Fe^{2+}. The total iron ion concentration in this model is kept constant and the electrochemical reduction of Fe^{3+} to Fe^{2+} is incorporated in the catalyst layers. This reaction, as well as H_2O_2-formation is strongly dependent on the electrode potentials. Therefore, cell operation at three different voltages is simulated: OCV, 0.9 V and 0.7 V.

At OCV, the concentrations of H_2O_2 and Fe^{2+} are high at the anode side causing severe degradation. At 0.9 V, the H_2O_2 concentration remains almost the same, while the degradation rate is found to be reduced by 57%. This reduction is caused by the lower Fe^{2+} concentration at 0.9 V which demonstrates the high impact of the state of iron on the degradation rates.

At 0.7 V, the ionomer potential gradient increases resulting in an almost zero net flux of Fe^{3+} to the anode which reduces the Fe^{2+} formation there. Iron ions accumulate at the cathode resulting in degradation at the cathode side under higher load conditions. Overall, the degradation at 0.7 V is reduced to one tenth.

7.2 Hydrogen Peroxide

7.2.1 Formation

In this work, the approach of [195] is applied and incorporated into the two-dimensional cell model. Hydrogen peroxide is formed via a side reaction of the ORR, the two electron transfer:

$$\mathrm{O_2} + 2\,\mathrm{H^+} + 2\,\mathrm{e^-} \rightleftharpoons \mathrm{H_2O_2}. \tag{7.1}$$

The equilibrium voltage $E^{0,\mathrm{H_2O_2},f}$ for this reaction is equal to 0.695 V [195]. The corresponding reaction rates in the anode and cathode catalyst layer are determined using

$$r^{\mathrm{H_2O_2},f} = ECSA_{eff}\; i^{0,\mathrm{H_2O_2},f} \frac{c^{\mathrm{O_2}}}{c^{\mathrm{O_2}}_{ref}} \chi \exp\left(-\frac{\mathrm{F}\eta^{\mathrm{H_2O_2},f}}{\mathrm{R}T}\right), \tag{7.2}$$

where χ denotes the selectivity of hydrogen peroxide formation [166] which is defined as

$$\chi = \left[\frac{1980 + 32.4\lambda^{\mathrm{H_2O}}}{1167.4EW\,(1 + 0.0648\lambda^{\mathrm{H_2O}})}\right]^2 \quad / \quad -. \tag{7.3}$$

Additionally, the reduction of hydrogen peroxide at the catalyst surface via the following reaction is modeled.

$$\mathrm{H_2O_2} + 2\,\mathrm{H^+} + 2\,\mathrm{e^-} \rightleftharpoons 2\,\mathrm{H_2O} \tag{7.4}$$

For the hydrogen peroxide reduction, $E^{0,\mathrm{H_2O_2},r} = 1.76$ V [195]. The reaction rate is described using

$$r^{\mathrm{H_2O_2},r} = 2\ ECSA\ i^{0,\mathrm{H_2O_2},r} \frac{c^{\mathrm{H_2O_2}}}{c_{ref}^{\mathrm{H_2O_2}}} \sinh\left(\frac{\alpha^{\mathrm{H_2O_2},r}\mathrm{F}\eta^{\mathrm{H_2O_2},r}}{\mathrm{R}T}\right). \tag{7.5}$$

From the volumetric current densities (Equations (7.2) and (7.5)) the source and sink terms for the mass balance equations are determined using Equation (4.74) on page 70. The heat production due to these reactions is neglected.

7.2.2 Transport

In the porous electrodes, the transport of hydrogen peroxide is described using equation Equation (4.4) on page 35 where the storage and flux terms are calculated via Equation (4.24) on page 46 and Equation (4.25) on page 46 respectively. In the considered two-phase system, hydrogen peroxide has a high affinity for the liquid water phase which manifests itself in high values for the *Henry* coefficient [159]. It ranges from 6.81×10^2 to 1.382×10^3 mol m^{-3} Pa^{-1} which is about seven to eight orders of magnitude higher as e.g. the value for oxygen ($\sim 1.283 \times 10^{-5}$ mol m^{-3} Pa^{-1}). To describe the the equilibrium between hydrogen peroxide in the gas and liquid phase, the relations

of [117] were implemented into the model describing the non-ideal behavior of the system. For the equilibrium concentration in the polymer phase, the same value as for the liquid phase is used. The mole fraction of hydrogen peroxide in the liquid and ionomer phase is calculated via

$$x_{l/ionomer}^{\mathrm{H_2O_2}} = \frac{x_g^{\mathrm{H_2O_2}} p_g}{p_{sat}^{\mathrm{H_2O_2}} a_l^{\mathrm{H_2O_2}}}, \tag{7.6}$$

where the vapor pressure of hydrogen peroxide is

$$p_{sat}^{\mathrm{H_2O_2}} = 10^X 1.3332237 \times 10^2 \quad / \quad \mathrm{Pa} \tag{7.7}$$

with the exponent (without units)

$$X = \begin{cases} \textbf{if } 273.15 \leq T < 368.15: \\ 24.8436 - 3511.54/T - 4.61453 \log(T) \\ -3.60245 \times 10^{-3} T - 7.73423 \times 10^{-6} T^2 \\ +1.78355 \times 10^{-8} T^3 - 2.27008 \times 10^{-13} T^4 \\ \\ \textbf{if } 368.15 \leq T < 433.15: \\ 38.8572 - 3627.72/T - 11.2133 \log(T) \\ +4.74132 \times 10^{-3} T \end{cases} \tag{7.8}$$

and the hydrogen peroxide activity is calculated from the temperature-dependent *Redlich-Kister* parameters B_{0-3} / J mol^{-1} [117]

$$
\begin{aligned}
a_l^{\mathrm{H_2O_2}} = \exp\Big\{ \left(x_l^{\mathrm{H_2O}}\right)^2 / \, \mathrm{R}T \\
\times \Big[B_0 + B_1 \left(3 - 4x_l^{\mathrm{H_2O}}\right) \\
+ B_2 \left(1 - 2x_l^{\mathrm{H_2O}}\right)\left(5 - 6x_l^{\mathrm{H_2O}}\right) \\
+ B_3 \left(1 - 2x_l^{\mathrm{H_2O}}\right)^2 \left(7 - 8x_l^{\mathrm{H_2O}}\right) \Big] \Big\}.
\end{aligned}
\tag{7.9}
$$

In the polymer phase the transport of hydrogen peroxide is modeled using *Fick's* law. The balance equation is then

$$
\frac{\partial c^{\mathrm{H_2O_2}} \phi_{ion}}{\partial t} + \nabla \cdot \left(-D_{eff}^{\mathrm{H_2O_2}} \nabla c^{\mathrm{H_2O_2}} \right) - q^{\mathrm{H_2O_2}} = 0, \tag{7.10}
$$

where $D_{eff}^{\mathrm{H_2O_2}} = 6.8 \times 10^{-11}$ / m^2 s^{-1} [143],

$$
c^{\mathrm{H_2O_2}} = \frac{x_l^{\mathrm{H_2O_2}} \rho_l^{\mathrm{H_2O}}}{M^{\mathrm{H_2O}}} \tag{7.11}
$$

and $q^{\mathrm{H_2O_2}}$ is calculated based on the system of reactions presented in Section 7.4.

7.3 Iron Impurities

Two explanations for the presence of iron in the fuel cell are given in the literature: contamination during the manufacturing process [41] and transport of iron from the piping or bipolar plates [148]. Therefore, earlier models considered a constant

concentration [168, 194] or a continuous source [39] of iron ions which react with hydrogen peroxide to form radicals.

A constant iron ion concentration seems unreasonable as Fe^{2+} is converted into Fe^{3+} in the main radical formation reaction, therefore, degradation would soon cease. A continuous source is also questionable, at least when iron-free bipolar plates are employed in the cell.

In this work, an initial concentration due to the manufacturing process is assumed. Additionally, the regeneration of Fe^{2+} via electro-chemical reactions in the catalyst layers is considered.

7.3.1 Redox-Reactions

Ferrous ions (Fe^{2+}) are *Fenton's* active meaning that they react with hydrogen peroxide to form highly active hydroxyl radicals ($OH^{\bullet}$). The reaction of ferric ions (Fe^{3+}) with hydrogen peroxide will yield hydroperoxyl radicals ($HOO^{\bullet}$) which are by far less reactive [37, 38, 65]. Therefore, the redox reaction of ferrous and ferric ions,

$$\mathrm{Fe^{3+} + e^{-} \rightleftharpoons Fe^{2+}} \tag{7.12}$$

has to be considered where the temperature-dependent equilibrium voltage is [191, 195]

$$E^{0,\mathrm{Fe}} = -1.23 \times 10^{-2} + 4.147 \times 10^{-3} T - 5.111 \times 10^{-6} T^2 + \frac{\mathrm{R}T}{\mathrm{F}} \ln\left(\frac{c^{\mathrm{Fe}^{3+}}}{c^{\mathrm{Fe}^{2+}}}\right). \tag{7.13}$$

In the present model this reaction is incorporated in the anode and cathode catalyst layers and the corresponding expression for the reaction rate is [195]

$$r^{\mathrm{Fe}} = ECSA\ k^{\mathrm{Fe}}\ \mathrm{F}\sqrt{c^{\mathrm{Fe}^{2+}} c^{\mathrm{Fe}^{3+}}} \times \left[\exp\left(\frac{\alpha \mathrm{F}\eta^{\mathrm{Fe}}}{\mathrm{R}T}\right) - \exp\left(\frac{-\alpha \mathrm{F}\eta^{\mathrm{Fe}}}{\mathrm{R}T}\right)\right]. \tag{7.14}$$

The value of k^{Fe} was estimated to be 10^{-5} m s^{-1} and $\alpha = 0.5$. For this reaction the contribution to the heat production in the catalyst layers is neglected.

7.3.2 Transport

The flux of iron species i in the CLs and PEM is described using a *Nernst-Planck* type equation [195]:

$$\Psi^i = -D^i \nabla c^i - u^i z^i c^i \mathrm{F} \nabla \Phi_{ion}. \tag{7.15}$$

Here, D^i is the ionic diffusion permeability, u^i the ion mobility and z^i the charge number. The ionic diffusion permeability is

related to the mobility via a generalized *Nernst-Einstein* type relation:

$$D^i = f^i u^i \mathrm{R} T, \tag{7.16}$$

where f^i is a factor describing the deviation from the *Nernst-Einstein* relation. It reflects the fact that the interaction between electro-osmotic flow and the counter-ions is stronger than for co-ions whose concentration is small [10]. Therefore, the ionic diffusion permeability is reduced and $f^i < 1$. In [10], a value of 0.36 was found for Na^+. This factor has a strong influence on the voltage dependence of the chemical membrane degradation as it shifts the ration between diffusion and transport due to potential gradients and therefore alters the iron ion distribution inside the CLs and PEM. In this work, to fit the experiments, a value of 0.33 for both, ferrous and ferric ions was used.

For the mobilities u^i of ferrous and ferric ions, values of 1.25×10^{-13} / mol s kg^{-1} and 1.83×10^{-14} / mol s kg^{-1} are used respectively [195].

The charge balance equation of contaminant species i is

$$\frac{\partial \phi_{ion} c^i}{\partial t} + \nabla \cdot \left(-f^i u^i \mathrm{R} T \nabla c^i - u^i z^i c^i \mathrm{F} \nabla \Phi_{ion} \right) - q^i = 0. \tag{7.17}$$

In the electrodes, q^i is equal to Equation (7.14). In the PEM domain, q^i is calculated as the sum of the species sources and sinks

due to the reactions listed in Table 7.1 where each source/sink term is calculated with Equation (7.19).

The interactions between the iron ions and the polymer are assumed to be strong so that the ions are unable to leave the CLs. Therefore, *Neumann* no-flow boundary conditions are applied on the CL/MPL interfaces.

7.4 Radical Formation

With hydrogen peroxide and ferrous ions present in the membrane, radical formation due to *Fentons's* chemistry is modeled. The reactions considered along with the corresponding rate constants at reference temperature (298.15 K) k^i_{ref} and activation energies E^i_{act} are listed in Table 7.1.

Table 7.1: Set of chemical reactions considered in the model.

Nr.	Reaction	k^i_{ref} / m^3 mol^{-1} s^{-1}	E^i_{act} / J mol^{-1}	Ref.
1	$Fe^{2+} + H_2O_2 + H^+ \longrightarrow Fe^{3+} + HO^\bullet + H_2O$	6.5×10^{-2}	3.54×10^4	[151]
2	$Fe^{3+} + H_2O_2 + H^+ \longrightarrow Fe^{2+} + HOO^\bullet + H^+$	7×10^{-7}	1.26×10^5	[181]
3	$Fe^{2+} + HOO^\bullet + H^+ \longrightarrow Fe^{3+} + H_2O_2$	1.2×10^3	4.2×10^4	[89, 158]
4	$Fe^{3+} + HOO^\bullet \longrightarrow Fe^{2+} + O_2 + H^+$	2×10^1	3.3×10^4	[103, 158]
5	$Fe^{2+} + HO^\bullet + H^+ \longrightarrow Fe^{3+} + H_2O$	2.5×10^5	9×10^3	[89, 112]
6	$HO^\bullet + H_2O_2 \longrightarrow HOO^\bullet + H_2O$	2.7×10^4	1.4×10^4	[27, 36]
7	$HOO^\bullet + H_2O_2 \longrightarrow HO^\bullet + H_2O + O_2$	3×10^{-3}	3×10^4	[42, 95]
8	$2\,HOO^\bullet \longrightarrow H_2O_2 + O_2$	8.6×10^2 / s^{-1}	2.06×10^4	[21, 113]
9	$HO^\bullet + H_2 \longrightarrow H^\bullet + H_2O$	4.2×10^7	$1 \times 10^{4*}$	[27]
10	$H^\bullet + O_2 \longrightarrow HOO^\bullet$	2.1×10^{10}	$1 \times 10^{4*}$	[27]

*estimated

In [64], reactions nine and ten are not considered, therefore, the derived steady state solution overestimates the hydroxyl radical concentration. Under fuel cell operation, this flaw is further intensified by neglecting the hydoxyl radical loss rate due to the degradation mechanisms. As stated in Section 7.1 the $HO^{\bullet}$ concentration in this model is strongly overestimated due to these assumptions.

In [65, 194, 195], the influence of temperature on the reaction kinetics is neglected, only the kinetics at room temperature are considered. This makes the corresponding sets of equations useless for the simulation of chemical degradation under fuel cell operating conditions.

Therefore, the set of equations used in this work is better suited than any set used in literature to model chemical membrane degradation *in operando*. It takes into account all the relevant reactions along with temperature dependence of the reaction rates. The temperature dependence of the rate constant is described using an *Arrhenius* approach for each reaction i,

$$k^i = k^i_{ref} \exp\left[\frac{E^i_{act}}{\mathrm{R}}\left(\frac{1}{T_{ref}} - \frac{1}{T}\right)\right], \tag{7.18}$$

where T_{ref} is equal to 298.15 K.

The corresponding molar volumetric reaction rate involving educt species A and B is then calculated as

$$r^i_{mol} = \phi_{ion} k^i [A][B], \tag{7.19}$$

Table 7.2: Effective diffusion coefficients for radical species in the membrane.

Species	Diffusion coefficient / m^2 s^{-1}
$HO^\bullet$	9×10^{-10}
$HOO^\bullet$	6.8×10^{-11}
$H^\bullet$	3×10^{-9}

where $[A]$ and $[B]$ denote the molar concentrations of species A and B respectively and ϕ_{ion} is the ionomer volume fraction.

Since transport and reaction of the radical species $HO^\bullet$, $HOO^\bullet$ and $H^\bullet$ needs to be simulated, additional conservation equations of the form

$$\frac{\partial c^\kappa \phi_{ion}}{\partial t} + \nabla \cdot \left(-D^\kappa_{eff} \nabla c^\kappa \right) - q^\kappa = 0 \tag{7.20}$$

need to be solved for each species κ, where the expressions q^κ are calculated from Equation (7.19). The values for the effective diffusion coefficients of $HO^\bullet$, $HOO^\bullet$ and $H^\bullet$ are approximated with the values for H_2O, H_2O_2 and the corresponding diffusion coefficient in water respectively [65]. They are listed in Table 7.2.

7.5 Degradation Mechanisms

7.5.1 Polymer Structure

The chemical structure of Nafion®, the ionomer which is used most often in commercial fuel cells, is depicted in Figure 7.1. It consists of a PTFE-like, hydrophobic backbone. Attached to this backbone are the side chains which terminate in a sulfonic acid group. This sulfonic acid group is easily de-protonated when water is present in the membrane according to the following reaction

$$SO_3H + H_2O \rightleftharpoons SO_3^- + H_3O^+. \tag{7.21}$$

Therefore, in vicinity of the sulfonic groups, hydrophilic domains with a high concentration of protons exist in the polymer. It is this phenomenon which causes the comparably high ion conductivity of the polymer membrane.

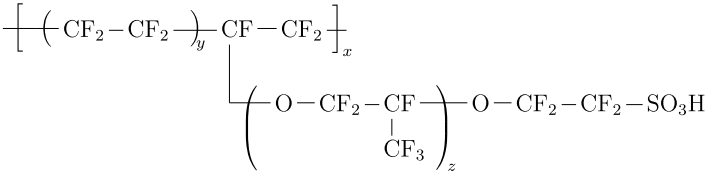

Figure 7.1: Chemical structure of Nafion®.

As explained in Section 7.1, chemical degradation of the membrane is assumed to proceeds via two distinct mechanisms: the

so-called unzipping- and side-chain scission mechanism. They will be discussed in the following.

7.5.2 Unzipping

For the unzipping mechanism, the radical attack takes place at a carboxylic acid group located on the backbone. During degradation, a CF_2 group is lost and the corresponding fluorine atoms are released as hydrogen fluoride. In this process, a new carboxylic acid group is formed on the backbone and chemical degradation may continue via this mechanism. The corresponding reactions for the unzipping mechanism are [41]

$$\mathrm{R}_f\mathrm{-CF_2-COOH} + \mathrm{HO^\bullet} \longrightarrow \mathrm{R}_f\mathrm{-CF_2^\bullet} + \mathrm{CO_2} + \mathrm{H_2O} \quad (7.22)$$

$$\mathrm{R}_f\mathrm{-CF_2^\bullet} + \mathrm{HO^\bullet} \longrightarrow \mathrm{R}_f\mathrm{-CF_2OH} \longrightarrow \mathrm{R}_f\mathrm{-COF} + \mathrm{HF} \quad (7.23)$$

$$\mathrm{R}_f\mathrm{-COF} + \mathrm{H_2O} \longrightarrow \mathrm{R}_f\mathrm{-COOH} + \mathrm{HF}. \quad (7.24)$$

Whether, these reactions really proceed as described above is questionable since the first part of reaction (7.23) involves the reaction of two radical species whose concentrations are very low. In [37] the following additional reversible reactions are introduced:

$$\mathrm{R}_f\mathrm{-CF_2}^{\bullet} + \mathrm{H_2} \rightleftharpoons \mathrm{R}_f\mathrm{-CF_2H} + \mathrm{H}^{\bullet} \tag{7.25}$$

$$\mathrm{R}_f\mathrm{-CF_2}^{\bullet} + \mathrm{H_2O_2} \rightleftharpoons \mathrm{R}_f\mathrm{-CF_2H} + \mathrm{HOO}^{\bullet} \tag{7.26}$$

$$\mathrm{R}_f\mathrm{-CF_2H} + \mathrm{HO}^{\bullet} \rightleftharpoons \mathrm{R}_f\mathrm{-CF_2}^{\bullet} + \mathrm{H_2O}. \tag{7.27}$$

Via reactions (7.25) and (7.26), the fluorocarbon radical is converted into an end group which is vulnerable due to its hydrogen atom. This group may then be reconverted via reaction (7.27).

Since these details of the unzipping mechanism remain elusive, it is simplified here, assuming a single rate determining step [168] and written as

$$\begin{aligned} &\mathrm{R}_f\mathrm{-CF_2-COOH} + 2\,\mathrm{HO}^{\bullet} \\ &\longrightarrow \mathrm{R}_f\mathrm{-COOH} + 2\,\mathrm{HF} + \mathrm{CO_2}. \end{aligned} \tag{7.28}$$

If the unzipping mechanism reaches the junction of the backbone with a side chain, the whole side chain is lost due to degradation. The process is sketched in Figure 7.2. This way, the unzipping mechanism contributes to the loss of sulfonic acid groups in the polymer.

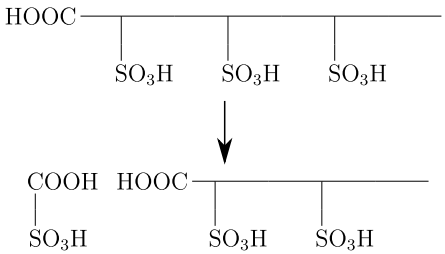

Figure 7.2: Indirect loss of a side chain due to unzipping of the backbone.

7.5.3 Side Chain Scission

For the side chain scission mechanism, the considered location for the hydroxyl radical attack on the polymer structure is the ether bond of the α-OCF_2 group on the side chain [63]. Due to this mechanism, the head group on the side chain is lost and the remainder of the side chain is assumed to be left with a vulnerable COOH group which may then be further degraded via the unzipping mechanism. Once unzipping along the side chain reaches the junction of the backbone and the side chain, two carboxylic acid groups are formed on the backbone. This way, the side chain mechanism increases the number of vulnerable groups in the polymer, leading to an increase in degradation via the unzipping mechanism. The mechanism is sketched in Figure 7.3.

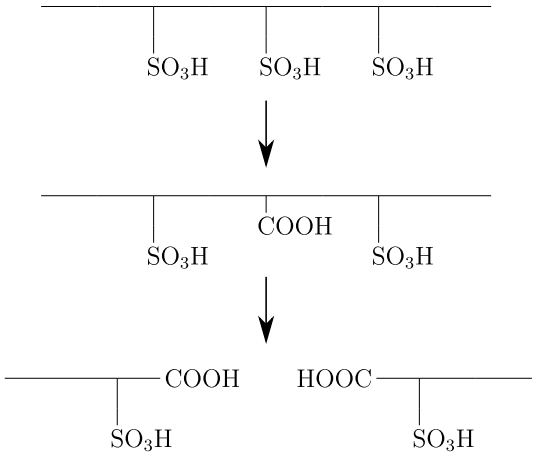

Figure 7.3: The principle of the side chain scission mechanism.

7.5.4 Degradation Model

For the modeling of chemical membrane degradation, the polymer structure is simplified using the radically coarse-grained approach of [64]. With this approach, the polymer structure is assumed to consist of three different species: the PTFE-like backbones ($bbone$), the trunk ($trunk$) and the head group ($head$) of the side chain (see Figure 7.4).

Backbone and trunk units are degraded via the unzipping mechanism, and the head groups are cut from the side chains via the side chain scission mechanism. The backbone- and trunk units may exist in an inert ($bbone$, $trunk$) or activated state ($bbone_{act}$, $trunk_{act}$), meaning that they may be immune to radical attack or vulnerable. For the backbones, this state depends on whether a carboxylic acid group is located on the backbone or not. For a

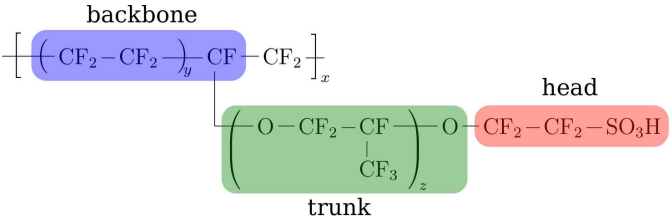

Figure 7.4: Coarse-grained structure of Nafion® according to [64].

pristine membrane, the concentration of carboxylic acid groups is low since their number can be reduced by repeated fluorination of the polymer [41]. However, it will rise due to side chain scission (Figure 7.3) in the course of degradation.

All trunk units are assumed to be initially inert but become activated when a head-group is cut from the side chain and a weak end group is formed on the side chain.

Based on these assumptions, the evolution of the polymer structure due to degradation can be described by introduction of five additional balance equations for the species $bbone$, $bbone_{act}$, $trunk$, $trunk_{act}$ and $head$. The polymer species are assumed to be immobile, therefore, the balance equations are expressed as

$$\frac{\partial \phi_{ion} c^i}{\partial t} - q^i = 0. \tag{7.29}$$

The corresponding source- and sink terms q^i will be discussed in the following.

The unzipping along the backbones and side chains is assumed to proceed in N consecutive pseudo first order reaction steps [64]. According to [44], the integrated rate $\hat{r}$ for a process with N consecutive steps, rate constant k and with the educts A and B is

$$\hat{r} = \frac{k}{N} [A] [B] . \tag{7.30}$$

For the backbones $N = N^{bbone} = 14$ and for the trunk units $N = N^{trunk} = 2$ is used in this work. These values correspond to the structural parameters of Nafion® $x = 7$ and $z = 1$ (see Figure 7.1). Variation of these parameters allows the description of polymers with varying equivalent weight due to varying side chain length or varying distance between sidechains.

The rates for the loss of activated trunk and backbone segments due to unzipping and the rate of head group loss due to scission of the side chains are

$$\hat{r}^{trunk_{act},u} = \frac{k^u}{N^{trunk}} [\mathrm{HO}^\bullet] [trunk_{act}] \tag{7.31}$$

$$\hat{r}^{bbone_{act},u} = \frac{k^u}{N^{bbone}} [\mathrm{HO}^\bullet] [bbone_{act}] \tag{7.32}$$

$$r^{head,sc} = k^{sc} [\mathrm{HO}^\bullet] [head] \tag{7.33}$$

Table 7.3: Set of degradation reactions considered in the model.

Nr.	Reaction	k / m^3 mol^{-1} s^{-1}	E_{act} / J mol^{-1}	Ref.
11	$HO^{\bullet} + \text{head} \longrightarrow \text{products}$	3.7×10^6	$7 \times 10^{4*}$	[45]
12	$HO^{\bullet} + \text{trunk}_{\text{act}} \longrightarrow \text{products}$	7.9×10^5	7×10^4	[45, 65]
13	$HO^{\bullet} + \text{backbone}_{\text{act}} \longrightarrow \text{products}$	7.9×10^5	7×10^4	[45, 65]

*estimated

respectively, where the rate constants are calculated according to Equation (7.18) and the superscripts u and sc represent the unzipping- and side chain scission mechanism respectively. The parameters for the degradation reactions are listed in Table 7.3.

The indirect loss rates of trunk-, activated trunk- and head groups due to unzipping of the backbone (Figure 7.2) are formulated as

$$r^{trunk,u_{in}} = \hat{r}^{bbone_{act},u} \frac{[trunk]}{[head_{init}]} \tag{7.34}$$

$$r^{trunk_{act},u_{in}} = \hat{r}^{bbone_{act},u} \frac{[trunk_{act}]}{[head_{init}]} \tag{7.35}$$

$$r^{head,u_{in}} = \hat{r}^{bbone_{act},u} \frac{[head]}{[head_{init}]} \tag{7.36}$$

respectively. The superscript u_{in} denotes the indirect loss due to unzipping.

From these expressions for the reaction rates, the source- and sink terms q^i of the balance equations (7.29) are calculated as

$$q^{head} = -r^{head,sc} - r^{head,u_{in}} \tag{7.37}$$
$$q^{trunk_{act}} = r^{head,sc} - \hat{r}^{trunk_{act},u} - r^{trunk_{act},u_{in}} \tag{7.38}$$
$$q^{trunk} = -r^{head,sc} - r^{trunk,u_{in}} \tag{7.39}$$
$$q^{bbone_{act}} = 2\hat{r}^{trunk_{act},u} \tag{7.40}$$
$$q^{bbone} = -2\hat{r}^{trunk_{act},u} - \hat{r}^{bbone_{act},u}. \tag{7.41}$$

An experimental approach to evaluate the chemical degradation of the membrane, is the measurement of the FER. In order to be able to compare the simulation results with experimental data, the calculation of the area specific fluorine release rate is incorporated into the model. The source of fluorine atoms in each control volume is calculated as

$$\begin{aligned} q^{\mathrm{F}} = &\left(r^{head,sc} + r^{head,u_{in}}\right) N^{\mathrm{F},head} \\ &+ \left(\hat{r}^{trunk_{act},u} + r^{trunk,u_{in}} + r^{trunk_{act},u_{in}}\right) N^{\mathrm{F},trunk} \\ &+ \hat{r}^{bbone_{act},u} N^{\mathrm{F},bbone}, \end{aligned} \tag{7.42}$$

where $N^{\mathrm{F},head}$, $N^{\mathrm{F},trunk}$ and $N^{\mathrm{F},bbone}$ are the number of fluorine atoms per head-, trunk- and backbone unit respectively. The cor-

responding values are 4, 6 and 28 in accordance with the values for N^{bbone} and N^{trunk}. For comparison with the experimental data the volumetric source q^{F} is integrated over the membrane volume and divided by the simulated cell area.

7.6 Initial-, Boundary- and Coupling Conditions

The relationships used for the calculation of the initial conditions in the PEM domain are listed in Table 7.4.

In the electrodes, the initial mole fraction of hydrogen peroxide is set to zero and the concentrations of Fe^{2+} and Fe^{3+} is set to 8.75×10^{-3} mol m^{-3} (0.5 ppm) in accordance with the initial conditions in the PEM domain.

The boundary conditions for hydrogen peroxide in the electrodes are set according to Section 4.7 on page 75 ($x_{g,inlet}^{\mathrm{H_2O_2}} = 0$). For the iron ions, similar to the protons, *Neumann* no flow conditions are applied on the CL/MPL interfaces. For the polymer and radical species, *Neumann* no flow conditions are set on the boundary of the PEM domain. A summary of the boundary conditions is depicted in Figure 7.5.

For the coupling of H_2O_2 transport in the electrodes and the polymer electrolyte membrane, chemical equilibrium is assumed. In the PEM domain, a *Dirichlet* type coupling condition is set. The molar concentration of hydrogen peroxide on the coupling interfaces is calculated from the local conditions in the electrodes.

Table 7.4: Relationships used for the calculation of the initial conditions in the PEM domain.

Property / Equation	Units
Polymer density:	
$\rho_{PEM} = 2000$	kg m^{-3}
Polymer chain lengths:	
$N^{bbone} = 14$	-
$N^{trunk} = 2$	-
Molar mass:	
$M^{head} = M^{\mathrm{S}} + 3M^{\mathrm{O}} + 2M^{\mathrm{C}} + 4M^{\mathrm{F}}$	kg mol^{-1}
$M^{bbone} =$	
$\left(M^{\mathrm{C}} + 2M^{\mathrm{F}}\right) N^{bbone} + M^{\mathrm{C}} + M^{\mathrm{F}}$	kg mol^{-1}
$M^{trunk} =$	
$\left(M^{\mathrm{C}} + 2M^{\mathrm{F}}\right) N^{trunk} + 2M^{\mathrm{O}} + M^{\mathrm{C}} + 2M^{\mathrm{F}}$	kg mol^{-1}
Equivalent weight:	
$EW_{init} = M^{head} + M^{bbone} + M^{trunk}$	kg mol^{-1}
Initial concentrations:	
$c_{init}^{\mathrm{Fe}^{2+}} = c_{init}^{\mathrm{Fe}^{3+}} = 8.75 \times 10^{-3*}$	mol m^{-3}
$c_{init}^{head} = \rho_{PEM}/EW_{init}$	mol m^{-3}
$c_{init}^{bbone_{act}} = 0.004 c_{init}^{head}$	mol m^{-3}
$c_{init}^{bbone} = (1 - 0.004)\, c_{init}^{head}$	mol m^{-3}
$c_{init}^{trunk} = c_{init}^{head}$	mol m^{-3}
$c_{init}^{trunk_{act}} = c_{init}^{\mathrm{HO}^{\bullet}} = c_{init}^{\mathrm{HOO}^{\bullet}} = c_{init}^{\mathrm{H}^{\bullet}} = c_{init}^{\mathrm{H_2O_2}} = 0$	mol m^{-3}

* corresponds to 0.5 ppm

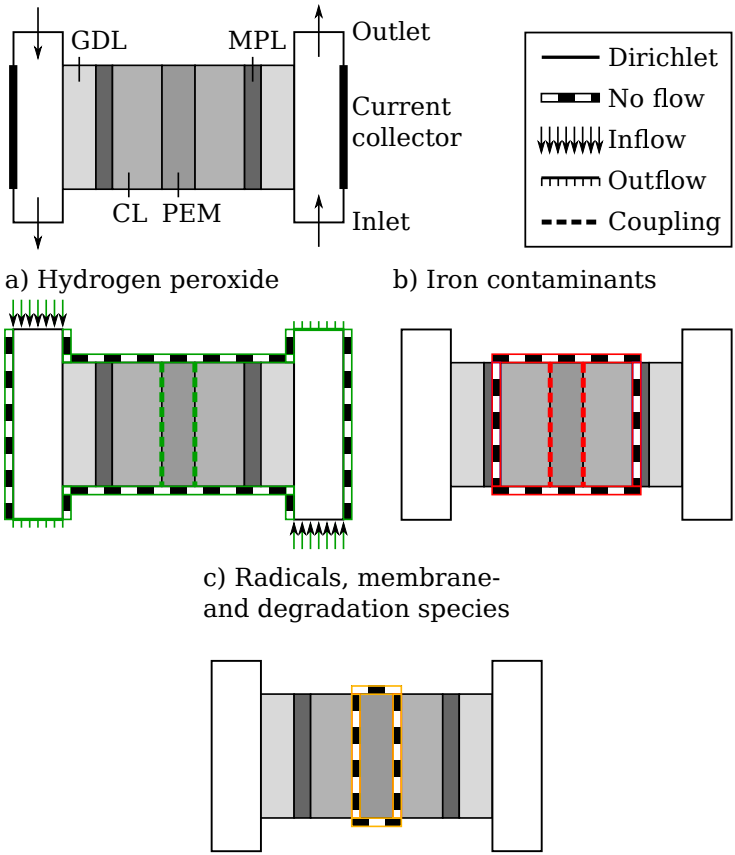

Figure 7.5: Summary of the boundary conditions for the degradation model.

Table 7.5: Operating conditions of the ASTs.

Test	RH / %	p_{anode} / Pa	$p_{cathode}$ / Pa
1	30	1.5×10^5	1.5×10^5
2	30	2.5×10^5	2.3×10^5
3	75	2.5×10^5	2.3×10^5

It is calculated using equations (7.6), (7.7) and (7.9). In return, a *Neumann* type flux coupling condition in the electrode domains is set.

The coupling for the transport of iron ions is also based on the assumption of chemical equilibrium and the iron concentration across the CL/PEM interface is assumed to be continuous.

7.7 Results - Degradation

To demonstrate the reliability of the chemical degradation model, it is validated against the experimental data of [29]. The authors carried out accelerated stress tests (ASTs) to evaluate the chemical membrane degradation under varying relative humidity and pressure. The operating conditions of the ASTs are listed in Table 7.5.

For all conditions, the cell temperature is set to 368.15 K and the lambda control parameters for hydrogen and oxygen are 1.2 and 2 respectively. In each test condition, a sequence of four current densities was applied to investigate the influence of cell voltage

on the chemical degradation. For test case 1 and 2, the applied sequence was 7500, 4000, 2000 and 0 A m^{-2}, for condition 3, 7500, 2000, 600 and 0 A m^{-2} was used. Each sequence was started at the highest current density, since degradation was expected to be lowest in this condition and to avoid pollution of subsequent water samples with previously released fluorine ions. The cells were operated at constant current for approximately one week for each current density. At OCV, the minimum current I_{min} for the lambda control (see Equation (4.78) on page 75) was set to 1000 A m^{-2} and the corresponding lambda control parameters were set to a value of 10 to increase the amount of water in the exhaust streams.

Samples of the exhaust water from the anode and cathode side of the cell were collected after the condenser every 24h. The mass of exhaust water was measured and the corresponding flow rate was determined. The fluoride ions concentration in the effluent water was then measured using chromatography.

Further, SEM was used to determine the location of degradation and membrane thinning across the CLs and PEM.

The cells where electrochemically characterized by polarization curve- and EIS measurements.

7.7.1 Cell Performance

To make sure that the simulated conditions of the AST resemble the experimental ones, the modeling results are compared to experimental polarization curves and impedance spectra. Figures

7.6 and 7.7 show the experimental and simulated polarization curves for two conditions.

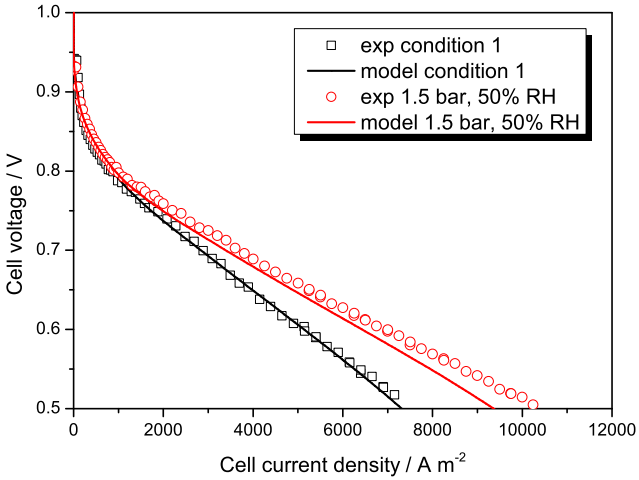

Figure 7.6: Experimental and simulated polarization curves for test case 1 and for an operating pressure of 1.5 bar and 50% relative humidity.

It should be noted that all model parameters used for the validation study, listed in Table 6.3 on page 124, were left unchanged except those listed in Table 7.6.

Even though the cell geometry was adapted to the new cell type, spatial parameters of the cell layers were adjusted and variations in the operating conditions (lambda-control and counter-flow mode) had to be incorporated, these changes are not considered as a part of the fitting procedure. To fit the polarization curves only the parameters which are expected to vary with a different

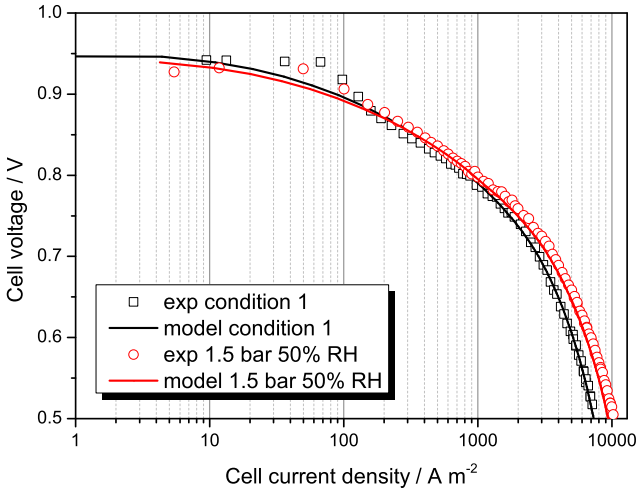

Figure 7.7: Experimental and simulated cell voltage over the logarithm of the cell current density for test case 1 and for an operating pressure of 1.5 bar and 50% relative humidity.

CL composition, e.g. platinum loading and ionomer properties, were adjusted. Since structural changes in the CLs might influence the ORR kinetics, slight variations of the corresponding parameters were used for the fitting procedure. Still the agreement between experiment and simulation is reasonable which demonstrates the predictive capabilities of the model.

Table 7.6: Model parameters used for the degradation study.

Parameter	Units	Reference
Operating mode:		
counter-flow		
Cell geometry:		
$A_{cell} = 1.04$	m^2	measured
$A_{inlet} = 0.89 \times 10^{-3}$	m^2	measured
$d_{channel} = 1.4 \times 10^{-3}$	m	measured
$d_{GDL} = 190 \times 10^{-6}$	m	estimated
$d_{MPL} = 45 \times 10^{-6}$	m	estimated
$d_{CL,anode} = 6 \times 10^{-6}$	m	estimated
$d_{CL,cathode} = 12 \times 10^{-6}$	m	estimated
$d_{PEM} = 25 \times 10^{-6}$	m	[6]
$l_{channel} = 1.04$	m	measured
Grid:		
$n_{cells,x,PEM} = 15$	-	-
$n_{cells,x,CL,anode} = 10$	-	-
$n_{cells,y,inlet} = n_{cells,y,outlet} = 1$	-	-
Spatial parameters:		
$\mathbf{K}_{channel} = \mathbf{K}_{inlet}$ $= \mathbf{K}_{outlet} = \mathbf{K}_{tube} = 1.633 \times 10^{-7}$	m^2	fitted
$\mathbf{K}_{GDL} = 6.74 \times 10^{-14}$	m^2	measured
$\mathbf{K}_{MPL} = 6.74 \times 10^{-15}$	m^2	estimated

Table 7.6: Model parameters used for the degradation study continued.

Parameter	Units	Reference
$\mathbf{K}_{CL} = 6.74 \times 10^{-15}$	m^2	estimated
$\phi_{channel} = \phi_{inlet} = \phi_{outlet} = \phi_{tube} = 1$		
$\phi_{GDL} = 0.77$		estimated
$\phi_{MPL} = 0.35$		estimated
$\phi_{CL} = 0.47$		estimated
$r_{pore,MPL} = 20 \times 10^{-9}$	m	estimated
$\theta_{GDL} = 112$	°	estimated
$\theta_{MPL} = 112$	°	estimated
$\theta_{CL} = 112$	°	estimated
$\phi_{ion,PEM} = 1$ (0.8 in reinforced layer)		estimated
Lambda control:		
$i_{min} = 1000$	A m^{-2}	
$\lambda^{flux,O_2} = \lambda^{flux,H_2} = 10$ (OCV)		
$\lambda^{flux,O_2} = 2$ (under load)		
$\lambda^{flux,H_2} = 1.2$ (under load)		
ORR:		
$i^0_{ref} = 1.8 \times 10^{-3}$	A m^{-2}	fitted
$\alpha^f_{high} = \alpha^r_{high} = 0.45$	-	fitted
ECSA:		
$r_{Pt,anode} = 3 \times 10^{-9}$	m	estimated

Table 7.6: Model parameters used for the degradation study continued.

Parameter	Units	Reference
Double layers:		
$C_{DL,anode} = C_{DL,cathode} = 1.25 \times 10^7$	F m^{-3}	fitted
CL conductivity:		
$A = 5 \times 10^{-2}$	S m^{-1}	fitted
$B = C = 2$	-	fitted
Ionomer film model:		
$\delta_{ion} = 10 \times 10^{-9}$	m	fitted
$A = 3.4 \times 10^3$	s m^{-1}	fitted
$B = 3 \times 10^4$	s m^{-1}	fitted
$C = -4$	-	fitted

Good agreement between the experimentally measured and the simulated OCV is achieved. This is important since the chemical membrane degradation is most severe in this condition. The open circuit voltage increases with reduced relative humidity of the inlet gases due to the resulting increase in oxygen concentration in the cathode compartment and therefore faster ORR kinetics. Again, higher relative humidity leads to an increase in cell performance due to the reduced transport resistances in the ionomer of the catalyst layers and the membrane.

In Figures 7.8 and 7.9, the *Nyquist* plots of the experimental and simulated impedance corresponding to conditions 1 and 2 and conditions 2 and 3 at 400 A m^{-2} are depicted respectively. Strong deviations in the semi-circle corresponding to the ORR are observed even though good agreement between experiment and simulation is achieved in the slope of the polarization curve at this current density. As discussed in Chapter 6, this may be explained by an underestimation of inductive and capacitive phenomena in the model due to three-dimensional effects.

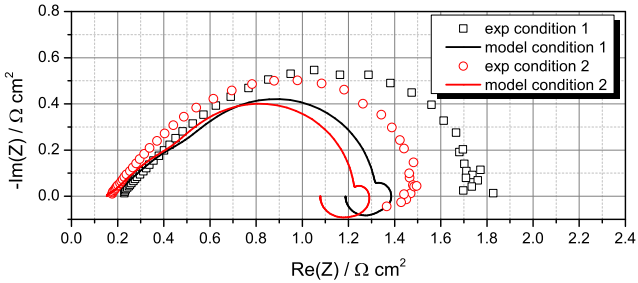

Figure 7.8: *Nyquist*-plot for test cases 1 and 2.

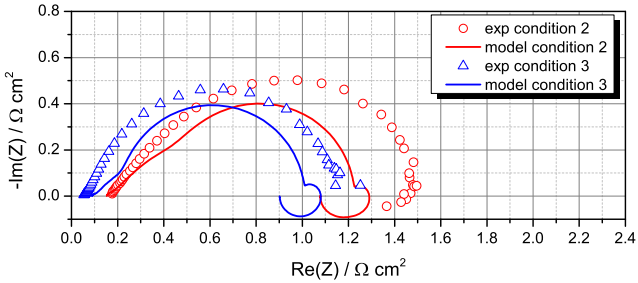

Figure 7.9: *Nyquist*-plot for test cases 2 and 3.

In Figures 7.10 and 7.11, the *Bode* plots of the experimental and simulated impedance at 400 A m^{-2} of conditions 1 and 2 and conditions 2 and 3 respectively are depicted. Similar to the results of Section 6.3.3 on page 144, qualitative agreement between experiment and simulation can be observed.

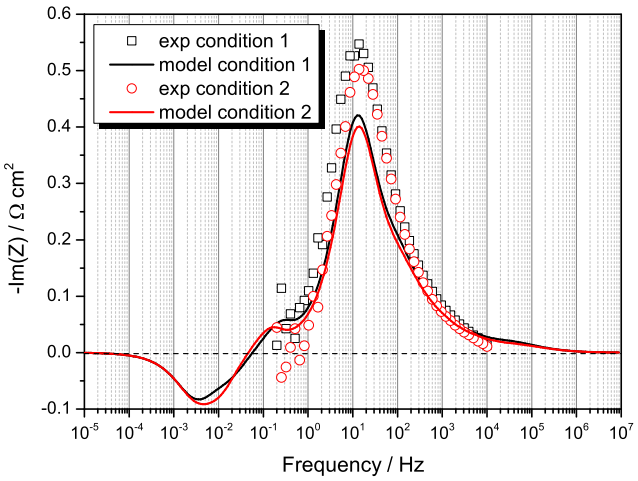

Figure 7.10: *Bode*-plot for test cases 1 and 2.

From Figures 7.8 and 7.9 the ohmic resistance of the cell can be obtained from the intercept of the curve with the axis of the real part of the impedance in the high frequency domain on the left. Higher pressure and relative humidity lead to a decrease in ohmic resistance due to improved humidification of the polymer electrolyte membrane and therefore increased ionic conductivity. This trend is well captured by the performance model. A good description of the ohmic resistance is important since the transport of iron ions depends on the ionic potential

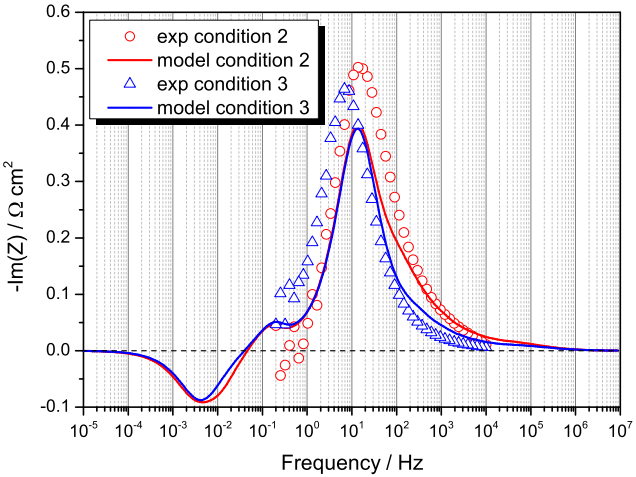

Figure 7.11: *Bode*-plot for test cases 2 and 3.

gradients (see Equation (7.15)). Therefore, it is highly relevant for the chemical degradation.

7.7.2 Effect of Pressure and Relative Humidity

The chemical membrane degradation model was employed to simulate the evolution of the FER at OCV for the three experimental conditions listed in Table 7.5. For all simulations of chemical degradation presented in this chapter, the set of initial conditions listed in Table 7.4 is used. With these simulations, the effect of pressure and relative humidity on the chemical membrane degradation are rationalized and the kinetics of the degradation reactions are validated.

Figure 7.12 shows the simulated fluoride emission rate at OCV for the three test conditions over time along with the experimental data. In this plot, the experimental FERs determined from the anode and cathode exhaust water samples were summed up. For the simulations, the cell was operated in galvanostatic mode at a current density equal to zero. Open circuit voltage was held for the time of the corresponding test condition.

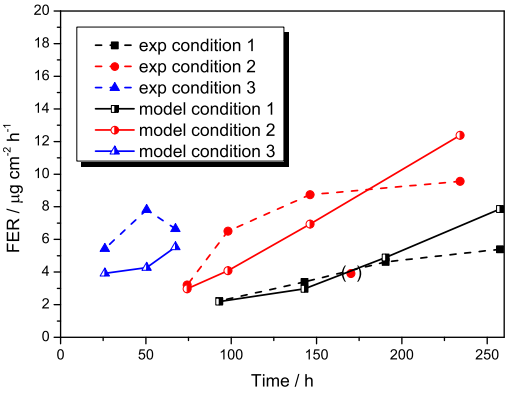

Figure 7.12: Experimental and simulated FER for test cases 1, 2 and 3.

Experimentally, for test condition 1, a continuous increase of the FER with time is observed. However, for conditions 2 and 3 the trend is not as clear since the corresponding data sets contain points exhibiting strong deviations from the expected behavior and the test duration of condition 3 was only about 65 hours due to test bench issues [29].

An increase in pressure leads to an increase in the FER as can be observed from the curves corresponding to condition 1 and 2. Increased pressure leads to increased oxygen concentration in the cathode compartment of the cell. Therefore, the oxygen cross-over from the cathode to the anode side across the membrane is stronger. Consequently, more hydrogen peroxide is formed at the anode and the rate at which the hydroxyl radicals are formed increases.

Elevated relative humidity (condition 3) further increases the chemical membrane degradation at open circuit voltage. This is caused by an increase in membrane humidification which results in higher oxygen permeation (Equation (4.15) on page 40) through the membrane. The FER in this condition is underestimated. This may be due to earlier degradation at lower cell voltage during the test which may have caused an increase in the number of weak end groups in the polymer.

For conditions 1 and 2, it may be observed that in the beginning of the AST the degradation rate increases and then approaches a plateau towards the end of the test. This can be explained when the contributions of the different degradation mechanisms to the overall FER as obtained from the model are considered. In Figures 7.13, 7.14 and 7.15 the contributions of each degradation mechanism to the overall FER are depicted for the three conditions.

In the beginning of the test, the main source of fluoride is loss of head groups (reaction 11). With time, this reaction slows down because the concentration of head groups in the polymer decreases. However, as depicted in Figure 7.3, after the head

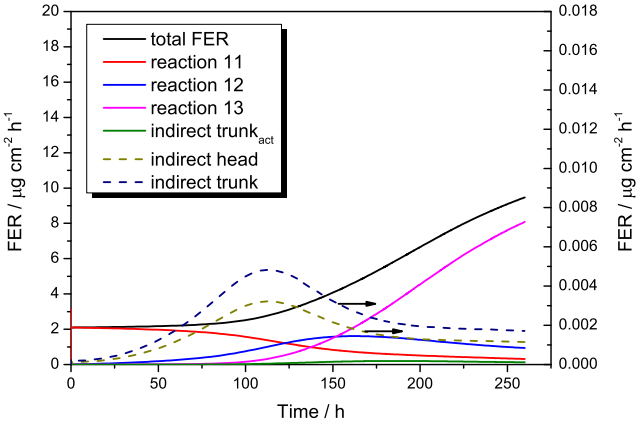

Figure 7.13: Contributions to the overall FER for test case 1.

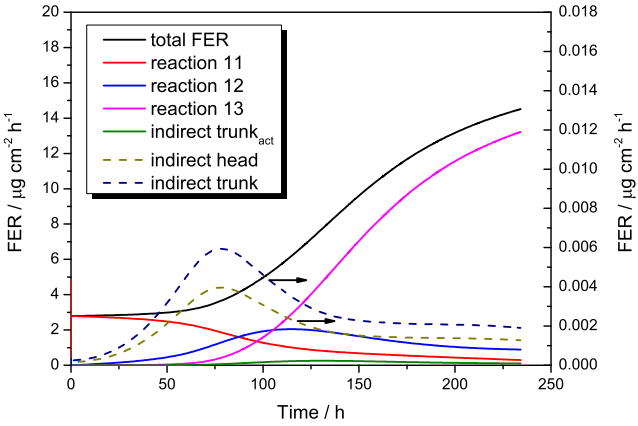

Figure 7.14: Contributions to the overall FER for test case 2.

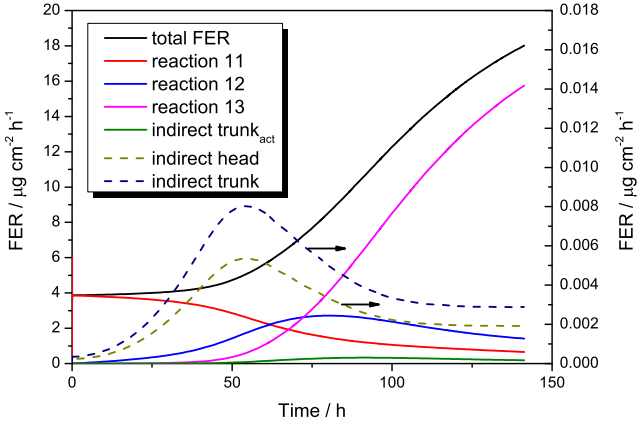

Figure 7.15: Contributions to the overall FER for test case 3.

group is lost, degradation will proceed along the side chain (reaction 12) and finally two carboxylic acid groups on the polymer backbone will be generated. Therefore, for longer test durations, degradation via the unzipping mechanism (reaction 13) becomes dominant.

For short test durations, the fluoride emission resulting from degradation of the activated trunk units is inversely proportional to the FER resulting from head group loss since one activated trunk unit is formed for each head group lost (Equation (7.38)). For longer test durations, this relation no longer holds because the rate at which trunk units are lost outweighs the rate at which they are produced. With the parameters used in this work, the contributions of indirect head and trunk loss to the overall FER are insignificant. This is due to the fact that these indirect losses are caused by the unzipping mechanism which becomes only

relevant when the head groups and trunk unit concentrations are already reduced.

As can be observed in Figure 7.12, the FER is overestimated by the model for longer test durations. This indicates that a mechanism is missing in the degradation model. Further, it should be noted that the available measurements are not sufficient to clarify the discrepancy between model and experiment and the experimental uncertainties are expected to be high.

This mechanism is very likely the elimination of activated backbones due to unzipping. It will occur when unzipping along the backbone proceeds from two ends of a polymer chain and the two COOH groups reach each other. In this case, two weak end groups or, in terms of the coarse-grained polymer structure, two activated backbones, will be eliminated in the system. With an increasing number of COOH groups on the polymer backbone due to scission and unzipping of the side chains, the probability that this mechanism becomes operative will increase. Or, in other words, the shorter the polymer chains, the faster the elimination mechanism. Consequently, with more defects on the polymer backbone, the degradation rate due to unzipping will reach a plateau and therefore, the overall FER.

To incorporate this mechanism into the model is not trivial. To estimate, when the elimination mechanism occurs, one would have to know the length distribution of the polymer chains in the membrane. This is possible, however, it is computationally extremely demanding. The length distribution of the polymer chains could be divided into discrete classes. Then, for each of these classes, an additional balance equation could be solved.

In the course of degradation, the length of polymer chains will decrease. This change will depend on the location of side chain scission on the polymer chain which is a statistical process. E.g. side chain scission in the middle of one of the longest polymer chains will reduce the number of polymer chains with maximum length by one and increase the number of polymer chains with half of the maximum length by two. If the side chain scission takes place close to the chain end, a short chain and a chain with length slightly smaller than the maximum chain length will be formed, changing the chain length distribution in a different way. The probability that a chain of a certain length is attacked will depend on the chain length distribution.

Since the polymer chains consist of approximately 1000 repeat units depicted in Figure 7.1, depending on the width of the chain length classes, $\sim$ 25 to 50 additional balance equations would have to be solved in order to resolve the chain length distribution and to account for the elimination mechanism of activated backbone units. This task is left for future modelers.

7.7.3 Effect of Cell Voltage

To further validate the degradation model, the dependence of chemical degradation on the cell voltage is investigated. For this purpose, potentiostatic simulations where carried out. The cell voltage was ramped from 1 V to the desired value during 10^4 seconds and then held constant for 1000 seconds in order to reach the corresponding steady state. During this period, the chemical degradation reactions where switched off in order to

avoid degradation due to the initially high cell voltage. Then, the chemical degradation reactions where switched on and the cell voltage was held constant for 140 hours. This protocol was applied for simulations at 0.4, 0.5, 0.6, 0.7, 0.75, 0.8, 0.85, and 0.9 V in the operating conditions of the three test cases. For comparison with the experiments, the FER was integrated over the degradation time of 140 hours.

In Figures 7.16 and 7.17, the experimental and simulated FER is plotted as a function of the cell voltage.

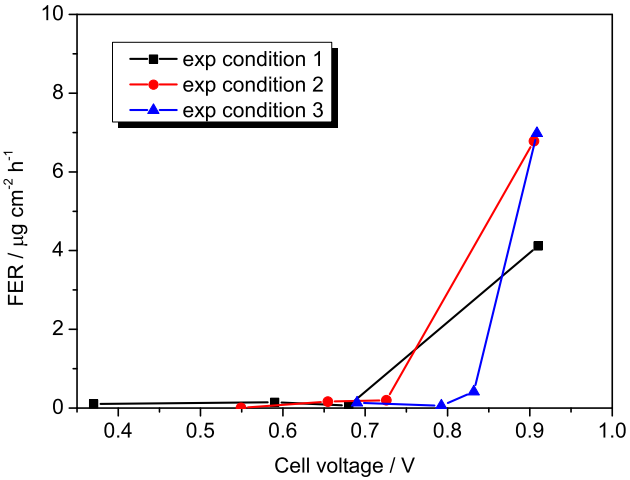

Figure 7.16: Experimental FER as a function of cell voltage [29].

For all three test conditions, the degradation rate is highest at OCV. Lower cell voltage, leads to a decrease of the FER and chemical degradation becomes insignificant below ∼0.8 V. For the dry test condition 1 and 2, the decrease of membrane degradation with cell voltage is more pronounced. In these conditions,

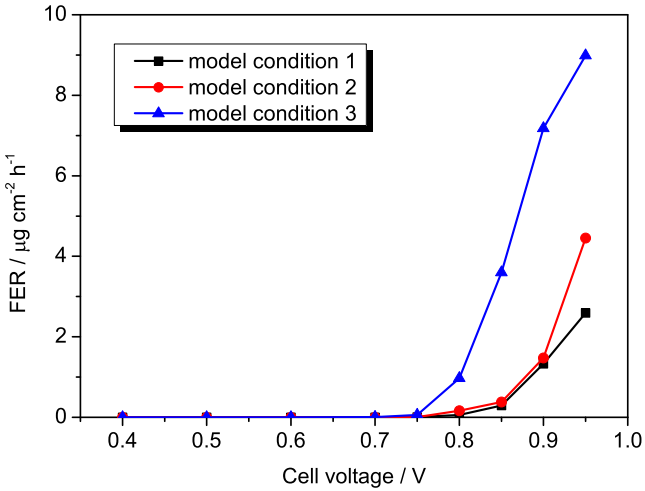

Figure 7.17: Simulated FER as a function of cell voltage.

the membrane hydration is low and therefore the ionic conductivity. Consequently, when a current is drawn from the cell, the gradients of the ionic potential across the CLs and PEM become larger. Therefore, the iron ions are dragged to the cathode electrode and less Fe^{3+} reaches the anode where it is reduced to Fe^{2+} due to the high overpotential of reaction (7.12). At lower cell voltage, the membrane is swept clean from the contaminants and the main radical formation reaction of Fe^{2+} and H_2O_2 (Reaction 1 of Table 7.1 on page 171) ceases.

In the conditions of test case 3 the membrane humidification is higher which results in smaller potential gradients. This allows more Fe^{3+} to be reduced at the anode. Therefore, the overall FER is higher and the reduction of degradation with decreasing cell voltage is less pronounced.

To illustrate the effect of cell voltage on the degradation, in Figure 7.18, the distribution of ferrous ions in the CLs and PEM is depicted for OCV 0.85 and 0.7 V in condition 1.

At OCV, the maximum concentration of Fe^{2+} is found in the ACL. Due to gradients of the ionic potential, this maximum shifts to the cathode side at 0.85 and 0.7 V. Since iron is assumed to stay in the ionomer phase, it cannot leave the CLs. Therefore, the highest concentration is found at 0.7 V at the CCL/MPL interface. For lower cell voltage, most parts of the CLs and PEM are effectively swept clean from the contaminants.

It should be noted that the strong voltage dependence of the iron distribution is due to the correction factor for the *Nernst-Einstein* relation applied for the calculation of the iron ion diffusion coefficient in Equation (7.16) on page 169.

In Figure 7.19 the simulated distribution of hydrogen peroxide in the CLs and PEM is depicted.

The high *Henry* coefficient of H_2O_2 in water leads to an increased concentration inside the PEM domain. Due to the high overpotential of reaction (7.1) at the anode and the operation in counter-flow mode, the maximum concentration of H_2O_2 is located at the anode inlet (top left). At 0.7 V the maximum shifts towards the cathode inlet because of the kinetics of reaction (7.1) and the higher oxygen concentration in this location.

The combination of the presence of Fe^{2+} and H_2O_2 governs the chemical membrane degradation since hydroxyl radicals are mainly formed via reaction 1 (Table 7.1). Figure 7.20 shows the

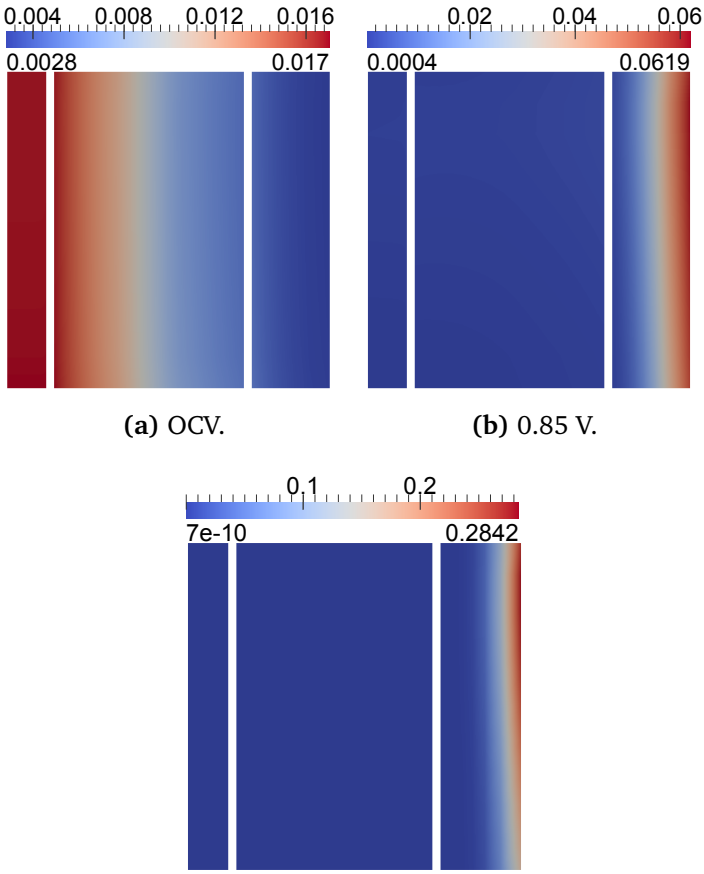

(a) OCV. **(b)** 0.85 V.

(c) 0.7 V.

Figure 7.18: Influence of cell voltage on chemical degradation: The concentration of Fe^{2+} / mol m^{-3} in the CLs (left and right) and PEM (center).

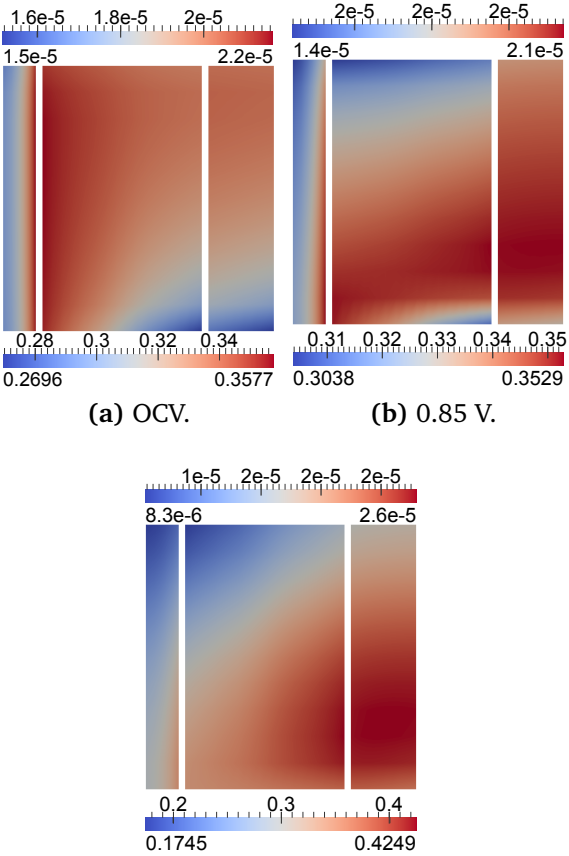

(a) OCV. **(b)** 0.85 V.

(c) 0.7 V.

Figure 7.19: Influence of cell voltage on chemical degradation: The concentration of H_2O_2 / mol m^{-3} in the Cls (left and right) and the PEM (center). Upper scale: concentration in the CLs, lower scale: concentration in the PEM.

distribution of the degradation rate in the PEM for OCV, 0.85, 0.7 V in condition 1.

At OCV, the FER is almost uniform along the channel and located at the ACL/PEM interface. At 0.85 V, it is reduced by an order of magnitude and the maximum is shifted towards the cathode outlet. Since the PTFE reinforcement layer reduces the volume fraction of ionomer in the PEM in the central region, the FER is decreased here. At 0.7 V, the degradation rate is further reduced by three orders of magnitude compared to OCV. In this condition, chemical membrane degradation becomes insignificant.

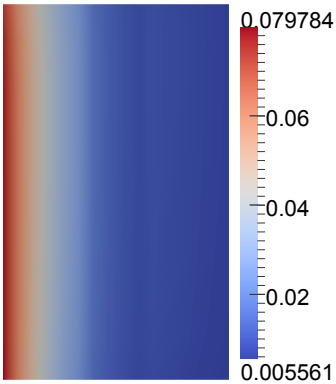

(a) OCV.

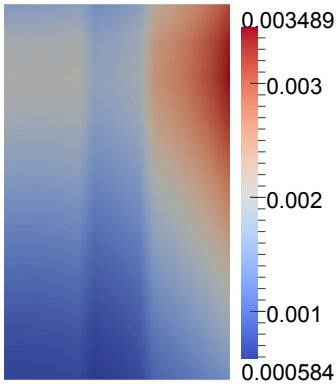

(b) 0.85 V.

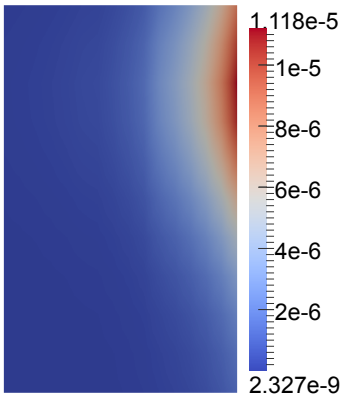

(c) 0.7 V.

Figure 7.20: Influence of cell voltage on chemical degradation: Distribution of the volumetric FER / mol m^{-3} s^{-1} in the PEM.

8 Summary and Outlook

Guybrush: At least I've learnt something from all of this.
Elaine: What's that?
Guybrush: Never pay more than 20 bucks for a computer game.
Elaine: A what?
Guybrush: I don't know. I have no idea why I said that.

(The Secret of Monkey Island)

Summary

In this work, the numerical framework NEOPARD-X for the simulation of electrochemical cells like fuel cells and electrolyzers has been established based on existing open-source software [15, 16, 54].

Physical models for the description of PEMFC performance have been incorporated into the framework. It allows transient simu-

lations in two- or three-dimensional setups. The incorporated processes are:

- Non-isothermal, compositional multi-phase flow in both electrodes.
- Non-isothermal, transport of water and gaseous species in the polymer electrolyte membrane.
- Ionic and electrical charge transport.
- Detailed ORR kinetics combined with mechanistic models for platinum oxide formation and oxygen transport in ionomer thin films.

The model has been verified and validated under different operating conditions and for different cell types.

Based on the established model, a detailed analysis of the simulated EIS was possible, revealing that low frequency inductive phenomena must be operative in PEMFCs. These phenomena are due to:

1. Change of ionic conductivity of the ionomer with water activity.
2. Changing coverage of the platinum oxides on the catalyst surface with cell voltage.

Further, it was found that diffusion cannot be the source for the low frequency capacitive peak observed in impedance spectra, which is a widespread misconception in the PEMFC community. In fact, the peak is mainly caused by oxygen and hydrogen concentration gradients in the in-plane dimension of the cell.

In the anode, transport of hydrogen into the catalyst layer must proceed via convection.

The capabilities of the PEMFC model were extended for the simulation of chemical membrane degradation. For this purpose the following mechanisms were implemented:

- Hydrogenperoxide formation and transport in the electrodes and the membrane.
- Transport of ferrous and ferric ions in the ionomer phase of the catalyst layers and the membrane.
- Chemical membrane degradation due to radical attack via two distinct mechanisms: unzipping and side-chain scission.

The degradation model has been validated against experimental data in different operating conditions and it was found that chemical degradation is stronger under wet conditions due to an increase in oxygen cross-over through the membrane. Further, higher operating pressure leads to increased degradation for the same reason. Chemical membrane degradation strongly depends on the cell voltage: it is most pronounced at OCV and becomes insignificant below 0.8 V. An explanation for this phenomenon is the changing distribution of iron ions in the CLs and PEM with cell voltage. At OCV, iron in high concentration is located at the anode side. With decreasing cell voltage, the ions are dragged to the cathode and the degradation ceases.

Outlook

With the physical PEMFC model, developed in this work, the contributions of different processes to the overall cell impedance can be identified. In combination with systematic distributed relaxation time (DRT)-analysis of experimental impedance spectra [152, 163], the model will yield a powerful tool allowing in depth analysis of physical processes inside fuel cells. From such an analysis, the factors, limiting the cell performance, can be identified and guidance for improved cell design can be obtained.

In order to achieve this goal, the performance model has to be improved. Two approaches to reach this goal are presented in the following.

1. Numerical robustness: The model as such is already numerically quite robust. However, phase transitions (e.g. the formation of liquid water from a saturated vapor phase) still cause convergence problems even though measures were taken to reduce this problem (Section 4.3.3 on page 49). Consequently, a new formulation for multi-phase transport or a specialized solver, tailored for this problem, needs to be developed.
2. Parallelization: For now, only simulations in a simplified along-the channel geometry are possible. In order to resolve the real geometry of a fuel cell with realistic flow field in 3D, the model needs to be parallelized since the computational effort will increase massively. One possibility is the exploitation of DUNE's algebraic multigrid (AMG)

solver parallel computing capabilities [7]. However, due to the use of multidomain and multidomaingrid [126, 127] for the present model, the resulting matrix representing the linear system of equations that has to be solved in each time-step of a simulation cannot be handled by the AMG solver. With a single domain approach for all layers of the fuel cell, similar to the one presented e.g. in [71, 185], this problem could be avoided. The second option would be a domain decomposition approach similar to the one demonstrated in [146, 147].

As discussed in Chapter 7, the chemical membrane degradation model needs improvement in order to account for the elimination of activated backbones due to the unzipping mechanism.

Further, the influence of radical scavengers which are used in state-of-the-art membranes could be incorporated [24, 38, 142]. E.g. Ce^{3+} is an effective radical scavenger which reacts with $HO^{\bullet}$ via the following reaction.

$$Ce^{3+} + HO^{\bullet} + H^{+} \longrightarrow Ce^{4+} + H_2O \tag{8.1}$$

It is further regenerated via

$$Ce^{4+} + H_2O_2 \rightleftharpoons Ce^{3+} + HOO^{\bullet} + H^{+} \tag{8.2}$$

and

$$Ce^{4+} + HOO^{\bullet} \longrightarrow Ce^{3+} + O_2 + H^{+}. \tag{8.3}$$

Since these reactions are not considered in the present model, the assumed concentrations of the iron contaminants may be too low.

Finally, the coupling of chemical degradation and cell performance developed in [39, 40] could be incorporated. However, in order to quantify the influence of chemical membrane degradation on the cell performance, one would also need quantitative data on the influence of other degradation mechanisms like platinum dissolution or delamination on the cell performance.

Bibliography

[1] URL: https://www.kern.de/de/technisches-datenblatt/polytetrafluorethylen-ptfe?n=1601_1 (cit. on p. 42).

[2] URL: http://www.azom.com/article.aspx?ArticleID=1630#_Natural_Graphite (cit. on p. 55).

[3] URL: http://www.dumux.org/documents/dumux-handbook-2.11.pdf (cit. on pp. 88, 89).

[4] URL: http://www.fuelcellstore.com/spec-sheets/nafion-xl-spec-sheet.pdf (cit. on p. 120).

[5] URL: https://www.psenterprise.com/ (cit. on p. 159).

[6] URL: http://www.fuelcellstore.com/spec-sheets/nafion-211-212-spec-sheet.pdf (cit. on p. 190).

[7] URL: https://www.dr-blatt.de/static/media/2012/09/dune_parallel_amg.pdf (cit. on p. 213).

[8] M. Acosta, C. Merten, G. Eigenberger, H. Class, R. Helmig, B. Thoben, H. Müller-Steinhagen. "Modeling non-isothermal two-phase multicomponent flow in the cathode of PEM fuel cells." In: *Journal of Power Sources* 159.2 (Sept. 2006), pp. 1123–1141. DOI: 10.1016/j.jpowsour.2005.12.068 (cit. on p. 30).

[9] A. J. Appleby. “Oxygen Reduction on Bright Osmium Electrodes in 85% Orthophosphoric Acid.” In: *Journal of The Electrochemical Society* 117.3 (1970), pp. 328–335. DOI: 10.1149/1.2407759 (cit. on pp. 31, 62).

[10] B. Auclair, V. Nikonenko, C. Larchet, M. Métayer, L. Dammak. “Correlation between transport parameters of ion-exchange membranes.” In: *Journal of Membrane Science* 195 (2002), pp. 89–102. DOI: 10.1016/S0376-7388(01)00556-7 (cit. on p. 169).

[11] K. Baber, K. Mosthaf, B. Flemisch, R. Helmig, S. Muthing, B. Wohlmuth. “Numerical scheme for coupling two-phase compositional porous-media flow and one-phase compositional free flow.” In: *IMA Journal of Applied Mathematics* 77.6 (July 2012), pp. 887–909. DOI: 10.1093/imamat/hxs048 (cit. on p. 100).

[12] Y. Bachmat, J. Bear. “On the Concept and Size of a Representative Elementary Volume (Rev).” In: *Advances in Transport Phenomena in Porous Media*. Springer Netherlands, 1987. DOI: 10.1007/978-94-009-3625-6 (cit. on p. 44).

[13] J. Baschuk, X. Li. “Modeling of ion and water transport in the polymer electrolyte membrane of PEM fuel cells.” In: *International Journal of Hydrogen Energy* 35.10 (May 2010), pp. 5095–5103. DOI: 10.1016/j.ijhydene.2009.10.032 (cit. on p. 26).

[14] P. Bastian, K. Birken, K. Johannsen, S. Lang, N. Neuß, H. Rentz-Reichert, C. Wieners. “UG - A flexible software toolbox for solving partial differential equations.” In:

Computing and Visualization in Science 1 (1997), pp. 27–40. DOI: 10.1007/s007910050003 (cit. on p. 81).

[15] P. Bastian, M. Blatt, A. Dedner, C. Engwer, R. Klöfkorn, R. Kornhuber, M. Ohlberger, O. Sander. "A generic grid interface for parallel and adaptive scientific computing. Part II: implementation and tests in DUNE." In: *Computing* 82.2-3 (June 2008), pp. 121–138. DOI: 10.1007/s00607-008-0004-9 (cit. on pp. 81, 209).

[16] P. Bastian, M. Blatt, A. Dedner, C. Engwer, R. Klöfkorn, M. Ohlberger, O. Sander. "A generic grid interface for parallel and adaptive scientific computing. Part I: abstract framework." In: *Computing* 82.2-3 (Apr. 2008), pp. 103–119. DOI: 10.1007/s00607-008-0003-x (cit. on pp. 81, 209).

[17] T. Bednarek, G. Tsotridis. "Calculation of effective transport properties of partially saturated gas diffusion layers." In: *Journal of Power Sources* 340 (2017), pp. 111–120. DOI: 10.1016/j.jpowsour.2016.10.098 (cit. on p. 56).

[18] D. M. Bernardi, M. W. Verbrugge. "A Mathematical Model of the Solid-Polymer-Electrolyte Fuel Cell." In: *J. Electrochem. Soc.* 139.9 (1992), pp. 2477–2491. DOI: 10.1149/1.2221251 (cit. on pp. 23, 25).

[19] D. M. Bernardi, M. W. Verbrugge. "Mathematical model of a gas diffusion electrode bonded to a polymer electrolyte." In: *AIChE Journal* 37.8 (Aug. 1991), pp. 1151–1163. DOI: 10.1002/aic.690370805 (cit. on pp. 23, 25).

[20] W. G. Bessler. “Rapid Impedance Modeling via Potential Step and Current Relaxation Simulations.” In: *Journal of The Electrochemical Society* 154.11 (2007), B1186–B1191. DOI: 10.1149/1.2772092 (cit. on p. 102).

[21] B. H. J. Bielski. “Reevaluation of the Spectral and Kinetic Properties of HO2 and O2- Free Radicals.” In: *Photochemistry and Photobiology* 28.4-5 (1978), pp. 645–649. DOI: 10.1111/j.1751-1097.1978.tb06986.x (cit. on p. 171).

[22] R. B. Bird, W. E. Stewart, E. N. Lightfoot. *Transport Phenomena*. 2nd ed. John Wiley & Sons, 2006 (cit. on p. 48).

[23] J. Bockris, S. Srinivasan. *Fuel Cells: Their Electrochemistry*. 1st ed. McGraw-Hill, 1969 (cit. on p. 13).

[24] R. Borup, J. Meyers, B. Pivovar, Y. S. Kim, R. Mukundan, N. Garland, D. Myers, M. Wilson, F. Garzon, D. Wood, P. Zelenay, K. More, K. Stroh, T. Zawodzinski, J. Boncella, J. E. McGrath, M. Inaba, K. Miyatake, M. Hori, K. Ota, Z. Ogumi, S. Miyata, A. Nishikata, Z. Siroma, Y. Uchimoto, K. Yasuda, K.-I. Kimijima, N. Iwashita. “Scientific aspects of polymer electrolyte fuel cell durability and degradation.” In: *Chemical reviews* 107.10 (Oct. 2007), pp. 3904–3951. DOI: 10.1021/cr050182l (cit. on pp. 153, 213).

[25] S. B. Brummer. “The Use of Large Anodic Galvanostatic Transients to Evaluate the Maximum Adsorption on Platinum from Formic Acid Solutions.” In: *The Journal of Physical Chemistry* 69.2 (1965), pp. 562–571. DOI: 10.1021/j100886a034 (cit. on p. 60).

[26] O. Burheim, P. J. S. Vie, J. G. Pharoah, S. Kjelstrup. “Ex situ measurements of through-plane thermal conductivities in a polymer electrolyte fuel cell.” In: *Journal of Power Sources* 195.1 (2010), pp. 249–256. DOI: 10.1016/j.jpowsour.2009.06.077 (cit. on p. 43).

[27] G. V. Buxton, C. L. Greenstock, W. P. Helman, A. B. Ross. “Critical Review of rate constants for reactions of hydrated electrons, hydrogen atoms and hydroxyl radicals ($\cdot$OH/$\cdot O^-$) in Aqueous Solution.” In: *Journal of Physical and Chemical Reference Data* 17.2 (1988), pp. 513–886. DOI: 10.1063/1.555805 (cit. on p. 171).

[28] F. C. Cetinbas, S. G. Advani, A. K. Prasad. “An Improved Agglomerate Model for the PEM Catalyst Layer with Accurate Effective Surface Area Calculation Based on the Sphere-Packing Approach.” In: *Journal of the Electrochemical Society* 161.6 (May 2014), F803–F813. DOI: 10.1149/2.116406jes (cit. on p. 28).

[29] M. Chandesris, R. Vincent, L. Guetaz, J. S. Roch, D. Thoby, M. Quinaud. “Membrane degradation in PEM fuel cells: From experimental results to semi-empirical degradation laws.” In: *International Journal of Hydrogen Energy* 42.12 (2017), pp. 8139–8149. DOI: 10.1016/j.ijhydene.2017.02.116 (cit. on pp. 186, 196, 202).

[30] C. Chen, T. F. Fuller. “The effect of humidity on the degradation of Nafion® membrane.” In: *Polymer Degradation and Stability* 94.9 (Sept. 2009), pp. 1436–1447. DOI: 10.1016/j.polymdegradstab.2009.05.016 (cit. on p. 154).

[31] C. Chen, T. F. Fuller. “XPS Analysis of Polymer Membrane Degradation in PEMFCs.” In: *Journal of The Electrochemical Society* 156.10 (2009), B1218–B1224. DOI: 10.1149/1.3187731 (cit. on pp. 152, 154, 155).

[32] S. Cherevko, G. P. Keeley, S. Geiger, A. R. Zeradjanin, N. Hodnik, N. Kulyk, K. J. Mayrhofer. “Dissolution of Platinum in the Operational Range of Fuel Cells.” In: *ChemElectroChem* 2.10 (2015), pp. 1471–1478. DOI: 10.1002/celc.201500098 (cit. on p. 59).

[33] P. Choi, R. Datta. “Sorption in Proton-Exchange Membranes.” In: *Journal of The Electrochemical Society* 150.12 (2003), E601–E607. DOI: 10.1149/1.1623495 (cit. on pp. 20, 27).

[34] P. Choi, N. H. Jalani, R. Datta. “Thermodynamics and Proton Transport in Nafion I. Membrane Swelling, Sorption, and Ion-Exchange Equilibrium.” In: *Journal of The Electrochemical Society* 152.3 (2005), E84–E89. DOI: 10.1149/1.1855872 (cit. on p. 161).

[35] P. Choi, N. H. Jalani, R. Datta. “Thermodynamics and Proton Transport in Nafion II. Proton Diffusion Mechanisms and Conductivity.” In: *Journal of The Electrochemical Society* 152.3 (2005), E123–E130. DOI: 10.1149/1.1859814 (cit. on pp. 20, 21, 26).

[36] H. Christensen, K. Sehested, H. Corfitzen. “Reactions of Hydroxyl Radicals with Hydrogen Peroxide at Ambient and Elevated Temperatures.” In: *The Journal of Physical Chemistry* 86.9 (1982), pp. 1588–1590. DOI: 10.1021/j100206a023 (cit. on p. 171).

[37] F. D. Coms. “The Chemistry of Fuel Cell Membrane Chemical Degradation.” In: *ECS Transactions* 16.2 (2008), pp. 235–255. DOI: 10.1149/1.2981859 (cit. on pp. 167, 175).

[38] F. D. Coms, H. Liu, J. E. Owejan. “Mitigation of Perfluorosulfonic Acid Membrane Chemical Degradation Using Cerium and Manganese Ions.” In: *ECS Transactions* 16.2 (2008), pp. 1735–1747. DOI: 10.1149/1.2982015 (cit. on pp. 167, 213).

[39] R. Coulon. “Modélisation de la dégradation chimique de membranes dans les piles à combustible à membrane électrolyte polymère.” PhD thesis. Université de Grenoble, 2012. URL: https://tel.archives-ouvertes.fr/tel-00767412/document (cit. on pp. 160, 167, 214).

[40] R. Coulon, W. G. Bessler, A. A. Franco. “Modeling Chemical Degradation of a Polymer Electrolyte Membrane and its Impact on Fuel Cell Performance.” In: *ECS Transactions* 25.35 (2010), pp. 259–273. DOI: 10.1149/1.3414024 (cit. on pp. 160, 214).

[41] D. E. Curtin, R. D. Lousenberg, T. J. Henry, P. C. Tangeman, M. E. Tisack. “Advanced materials for improved PEMFC performance and life.” In: *Journal of Power Sources* 131.1-2 (May 2004), pp. 41–48. DOI: 10.1016/j.jpowsour.2004.01.023 (cit. on pp. 153, 166, 175, 179).

[42] F. S. Dainton, J. Rowbottom. “The Primary Radical Yield in Water. A Comparison of the Photolysis and Radiolysis of Solutions of Hydrogen Peroxide.” In: *Trans. Faraday Soc.* 49.1160 (1953), pp. 1160–1173. DOI: 10.1039/TF9534901160 (cit. on p. 171).

[43] R. M. Darling, J. P. Meyers. “Kinetic Model of Platinum Dissolution in PEMFCs.” In: *Journal of The Electrochemical Society* 150.11 (2003), A1523–A1527. DOI: 10.1149/1.1613669 (cit. on p. 60).

[44] D. A. Deranleau. “General solution of the pseudo first-order rate equations for consecutive reactions with identical rate constants.” In: *Experientia* 38.6 (1982), pp. 661–662. DOI: 10.1007/BF01964078 (cit. on p. 180).

[45] A. M. Dreizler, E. Roduner. “Reaction Kinetics of Hydroxyl Radicals with Model Compounds of Fuel Cell Polymer Membranes.” In: *Fuel Cells* 12.1 (Feb. 2012), pp. 132–140. DOI: 10.1002/fuce.201100157 (cit. on p. 181).

[46] M. Eikerling. “Phenomenological Theory of Electro-osmotic Effect and Water Management in Polymer Electrolyte Proton-Conducting Membranes.” In: *Journal of The Electrochemical Society* 145.8 (1998), pp. 2684–2699. DOI: 10.1149/1.1838700 (cit. on p. 24).

[47] M. Eikerling. “Water Management in Cathode Catalyst Layers of PEM Fuel Cells.” In: *Journal of The Electrochemical Society* 153.3 (2006), E58–E70. DOI: 10.1149/1.2160435 (cit. on p. 48).

[48] M. H. Eikerling, P. Berg. “Poroelectroelastic theory of water sorption and swelling in polymer electrolyte membranes.” In: *Soft Matter* 7.13 (2011), pp. 5976–5990. DOI: 10.1039/c1sm05273j (cit. on pp. 20, 21).

[49] A. Einstein. “Über die von der molekularkinetischensche Theorie der Wärme geforderte Bewegumg von in ruhenden Flüssigkeiten suspendierten Teilchen.” In: *Ann. d. Phys.* 322.8 (1905), pp. 549–560. DOI: 10.1002/andp.19053220806 (cit. on p. 139).

[50] J. M. Fenton, M. P. Rodgers, D. K. Slattery, X. Huang, V. O. Mittal, L. J. Bonville, H. R. Kunz. “Membrane Degradation Mechanisms and Accelerated Durability Testing of Proton Exchange Membrane Fuel Cells.” In: *ECS Transactions* 25.1 (2009), pp. 233–247. DOI: 10.1149/1.3210575 (cit. on p. 154).

[51] J. Fimrite, B. Carnes, H. Struchtrup, N. Djilali. “Transport Phenomena in Polymer Electrolyte Membranes II. Binary Friction Membrane Model.” In: *Journal of The Electrochemical Society* 152.9 (2005), A1815–A1823. DOI: 10.1149/1.1952647 (cit. on p. 26).

[52] J. Fimrite, H. Struchtrup, N. Djilali. “Transport Phenomena in Polymer Electrolyte Membranes I. Modeling Framework.” In: *Journal of The Electrochemical Society* 152.9 (2005), A1804. DOI: 10.1149/1.1952627 (cit. on p. 26).

[53] P. Fischer, J. Heitbaum, W. Vielstich. “Zum Mechanismus der Sauerstoff-Reduktion.” In: *Chemie Ingenieur Technik* 52.5 (1980), pp. 423–425. DOI: 10.1002/cite.330520513 (cit. on p. 13).

[54] B. Flemisch, M. Darcis, K. Erbertseder, B. Faigle, A. Lauser, K. Mosthaf, P. Nuske, A. Tatomir, M. Wolff, R. Helmig. “DuMu^{X} : DUNE for Multi- { Phase , Component , Scale , Physics , ... } Flow and Transport in Porous

Media." In: *Advances in Water Resources* 34.9 (2011), pp. 1102–1112. DOI: 10.1016/j.advwatres.2011.03.007 (cit. on pp. 81, 209).

[55] P. Flory. *Principles of Polymer Chemistry*. Baker lectures 1948. Cornell University Press, 1953 (cit. on p. 27).

[56] A. A. Franco, R. Coulon, R. F. de Morais, S.-K. Cheah, A. Kachmar, M. A. Gabriel. "Multiscale Modeling Prediction of PEMFC MEA Durability under Automotive Conditions." In: *ECS Transactions* 25.1 (2009), pp. 65–79. DOI: 10.1149/1.3210560 (cit. on p. 161).

[57] A. A. Franco, P. Schott, C. Jallut, B. Maschke. "A Multi-Scale Dynamic Mechanistic Model for the Transient Analysis of PEFCs." In: *Fuel Cells* 7.2 (Apr. 2007), pp. 99–117. DOI: 10.1002/fuce.200500204 (cit. on p. 161).

[58] A. A. Franco, P. Schott, C. Jallut, B. Maschke. "A Dynamic Mechanistic Model of an Electrochemical Interface." In: *Journal of The Electrochemical Society* 153.6 (2006), A1053. DOI: 10.1149/1.2188353 (cit. on p. 161).

[59] V. Freger. "Hydration of ionomers and Schroeder's paradox in Nafion." In: *The Journal of Physical Chemistry. B* 113.1 (Jan. 2009), pp. 24–36. DOI: 10.1021/jp806326a (cit. on pp. 19, 22).

[60] E. N. Fuller, P. D. Schettler, J. C. Giddings. "A New Method for Prediction of Binary Gas-Phase Diffusion." In: *Ind. Eng. Chem* 58.5 (1966), pp. 18–27. DOI: 10.1021/ie50677a007 (cit. on p. 48).

[61] T. F. Fuller, J. Newman. “Water and Thermal Management in Solid-Polymer-Electrolyte Fuel Cells.” In: *J. Electrochem. Soc.* 140.5 (1993), pp. 1218–1225. DOI: 10.1149/1.2220960 (cit. on pp. 24, 25).

[62] S. Ge, X. Li, B. Yi, I.-M. Hsing. “Absorption, Desorption, and Transport of Water in Polymer Electrolyte Membranes for Fuel Cells.” In: *Journal of The Electrochemical Society* 152.6 (2005), A1149–A1157. DOI: 10.1149/1.1899263 (cit. on p. 22).

[63] L. Ghassemzadeh, T. J. Peckham, T. Weissbach, X. Luo, S. Holdcroft. “Selective formation of hydrogen and hydroxyl radicals by electron beam irradiation and their reactivity with perfluorosulfonated acid ionomer.” In: *Journal of the American Chemical Society* 135.42 (Oct. 2013), pp. 15923–15932. DOI: 10.1021/ja408032p (cit. on p. 177).

[64] M. Ghelichi, P.-É. A. Melchy, M. H. Eikerling. “Radically coarse-grained approach to the modeling of chemical degradation in fuel cell ionomers.” In: *The journal of physical chemistry. B* 118.38 (Sept. 2014), pp. 11375–11386. DOI: 10.1021/jp506333p (cit. on pp. 156, 172, 178–180).

[65] L. Gubler, S. M. Dockheer, W. H. Koppenol. “Radical ($HO^{\bullet}$, $H^{\bullet}$ and $HOO^{\bullet}$) Formation and Ionomer Degradation in Polymer Electrolyte Fuel Cells.” In: *Journal of The Electrochemical Society* 158.7 (2011), B755–B769. DOI: 10.1149/1.3581040 (cit. on pp. 152–154, 156, 157, 167, 172, 173, 181).

[66] M. Gummalla, V. V. Atrazhev, D. Condit, N. Cipollini, T. Madden, N. Y. Kuzminyh, D. Weiss, S. F. Burlatsky. "Degradation of Polymer-Electrolyte Membranes in Fuel Cells II. Theoretical model." In: *Journal of The Electrochemical Society* 157.11 (2010), B1542. DOI: 10.1149/1.3481450 (cit. on pp. 152, 154, 159).

[67] F. Haber, J. Weiss. "The Catalytic Decomposition of Hydrogen Peroxide by Iron Salts." In: *Proceedings of the Royal Society A: Mathematical, Physical and Engineering Sciences* 147.861 (1934), pp. 332–351. DOI: 10.1098/rspa.1934.0221 (cit. on p. 153).

[68] D. T. Hallinan, M. G. De Angelis, M. Giacinti Baschetti, G. C. Sarti, Y. A. Elabd. "Non-Fickian Diffusion of Water in Nafion." In: *Macromolecules* 43.10 (May 2010), pp. 4667–4678. DOI: 10.1021/ma100047z (cit. on p. 22).

[69] C. H. Hamann, W. Vielstich. *Elektrochemie 2: Elektrodenprozesse, Angewandte Elektrochemie - Taschentext 42*. Verlag Chemie - Physik Verlag, 1981 (cit. on p. 13).

[70] L. Hao, K. Moriyama, W. Gu, C.-Y. Wang. "Modeling and Experimental Validation of Pt Loading and Electrode Composition Effects in PEM Fuel Cells." In: *Journal of the Electrochemical Society* 162.8 (2015), F854–F867. DOI: 10.1149/2.0221508jes (cit. on pp. 30, 64, 65, 68).

[71] L. Hao, K. Moriyama, W. Gu, C.-Y. Wang. "Three Dimensional Computations and Experimental Comparisons for a Large-Scale Proton Exchange Membrane Fuel Cell." In: *Journal of The Electrochemical Society* 163.7 (2016), F744–F751. DOI: 10.1149/2.1461607jes (cit. on p. 213).

[72] C. Hartnig, C. Roth, eds. *Polymer Electrolyte Membrane and Direct Methanol Fuel Cell Technology*. 1st ed. Vol. 1. Woodhead Publishing, 2012 (cit. on p. 161).

[73] D. Harvey, J. G. Pharoah, K. Karan. "A comparison of different approaches to modelling the PEMFC catalyst layer." In: *Journal of Power Sources* 179.1 (2008), pp. 209–219. DOI: 10.1016/j.jpowsour.2007.12.077 (cit. on pp. 28–31, 56, 61, 62).

[74] Q. He, A. Kusoglu, I. T. Lucas, K. Clark, A. Z. Weber, R. Kostecki. "Correlating humidity-dependent ionically conductive surface area with transport phenomena in proton-exchange membranes." In: *Journal of Physical Chemistry B* 115.40 (2011), pp. 11650–11657. DOI: 10.1021/jp206154y (cit. on p. 22).

[75] J. Healy, C. Hayden, T. Xie, K. Olson, R. Waldo, M. Brundage, H. Gasteiger, J. Abbott. "Aspects of the Chemical Degradation of PFSA Ionomers used in PEM Fuel Cells." In: *Fuel Cells* 5.2 (Apr. 2005), pp. 302–308. DOI: 10.1002/fuce.200400050 (cit. on p. 153).

[76] R. Helmig. *Multiphase Flow and Transport Processes in the Subsurface*. Springer-Verlag Berlin Heidelberg, 1997 (cit. on pp. 34, 44, 46).

[77] S. Helmly, B. Ohnmacht, P. Gazdzicki, R. Hiesgen, E. Gülzow, K. A. Friedrich. "Influence of the Distribution of Platinum Deposits on the Properties and Degradation of Platinum-Impregnated Nafion® Membranes." In: *Journal of The Electrochemical Society* 161.14 (2014), F1416–F1426. DOI: 10.1149/05801.0969ecst (cit. on p. 152).

[78] S. Helmly, B. Ohnmacht, R. Hiesgen, E. Gülzow, K. A. Friedrich. "Influence of Platinum Precipitation on Properties and Degradation of Nafion® Membranes S. Helmly." In: *ECS Transactions* 58.1 (2013), pp. 969–990. DOI: 10.1149/05801.0969ecst (cit. on p. 152).

[79] J. P. Hoare. *The Electrochemistry of Oxygen*. Interscience Publishers/John Wiley & Sons Inc., 1968 (cit. on p. 13).

[80] R. Huber, R. Helmig. "Node-centered finite volume discretizations for the numerical simulation of multiphase flow in heterogeneous porous media." In: *Computational Geosciences* 4 (2000), pp. 141–164. DOI: 10.1023/A:1011559916309 (cit. on pp. 87, 100).

[81] IAPWS. *Release on the IAPWS Formulation 2011 for the Thermal Conductivity of Ordinary Water Substance*. Tech. rep. IAPWS, 2011. URL: http://www.iapws.org/relguide/ThCond.pdf (cit. on p. 55).

[82] IPCC 2007 Core Writing Team. *Climate Change 2007: Synthesis Report. Contribution of Working Groups I, II and III to the Fourth Assessment Report of the Intergovernmental Panel on Climate Change*. 2007, 104 pp. URL: https://www.ipcc.ch/report/ar4/syr/ (cit. on p. 2).

[83] IPCC 2014 Core Writing Team. *Climate Change 2014: Synthesis Report. Contribution of Working Groups I, II and III to the Fifth Assessment Report of the Intergovernmental Panel on Climate Change*. 2014, 151 pp. URL: https://www.ipcc.ch/report/ar5/syr/ (cit. on pp. 1, 3, 4).

[84] T. Ishimoto, T. Ogura, M. Koyama. “Theoretical Study on Chemical Degradation Mechanism of Nafion Side Chain by the Attack of OH Radical in Polymer Electrolyte Fuel Cell.” In: *ECS Transactions* 35.27 (2011), pp. 1–6. DOI: 10.1149/1.3643346 (cit. on p. 154).

[85] T. Ishimoto, R. Nagumo, T. Ogura, T. Ishihara, B. Kim, A. Miyamoto, M. Koyama. “Chemical Degradation Mechanism of Model Compound, $CF_3(CF_2)_3O(CF_2)_2OCF_2SO_3H$, of PFSA Polymer by Attack of Hydroxyl Radical in PEMFCs.” In: *Journal of The Electrochemical Society* 157.9 (2010), B1305–B1309. DOI: 10.1149/1.3462970 (cit. on p. 154).

[86] T. Jacobsen, P. V. Hendriksen, S. Koch. “Diffusion and conversion impedance in solid oxide fuel cells.” In: *Electrochimica Acta* 53.25 (2008), pp. 7500–7508. DOI: 10.1016/j.electacta.2008.02.019 (cit. on p. 144).

[87] T. Jahnke, G. Futter, A. Latz, T. Malkow, G. Papakonstantinou, G. Tsotridis, P. Schott, M. Gérard, M. Quinaud, M. Quiroga, A. A. Franco, K. Malek, F. Calle-Vallejo, R. Ferreira De Morais, T. Kerber, P. Sautet, D. Loffreda, S. Strahl, M. Serra, P. Polverino, C. Pianese, M. Mayur, W. G. Bessler, C. Kompis. “Performance and degradation of Proton Exchange Membrane Fuel Cells: State of the art in modeling from atomistic to system scale.” In: *Journal of Power Sources* 304 (2016), pp. 207–233. DOI: 10.1016/j.jpowsour.2015.11.041 (cit. on pp. 17, 18, 31, 152).

[88] G. J. M. Janssen. “A Phenomenological Model of Water Transport in a Proton Exchange Membrane Fuel Cell.”

In: *Journal of The Electrochemical Society* 148.12 (2001), A1313–A1323. DOI: 10.1149/1.1415031 (cit. on p. 25).

[89] G. G. Jayson, B. J. Parsons, A. J. Swallow. "Oxidation of ferrous ions by perhydroxyl radicals." In: *Journal of the Chemical Society, Faraday Transactions 1* 69.3 (1973), pp. 236–242. DOI: 10.1039/f19736900236 (cit. on p. 171).

[90] S. Jeck, P. Scharfer, M. Kind. "Absence of Schroeder's paradox: Experimental evidence for water-swollen Nafion membranes." In: *Journal of Membrane Science* 373 (2011), pp. 74–79. DOI: 10.1016/j.memsci.2011.02.036 (cit. on p. 19).

[91] S. Jomori, K. Komatsubara, N. Nonoyama, M. Kato, T. Yoshida. "An Experimental Study of the Effects of Operational History on Activity Changes in a PEMFC." In: *Journal of the Electrochemical Society* 160.9 (2013), F1067–F1073. DOI: 10.1149/2.103309jes (cit. on p. 66).

[92] S. Jomori, N. Nonoyama, T. Yoshida. "Analysis and modeling of PEMFC degradation: Effect on oxygen transport." In: *Journal of Power Sources* 215 (Oct. 2012), pp. 18–27. DOI: 10.1016/j.jpowsour.2012.04.069 (cit. on pp. 31, 59, 64).

[93] H. Ju. "Investigation of the effects of the anisotropy of gas-diffusion layers on heat and water transport in polymer electrolyte fuel cells." In: *Journal of Power Sources* 191.2 (2009), pp. 259–268. DOI: 10.1016/j.jpowsour.2009.01.103 (cit. on p. 56).

[94] A. El-Kharouf, T. J. Mason, D. J. L. Brett, B. G. Pollet. "Ex-situ characterisation of gas diffusion layers for proton exchange membrane fuel cells." In: *Journal of Power Sources* 218 (2012), pp. 393–404. DOI: 10.1016/j.jpowsour.2012.06.099 (cit. on p. 122).

[95] W. H. Koppenol, J. Butler, J. W. v. Leeuwen. "The Haber-Weiss Cycle." In: *Photochemistry and Photobiology* 28.4-5 (1978), pp. 655–658. DOI: 10.1111/j.1751-1097.1978.tb06989.x (cit. on p. 171).

[96] K.-D. Kreuer. "The role of internal pressure for the hydration and transport properties of ionomers and polyelectrolytes." In: *Solid State Ionics* 252 (Dec. 2013), pp. 93–101. DOI: 10.1016/j.ssi.2013.04.018 (cit. on pp. 19, 21).

[97] K. Kudo, R. Jinnouchi, Y. Morimoto. "Humidity and Temperature Dependences of Oxygen Transport Resistance of Nafion Thin Film on Platinum Electrode." In: *Electrochimica Acta* 209 (2016), pp. 682–690. DOI: 10.1016/j.electacta.2016.04.023 (cit. on p. 29).

[98] A. Kulikovsky. "How important is oxygen transport in agglomerates in a PEM fuel cell catalyst layer?" In: *Electrochimica Acta* 130 (June 2014), pp. 826–829. DOI: 10.1016/j.electacta.2014.03.131 (cit. on p. 29).

[99] S. Kundu, M. W. Fowler, L. C. Simon, R. Abouatallah, N. Beydokhti. "Degradation analysis and modeling of reinforced catalyst coated membranes operated under OCV conditions." In: *Journal of Power Sources* 183.2 (Sept. 2008), pp. 619–628. DOI: 10.1016/j.jpowsour.2008.05.074 (cit. on pp. 152, 157).

[100] A. Kusoglu, A. Kwong, K. T. Clark, H. P. Gunterman, A. Z. Weber. "Water Uptake of Fuel-Cell Catalyst Layers." In: *Journal of the Electrochemical Society* 159.9 (Aug. 2012), F530–F535. DOI: 10.1149/2.031209jes (cit. on p. 51).

[101] M. J. Lampinen, M. Fomino. "Analysis of Free Energy and Entropy Changes for Half-Cell Reactions." In: *Journal of The Electrochemical Society* 140.12 (1993), pp. 3537–3546. DOI: 10.1149/1.2221123 (cit. on p. 70).

[102] A. Lauser, C. Hager, R. Helmig, B. Wohlmuth. "A new approach for phase transitions in miscible multi-phase flow in porous media." In: *Advances in Water Resources* 34 (2011), pp. 957–966. DOI: 10.1016/j.advwatres.2011.04.021 (cit. on pp. 45, 49, 54).

[103] C. Lee, J. Yoon. "Temperature dependence of hydroxyl radical formation in the $h\nu$/Fe^{3+}/H_2O_2 and Fe^{3+}/H_2O_2 systems." In: *Chemosphere* 56.10 (2004), pp. 923–934. DOI: 10.1016/j.chemosphere.2004.04.047 (cit. on p. 171).

[104] M. C. Leverett. "Capillary Behavior in Porous Solids." In: *Transactions of the AIME* (1941). DOI: 10.2118/941152-G (cit. on p. 47).

[105] G. C. Li, P. G. Pickup. "Ionic conductivity of PEMFC electrodes - Effect of Nafion loading." In: *Journal of the Electrochemical Society* 150.11 (2003), pp. C745–C752. DOI: 10.1149/1.1611493 (cit. on p. 123).

[106] X. S. Li. “An Overview of SuperLU: Algorithms, Implementation, and User Interface.” In: 31.3 (Sept. 2005), pp. 302–325. URL: http://crd-legacy.lbl.gov/~xiaoye/LBNL-53848.pdf (cit. on p. 82).

[107] X. Li, J. Demmel, J. Gilbert, iL. Grigori, M. Shao, I. Yamazaki. *SuperLU Users' Guide*. Tech. rep. LBNL-44289. Lawrence Berkeley National Laboratory, Sept. 1999. URL: http://crd.lbl.gov/~xiaoye/SuperLU/ (cit. on p. 82).

[108] C. Lim, L. Ghassemzadeh, F. Van Hove, M. Lauritzen, J. Kolodziej, G. Wang, S. Holdcroft, E. Kjeang. “Membrane degradation during combined chemical and mechanical accelerated stress testing of PEM fuel cells.” In: *Journal of Power Sources* 257 (Feb. 2014), pp. 102–110. DOI: 10.1016/j.jpowsour.2014.01.106 (cit. on p. 162).

[109] H. Liu, W. K. Epting, S. Litster. “Gas Transport Resistance in Polymer Electrolyte Thin Films on Oxygen Reduction Reaction Catalysts.” In: *Langmuir* 31.36 (2015), pp. 9853–9858. DOI: 10.1021/acs.langmuir.5b02487 (cit. on p. 29).

[110] W. Liu, D. Zuckerbrod. “In Situ Detection of Hydrogen Peroxide in PEM Fuel Cells.” In: *Journal of The Electrochemical Society* 152.6 (2005), A1165–A1170. DOI: 10.1149/1.1904988 (cit. on pp. 152, 153).

[111] Y. Liu, M. Mathias, J. Zhang. “Measurement of Platinum Oxide Coverage in a Proton Exchange Membrane Fuel Cell.” In: *Electrochemical and Solid-State Letters* 13 (2010), B1–B3. DOI: 10.1149/1.3257595 (cit. on p. 59).

[112] T. Lundström, H. Christensen, K. Sehested. "Reactions of the HO_2 radical with OH, H, Fe^{2+} and Cu^{2+} at elevated temperatures." In: *Radiation Physics and Chemistry* 69.3 (2004), pp. 211–216. DOI: 10.1016/S0969-806X(03)00462-6 (cit. on p. 171).

[113] T. Lundström, H. Christensen, K. Sehested. "The reaction of hydrogen atoms with hydrogen peroxide as a function of temperature." In: *Radiation Physics and Chemistry* 61.2 (2001), pp. 109–113. DOI: 10.1016/S0969-806X(01)00189-X (cit. on p. 171).

[114] N. Macauley, L. Ghassemzadeh, C. Lim, M. Watson, J. Kolodziej, M. Lauritzen, S. Holdcroft, E. Kjeang. "Pt Band Formation Enhances the Stability of Fuel Cell Membranes." In: *ECS Electrochemistry Letters* 2.4 (Feb. 2013), F33–F35. DOI: 10.1149/2.007304eel (cit. on p. 152).

[115] T. Madden, D. Weiss, N. Cipollini, D. Condit, M. Gummalla, S. Burlatsky, V. Atrazhev. "Degradation of Polymer-Electrolyte Membranes in Fuel Cells I. Experimental." In: *Journal of The Electrochemical Society* 156.5 (2009), B657–B662. DOI: 10.1149/1.3095466 (cit. on pp. 159, 160).

[116] P. W. Majsztrik, M. B. Satterfield, A. B. Bocarsly, J. B. Benziger. "Water sorption, desorption and transport in Nafion membranes." In: *Journal of Membrane Science* 301.1-2 (Sept. 2007), pp. 93–106. DOI: 10.1016/j.memsci.2007.06.022 (cit. on pp. 19, 22).

[117] S. L. Manatt, M. R. R. Manatt. "On the analyses of mixture vapor pressure data: the hydrogen peroxide/water system and its excess thermodynamic functions."

In: *Chemistry (Weinheim an der Bergstrasse, Germany)* 10.24 (Dec. 2004), pp. 6540–57. DOI: 10.1002/chem.200400104 (cit. on p. 165).

[118] M. Markiewicz, C. Zalitis, A. Kucernak. "Performance measurements and modelling of the ORR on fuel cell electrocatalysts - The modified double trap model." In: *Electrochimica Acta* 179 (2015), pp. 126–136. DOI: 10.1016/j.electacta.2015.04.066 (cit. on pp. 32, 63).

[119] E. Mason, A. Malinauskas. *Gas transport in porous media: the dusty-gas model*. Chemical engineering monographs Bd. 17. Elsevier, 1983 (cit. on p. 25).

[120] B. J. McBride, M. J. Zehe, S. Gordon. *NASA Glenn Coefficients for Calculating Thermodynamic Properties of Individual Species*. Tech. rep. 2002. URL: https://www.grc.nasa.gov/WWW/CEAWeb/TP-2002-211556.pdf (cit. on p. 71).

[121] J. P. Meyers, J. Newman. "Simulation of the Direct Methanol Fuel Cell I. Themodynamic Framework for a Multicomponent Membrane." In: *Journal of The Electrochemical Society* 149.6 (2002), A710–A717. DOI: 10.1149/1.1473188 (cit. on pp. 36, 37).

[122] M. Moein-Jahromi, M. Kermani. "Performance prediction of PEM fuel cell cathode catalyst layer using agglomerate model." In: *International Journal of Hydrogen Energy* 37.23 (Dec. 2012), pp. 17954–17966. DOI: 10.1016/j.ijhydene.2012.09.120 (cit. on p. 28).

[123] M. Moore, A. Putz, M. Secanell. “Investigation of the ORR Using the Double-Trap Intrinsic Kinetic Model.” In: *Journal of the Electrochemical Society* 160.6 (2013), F670–F681. DOI: 10.1149/2.123306jes (cit. on pp. 32, 63).

[124] M. J. Moran, H. N. Shapiro. *Fundamentals of Engineering Thermodynamics*. John Wiley & Sons, 1996 (cit. on p. 26).

[125] T. Morawietz, M. Handl, C. Oldani, K. A. Friedrich, R. Hiesgen. “Quantitative in Situ Analysis of Ionomer Structure in Fuel Cell Catalytic Layers.” In: *ACS Applied Materials and Interfaces* 8.40 (2016), pp. 27044–27054. DOI: 10.1021/acsami.6b07188 (cit. on pp. 30, 67).

[126] S. Müthing. “A Flexible Framework for Multi Physics and Multi Domain PDE Simulations.” PhD thesis. University of Stuttgart, 2015. DOI: 10.18419/opus-3620 (cit. on pp. 82, 94, 213).

[127] S. Müthing, P. Bastian. “Dune-Multidomaingrid: A Metagrid Approach to Subdomain Modeling.” In: *Advances in DUNE*. Springer-Verlag Berlin Heidelberg, 2012, pp. 59–73. DOI: 10.1007/978-3-642-28589-9 (cit. on pp. 82, 94, 213).

[128] J. Newman, K. E. Thomas-Alyea. *Electrochemical Systems*. 3rd ed. John Wiley & Sons, 2004 (cit. on pp. 23, 38, 40, 42).

[129] K. C. Neyerlin, W. Gu, J. Jorne, H. A. Gasteiger. “Determination of Catalyst Unique Parameters for the Oxygen Reduction Reaction in a PEMFC.” In: *Journal of The Elec-*

trochemical Society 153.10 (2006), A1955–A1963. DOI: 10.1149/1.2266294 (cit. on pp. 31, 62).

[130] K. C. Neyerlin, W. Gu, J. Jorne, H. A. Gasteiger. "Study of the Exchange Current Density for the Hydrogen Oxidation and Evolution Reactions." In: *Journal of The Electrochemical Society* 154 (2007), B631–B635. DOI: 10.1149/1.2733987 (cit. on pp. 57, 123).

[131] R. O'Hayre, S.-W. Cha, W. Colella, F. B. Prinz. *Fuel Cell Fundamentals*. 2nd ed. John Wiley & Sons, 2009 (cit. on pp. 10, 11, 14).

[132] N. Ohguri, A. Y. Nosaka, Y. Nosaka. "Detection of OH radicals as the effect of Pt particles in the membrane of polymer electrolyte fuel cells." In: *Journal of Power Sources* 195.15 (Aug. 2010), pp. 4647–4652. DOI: 10.1016/j.jpowsour.2010.02.010 (cit. on p. 152).

[133] A. Ohma, S. Yamamoto, K. Shinohara. "Membrane degradation mechanism during open-circuit voltage hold test." In: *Journal of Power Sources* 182.1 (July 2008), pp. 39–47. DOI: 10.1016/j.jpowsour.2008.03.078 (cit. on p. 152).

[134] M. Okumura, Z. Noda, J. Matsuda, Y. Tachikawa, M. Nishihara, S. M. Lyth, A. Hayashi, K. Sasaki. "Correlating Cathode Microstructure with PEFC Performance Using FIB-SEM and TEM." In: *Journal of The Electrochemical Society* 164.9 (2017), F928–F934. DOI: 10.1149/2.0581709jes (cit. on p. 30).

[135] L. M. Onishi, J. M. Prausnitz, J. Newman. “Water-Nafion equilibria. absence of Schroeder’s paradox.” In: *The Journal of Physical Chemistry. B* 111.34 (Aug. 2007), pp. 10166–10173. DOI: 10.1021/jp073242v (cit. on p. 19).

[136] J. P. Owejan, J. E. Owejan, W. Gu. “Impact of Platinum Loading and Catalyst Layer Structure on PEMFC Performance.” In: *Journal of the Electrochemical Society* 160.8 (2013), F824–F833. DOI: 10.1149/2.072308jes (cit. on p. 29).

[137] A. Parthasarathy. “Pressure Dependence of the Oxygen Reduction Reaction at the Platinum Microelectrode/-Nafion Interface: Electrode Kinetics and Mass Transport.” In: *Journal of The Electrochemical Society* 139.10 (1992), pp. 2856–2862. DOI: 10.1149/1.2068992 (cit. on p. 13).

[138] A. Parthasarathy, B. Davé, S. Srinivasan, A. J. Appleby, C. R. Martin. “The Platinum Microelectrode/Nafion Interface: An Electrochemical Impedance Spectroscopic Analysis of Oxygen Reduction Kinetics and Nation Characteristics.” In: *Journal of The Electrochemical Society* 139.6 (1992), pp. 1634–1641. DOI: 10.1149/1.2069469 (cit. on pp. 31, 62).

[139] A. Parthasarathy, C. R. Martin, S. Srinivasan. “Investigations of the O_2 Reduction Reaction at the Platinum/Nafion® Interface Using a Solid-State Electrochemical Cell.” In: *Journal of The Electrochemical Society* 138.4 (1991), pp. 916–921. DOI: 10.1149/1.2085747 (cit. on pp. 31, 59, 61).

[140] A. Parthasarathy, S. Srinivasan, A. J. Appleby, C. R. Martin. “Temperature dependence of the electrode kinetics of oxygen reduction at the platinum/Nafion interface - A microelectrode investigation.” In: *Journal of The Electrochemical Society* 139.9 (1992), pp. 2530–2537. DOI: 10.1149/1.2221258 (cit. on p. 123).

[141] D. K. Paul, R. McCreery, K. Karan. “Proton Transport Property in Supported Nafion Nanothin Films by Electrochemical Impedance Spectroscopy.” In: *Journal of the Electrochemical Society* 161.14 (2014), F1395–F1402. DOI: 10.1149/2.0571414jes (cit. on p. 51).

[142] B. P. Pearman. “The Behavior of Cerium Oxide Nanoparticles in Polymer Electrolyte Membranes in ex-situ and in-situ Fuel Cell Durability Tests.” PhD thesis. University of Bath, 2012. URL: http://stars.library.ucf.edu/cgi/viewcontent.cgi?article=3302&context=etd (cit. on p. 213).

[143] M. C. Pelsozy. “Investigation of hydrogen peroxide production and transport in a proton exchange membrane fuel cell and the atom resolved micro-characterization of its catalyst.” PhD thesis. 2008. URL: http://rave.ohiolink.edu/etdc/view?acc_num=case1209692060 (cit. on p. 166).

[144] R. Petrone, Z. Zheng, D. Hissel, M. C. Péra, C. Pianese, M. Sorrentino, M. Becherif, N. Yousfi-Steiner. “A review on model-based diagnosis methodologies for PEMFCs.” In: *International Journal of Hydrogen Energy* 38.17 (2013), pp. 7077–7091. DOI: 10.1016/j.ijhydene.2013.03.106 (cit. on p. 129).

[145] I. Pivac, F. Barbir. “Inductive phenomena at low frequencies in impedance spectra of proton exchange membrane fuel cells – A review.” In: *Journal of Power Sources* 326 (2016), pp. 112–119. DOI: 10.1016/j.jpowsour.2016.06.119 (cit. on pp. 129–132).

[146] J. J. Pods. “Electrodiffusion Models of Axon and Extracellular Space Using the Poisson-Nernst-Planck Equations.” PhD thesis. 2014. DOI: 10.11588/heidok.00017128 (cit. on p. 213).

[147] J. Pods, J. Schönke, P. Bastian. “Electrodiffusion models of neurons and extracellular space using the poisson-nernst-planck equations - Numerical simulation of the intra- and extracellular potential for an axon model.” In: *Biophysical Journal* 105.1 (2013), pp. 242–254. DOI: 10.1016/j.bpj.2013.05.041 (cit. on p. 213).

[148] A. Pozio, R. Silva, M. De Francesco, L. Giorgi. “Nafion degradation in PEFCs from end plate iron contamination.” In: *Electrochimica Acta* 48.11 (May 2003), pp. 1543–1549. DOI: 10.1016/S0013-4686(03)00026-4 (cit. on p. 166).

[149] S. Primdahl. “Gas Conversion Impedance: A Test Geometry Effect in Characterization of Solid Oxide Fuel Cell Anodes.” In: *Journal of The Electrochemical Society* 145.7 (1998), p. 2431. DOI: 10.1149/1.1838654 (cit. on p. 144).

[150] S. M. Rezaei Niya, M. Hoorfar. “Study of proton exchange membrane fuel cells using electrochemical impedance spectroscopy technique - A review.” In: *Journal of Power*

Sources 240 (2013), pp. 281–293. DOI: 10.1016/j.jpowsour.2013.04.011 (cit. on p. 129).

[151] T. Rigg, W. Taylor, J. Weiss. "The rate constant of the bimolecular reaction between hydrogen peroxide and ferrous ion." In: *The Journal of Chemical Physics* 22.4 (1954), pp. 575–577. DOI: 10.1063/1.1740127 (cit. on p. 171).

[152] S. Risse, N. A. Cañas, N. Wagner, E. Härk, M. Ballauff, K. A. Friedrich. "Correlation of capacity fading processes and electrochemical impedance spectra in lithium/sulfur cells." In: *Journal of Power Sources* 323 (2016), pp. 107–114. DOI: 10.1016/j.jpowsour.2016.05.032 (cit. on p. 212).

[153] M. P. Rodgers, B. P. Pearman, L. J. Bonville, D. A. Cullen, N. Mohajeri, D. K. Slattery. "Evaluation of the Effect of Impregnated Platinum on PFSA Degradation for PEM Fuel Cells." In: *Journal of the Electrochemical Society* 160.10 (2013), F1123–F1128. DOI: 10.1149/2.055310jes (cit. on p. 152).

[154] M. P. Rodgers, L. J. Bonville, D. K. Slattery. "Evaluation of the Durability of Polymer Electrolyte Membranes in Fuel Cells Containing Pt/C and Pt–Co/C Catalysts Under Accelerated Testing." In: *ECS Transactions* 41.1 (2011), pp. 1461–1469. DOI: 10.1149/1.3635677 (cit. on p. 152).

[155] T. Romero, W. Mérida. "Water transport in liquid and vapour equilibrated Nafion™ membranes." In: *Journal of Membrane Science* 338.1-2 (2009), pp. 135–144. DOI: 10.1016/j.memsci.2009.04.018 (cit. on p. 22).

[156] T. Rosén, J. Eller, J. Kang, N. I. Prasianakis, J. Mantzaras, F. N. Büchi. "Saturation Dependent Effective Transport Properties of PEFC Gas Diffusion Layers." In: *Journal of the Electrochemical Society* 159.9 (2012), F536–F544. DOI: 10.1149/2.005209jes (cit. on p. 46).

[157] S. K. Roy, M. E. Orazem, B. Tribollet. "Interpretation of Low-Frequency Inductive Loops in PEM Fuel Cells." In: *Journal of The Electrochemical Society* 154.12 (2007), B1378–B1388. DOI: 10.1149/1.2789377 (cit. on p. 132).

[158] J. D. Rush, B. H. J. Bielski. "Pulse radiolysis studies of alkaline iron(III) and iron(VI) solutions. Observation of transient iron complexes with intermediate oxidation states." In: *The Journal of Physical Chemistry* 89.23 (1985), pp. 5062–5066. DOI: 10.1021/ja00263a037 (cit. on p. 171).

[159] R. Sander. *Compilation of Henry's Law Constants for Inorganic and Organic Species of Potential Importance in Environmental Chemistry*. Tech. rep. 1999. URL: http://www.henrys-law.org/henry-3.0.pdf (cit. on p. 164).

[160] M. B. Satterfield, J. B. Benziger. "Non-Fickian Water Vapor Sorption Dynamics by Nafion Membranes." In: *Journal of Physical Chemistry B* 112 (2008), pp. 3693–3704. DOI: 10.1021/jp7103243 (cit. on p. 22).

[161] A. E. Scheidegger. *The physics of flow through porous media*. University of Toronto Press, 1974 (cit. on p. 46).

[162] R. Schlögl, U. Schödel. "Über das Verhalten geladener Porenmembranen bei Stromdurchgang." In: *Zeitschrift*

für Physikalische Chemie (1955), pp. 372–397. DOI: 10.1524/zpch.1955.5.5_6.372 (cit. on pp. 23, 26).

[163] J. P. Schmidt, E. Ivers-Tiffée. "Pulse-fitting - A novel method for the evaluation of pulse measurements, demonstrated for the low frequency behavior of lithium-ion cells." In: *Journal of Power Sources* 315 (2016), pp. 316–323. DOI: 10.1016/j.jpowsour.2016.03.026 (cit. on p. 212).

[164] P. von Schroeder. *Über Erstarrungs- und Quellungserscheinungen von Gelatine*. W. Engelmann, 1903 (cit. on pp. 18, 25).

[165] M. Secanell, K. Karan, A. Suleman, N. Djilali. "Multivariable optimization of PEMFC cathodes using an agglomerate model." In: *Electrochimica Acta* 52.22 (2007), pp. 6318–6337. DOI: 10.1016/j.electacta.2007.04.028 (cit. on p. 28).

[166] V. A. Sethuraman, J. W. Weidner, A. T. Haug, S. Motupally, L. V. Protsailo. "Hydrogen Peroxide Formation Rates in a PEMFC Anode and Cathode." In: *Journal of The Electrochemical Society* 155.1 (2008), B50–B57. DOI: 10.1149/1.2801980 (cit. on pp. 153, 163).

[167] B. P. Setzler, T. F. Fuller. "A Physics-Based Impedance Model of Proton Exchange Membrane Fuel Cells Exhibiting Low-Frequency Inductive Loops." In: *Journal of the Electrochemical Society* 162.6 (2015), F519–F530. DOI: 10.1149/2.0361506jes (cit. on pp. 51, 132).

[168] A. A. Shah, T. R. Ralph, F. C. Walsh. "Modeling and Simulation of the Degradation of Perfluorinated Ion-Exchange Membranes in PEM Fuel Cells." In: *Journal of The Electrochemical Society* 156.4 (2009), B465–B484. DOI: 10.1149/1.3077573 (cit. on pp. 28, 152–154, 158, 167, 176).

[169] T. J. Silverman, J. P. Meyers, J. J. Beaman. "Dynamic thermal, transport and mechanical model of fuel cell membrane swelling." In: *Fuel Cells* 11.6 (2011), pp. 875–887. DOI: 10.1002/fuce.201100025 (cit. on p. 22).

[170] T. J. Silverman, J. P. Meyers, J. J. Beaman. "Modeling Water Transport and Swelling in Polymer Electrolyte Membranes." In: *Journal of The Electrochemical Society* 157.10 (2010), B1376–B1381. DOI: 10.1149/1.3464805 (cit. on p. 22).

[171] M. Smoluchowski. "Zur kinetischen Theorie der Brownschen Molekularbewegung und der Suspensionen." In: *Ann. d. Phys.* 326.14 (1906), pp. 756–780. DOI: 10.1002/andp.19063261405 (cit. on p. 139).

[172] W. Somerton, J. Keese, S. Chu. "Thermal Behavior of Unconsolidated Oil Sands." In: *Society of Petroleum Engineers Journal* (1974). DOI: 10.2118/4506-PA (cit. on p. 55).

[173] N. E. Souza, J. L. Bott-Neto, T. A. Rocha, G. C. da Silva, E. Teixeira-Neto, E. R. Gonzalez, E. A. Ticianelli. "Support modification in Pt/C electrocatalysts for durability increase: A degradation study assisted by identical location transmission electron microscopy." In: *Electrochim-*

ica Acta 265 (2018), pp. 523–531. DOI: 10.1016/j.electacta.2018.01.180 (cit. on p. 30).

[174] T. E. Springer, T. A. Zawodzinski, S. Gottesfeld. "Polymer Electrolyte Fuel Cell Model." In: *J. Electrochem. Soc.* 138.8 (1991), pp. 2334–2342. DOI: 10.1149/1.2085971 (cit. on pp. 23, 25, 39).

[175] W. Sun, B. A. Peppley, K. Karan. "An improved two-dimensional agglomerate cathode model to study the influence of catalyst layer structural parameters." In: *Electrochimica Acta* 50.16-17 (2005), pp. 3359–3374. DOI: 10.1016/j.electacta.2004.12.009 (cit. on pp. 28, 29, 31, 56, 61, 67).

[176] T. Thampan, S. Malhotra, H. Tang, R. Datta. "Modeling of Conductive Transport in Proton-Exchange Membranes for Fuel Cells." In: *Journal of The Electrochemical Society* 147.9 (2000), pp. 3242–3250. DOI: 10.1149/1.1393890 (cit. on p. 25).

[177] A. A. Topalov, S. Cherevko, A. R. Zeradjanin, J. C. Meier, I. Katsounaros, K. J. J. Mayrhofer. "Towards a comprehensive understanding of platinum dissolution in acidic media." In: *Chemical Science* 5 (2014), pp. 631–638. DOI: 10.1039/c3sc52411f (cit. on p. 59).

[178] C. Vallieres, D. Winkelmann, D. Roizard, E. Favre, P. Scharfer, M. Kind. "On Schroeder's paradox." In: *Journal of Membrane Science* 278.1-2 (2006), pp. 357–364. DOI: 10.1016/j.memsci.2005.11.020 (cit. on pp. 18, 19).

[179] S. A. Vilekar, R. Datta. “The effect of hydrogen crossover on open-circuit voltage in polymer electrolyte membrane fuel cells.” In: *Journal of Power Sources* 195.8 (Apr. 2010), pp. 2241–2247. DOI: 10.1016/j.jpowsour.2009.10.023 (cit. on pp. 13, 101).

[180] W. Vogel, L. Lundquist, P. Ross, P. Stonehart. “Reaction pathways and poisons-II. The rate controlling step for electrochemical oxidation of hydrogen on Pt in acid and poisoning of the reaction by CO.” In: *Electrochimica Acta* 20.1 (1975), pp. 79–93. DOI: 10.1016/0013-4686(75)85048-1 (cit. on p. 31).

[181] C. Walling, A. Goosen. “Mechanism of the Ferric Ion Catalyzed Decomposition of Hydrogen Peroxide. Effect of Organic Substrates.” In: *Journal of the American Chemical Society* 95.9 (1973), pp. 2987–2991. DOI: 10.1021/ja00790a042 (cit. on p. 171).

[182] J. X. Wang, T. E. Springer, R. R. Adzic. “Dual-Pathway Kinetic Equation for the Hydrogen Oxidation Reaction on Pt Electrodes.” In: *Journal of The Electrochemical Society* 153.9 (2006), A1732–A1740. DOI: 10.1149/1.2218756 (cit. on p. 31).

[183] J. X. Wang, F. A. Uribe, T. E. Springer, J. Zhang, R. R. Adzic. “Intrinsic kinetic equation for oxygen reduction reaction in acidic media: the double Tafel slope and fuel cell applications.” In: *Faraday Discuss.* 140 (2008), pp. 347–362. DOI: 10.1039/B814058H (cit. on pp. 32, 63).

[184] J. X. Wang, J. Zhang, R. R. Adzic. "Double-Trap Kinetic Equation for the Oxygen Reduction Reaction on Pt(111) in Acidic Media." In: *Journal of Physical Chemistry A* 111 (2007), pp. 12702–12710. DOI: 10.1021/jp076104e (cit. on pp. 32, 59, 63).

[185] Y. Wang, C.-Y. Wang. "A Nonisothermal, Two-Phase Model for Polymer Electrolyte Fuel Cells." In: *Journal of The Electrochemical Society* 153.6 (2006), A1193–A1200. DOI: 10.1149/1.2193403 (cit. on p. 213).

[186] A. Z. Weber, R. L. Borup, R. M. Darling, P. K. Das, T. J. Dursch, W. Gu, D. Harvey, A. Kusoglu, S. Litster, M. M. Mench, R. Mukundan, J. P. Owejan, J. G. Pharoah, M. Secanell, I. V. Zenyuk. "A Critical Review of Modeling Transport Phenomena in Polymer-Electrolyte Fuel Cells." In: *Journal of the Electrochemical Society* 161.12 (Sept. 2014), F1254–F1299. DOI: 10.1149/2.0751412jes (cit. on pp. 17, 30, 32, 70).

[187] A. Z. Weber, J. Newman. "Transport in Polymer-Electrolyte Membranes I. Physical model." In: *Journal of The Electrochemical Society* 150.7 (2003), A1008–A1015. DOI: 10.1149/1.1580822 (cit. on pp. 25, 72).

[188] A. Z. Weber, J. Newman. "Transport in Polymer-Electrolyte Membranes II. Mathematical Model." In: *Journal of The Electrochemical Society* 151.2 (2004), A311–A325. DOI: 10.1149/1.1639157 (cit. on pp. 37–42).

[189] A. Z. Weber, J. Newman. "Transport in Polymer-Electrolyte Membranes III.Model Validation in a Simple

Fuel-Cell Model." In: *Journal of The Electrochemical Society* 151.2 (2004), A326–A339. DOI: 10.1149/1.1639158 (cit. on p. 25).

[190] F. M. White. *Fluid Mechanics*. 5th ed. McGraw-Hill, 2002 (cit. on p. 34).

[191] D. O. Whittemore, D. Langmuir. "Standard Electrode Potential of $Fe^{3+} + e^{-} = Fe^{2+}$ from 5-35°C." In: *Journal of Chemical Engineering Data* 17.3 (1972), pp. 288–290. DOI: 10.1021/je60054a002 (cit. on p. 167).

[192] H. Wiese, K. G. Weil. "An Efficient Fourier Transform Algorithm for Frequency Domains of Several Decades Using Logarithmically Spaced Time Samples." In: *IEEE Transactions on Acoustics, Speech and Signal Processing* 36.7 (1988), pp. 1096–1099. DOI: 10.1109/29.1636 (cit. on p. 103).

[193] M. Wöhr. "Instationäres thermodynamisches Verhalten der Polymermembran-Brennstoffzelle." In: *Fortschritt-Berichte VDI, Reihe 3: Verfahrenstechnik*. VDI Verlag GmbH, 2000 (cit. on p. 12).

[194] K. H. Wong, E. Kjeang. "Macroscopic In-Situ Modeling of Chemical Membrane Degradation in Polymer Electrolyte Fuel Cells." In: *Journal of the Electrochemical Society* 161.9 (May 2014), F823–F832. DOI: 10.1149/2.0031409jes (cit. on pp. 161, 167, 172).

[195] K. H. Wong, E. Kjeang. "Mitigation of Chemical Membrane Degradation in Fuel Cells: Understanding the Effect of Cell Voltage and Iron Ion Redox Cycle." In: *Chem-*

SusChem 8.6 (2015), pp. 1072–1082. DOI: 10.1002/cssc.201402957 (cit. on pp. 162–164, 167–169, 172).

[196] J. Wu, X. Z. Yuan, H. Wang, M. Blanco, J. J. Martin, J. Zhang. "Diagnostic tools in PEM fuel cell research: Part I Electrochemical techniques." In: *International Journal of Hydrogen Energy* 33.6 (2008), pp. 1735–1746. DOI: 10.1016/j.ijhydene.2008.01.013 (cit. on p. 129).

[197] T. Xie, C. A. Hayden. "A kinetic model for the chemical degradation of perfluorinated sulfonic acid ionomers: Weak end groups versus side chain cleavage." In: *Polymer* 48.19 (Sept. 2007), pp. 5497–5506. DOI: 10.1016/j.polymer.2007.07.043 (cit. on pp. 153, 154).

[198] H. Xu, R. Kunz, J. M. Fenton. "Investigation of Platinum Oxidation in PEM Fuel Cells at Various Relative Humidities." In: *Electrochemical and Solid-State Letters* 10.1 (2007), B1–B5. DOI: 10.1149/1.2372230 (cit. on p. 60).

[199] L. Zhang, S. Mukerjee. "Investigation of Durability Issues of Selected Nonfluorinated Proton Exchange Membranes for Fuel Cell Application." In: *Journal of The Electrochemical Society* 153.6 (2006), A1062–A1072. DOI: 10.1149/1.2180715 (cit. on p. 152).

[200] S. Zhang, X. Z. Yuan, J. N. C. Hin, H. Wang, K. A. Friedrich, M. Schulze. "A review of platinum-based catalyst layer degradation in proton exchange membrane fuel cells." In: *Journal of Power Sources* 194.2 (2009), pp. 588–600. DOI: 10.1016/j.jpowsour.2009.06.073 (cit. on p. 30).

All links were last followed on January 11, 2019.

Acknowledgements

I would like to thank all the people who supported me in the course of my doctorate. Without your help this work would not exist.

First, I would like to thank Prof. Dr. Andreas Friedrich for the supervision of my work, the constructive criticism and the freedom he left me. I believe that your relentless scientific work will bring on the future of mobility and energy conversion.

Secondly, I thank Prof. Dr. Arnulf Latz for his willingness to co-review my work and his unconditional support during the time in his department. Your view on scientific modeling was a great inspiration.

I would like to thank Prof. Dr. Rainer Helmig for agreeing to act as additional examiner. Your lectures during my studies at the University of Stuttgart inspired me to tread the path that lead me to this point.

Special thanks go to Dr. Thomas Jahnke, a demanding and relentless supervisor, who always had an open ear for my problems and helped wherever he could. Thank you very much.

I thank all the colleagues at DLR Stuttgart and especially the members of the modeling groups in Stuttgart and Ulm for the great time at work, on conferences and other occasions. It was a pleasure to work with you.

Moreover, I would like to thank all the developers of Dumu^{X} which built the basis for my work. Thanks go to the developers at LH^{2}, especially Dr. Bernd Flemisch, for their help and support.

I thank the European Union for the funding of this work and all project partners from the PUMA MIND Project.

Finally, I would like to thank my parents, my brother and all of my friends who are always at my side and who I owe so much.

Above all, I thank my beautiful wife Anja and my son Nils for bearing me during this work. You are the light of my life. I love you.

Declaration of Authorship

I hereby certify that the dissertation entitled

PHYSICAL MODELING OF PEMFC PERFORMANCE AND CHEMICAL MEMBRANE DEGRADATION

is entirely my own work except where otherwise indicated. Passages and ideas from other sources have been clearly indicated.

Ich versichere, dass ich die vorliegende Arbeit mit dem Titel

PHYSIKALISCHE MODELLIERUNG VON PEMFC LEISTUNG UND CHEMISCHER MEMBRANDEGRADATION

selbständig verfasst und keine anderen als die angegebenen Quellen und Hilfsmittel benutzt habe; aus fremden Quellen entnommene Passagen und Gedanken sind als solche kenntlich gemacht.

Name/Name: _____

Unterschrift/Signature: _____

Datum/Date: _____